Plasma Transport and Development of Plasma Kinetics in ARIS

Felipe Soberón Vargas Prada

(full name)

May 2005

PLASMA TRANSPORT AND DEVELOPMENT OF PLASMA KINETICS IN ARIS

A thesis for the degree of

PHILOSOPHIAE DOCTOR

Presented to

DUBLIN CITY UNIVERSITY

By

FELIPE SOBERON
School of Physical Sciences
Dublin City University

Research Supervisors.
Dr. Bert Ellingboe and
Prof. Miles M Turner

External Examiners: Dr Pascal Chabert and
Dr Stephen Daniels

May 2005

Declaration

I hereby certify that this material which I now submit for assessment on the programme of study leading to the award of Philosophiae Doctor is entirely my own work and has not been taken from the work of others save and to the extent that such work has been cited and acknowledged within the text of this work

F. Soberon

Felipe Soberon

ID No 51168979

13th May 2005

Abstract

The topic of this thesis is the study of basic plasma transport and chemistry in the diffusion chamber of the ARIS (Applied Radio-frequency Ion Source). The ARIS experiment has been designed as a two chamber system, with a source (high density plasma region) and a diffusion region (plasma expansion region). The boundary conditions on the diffusion chamber and the neutral pressure determine the plasma parameters. Careful control over the boundaries give us some control on the plasma volume chemistry key element: the electron energy distribution function(EEDF). We explore the possibility of a magnetised boundary in the the diffusion chamber region by means of a multi-cusp magnetic array. A multi-cusp produces an effective field close to the boundary with low penetration on the plasma bulk. The diffusion chamber gains a sub-region defined by the magnetic field penetration region. Experimental measurements of the electron energy distribution function with a single Langmuir probe are compared with double probe results. Also the negative ion density (H^-) is measured in Hydrogen plasmas. Volume production of H^- requires special conditions of the EEDF and molecular Hydrogen vibrationally excited states to maximise the negative ion density. Results are compared for magnetised and non magnetised boundaries in the diffusion chamber. Results show that the magnetic field improve the plasma confinement (higher plasma density) and reduces the average kinetic electron energy (or Te) by actually changing the EEDF shape. It is proposed that this effects are the reason for the improvement on volume production of H^- in a magnetised case in the diffusion chamber while the state of the population of vibrationally excited Hydrogen molecules is not clear. Finally, particle

models complement the experimental work by providing some insight on single particle interaction with a multi-cusp magnetic field and self-consistent plasma interaction with a cylindrical Langmuir probe Also a global model developed by R Zorat is used to complement and understand the experimental results

Acknowledgements

I would like to thank first my supervisor, Dr Bert Ellmgboe, for giving me the opportunity to do a PhD I had the chance to know Dr David Vender and would like to thank him for encouraging me through the short time I met him I thank fruitful discussions on plasma modelling with Prof Miles Turner Dr Mike Hopkins for the tremendous boost he gave to our project, making the CRDS diagnostic possible, many encouraging discussions and personal trust Dr Ronan Faulkner for his assistance on developing the ARIS experiment Des Lavelle and Cian Merne at the Physics School Workshop for building and modifying many of the experimental parts for ARIS Pat Wogan for his help on the electronics All the PRL students for many discussions which help me to start understanding the physics of plasmas The Plasma Research Laboratory administrators, Samantha Fahy and Dierdre O'Riordan, and the secretaries, Sarah Hayes and Elizabeth Breen, and the School of Physics secretary, Lisa Peyton I thank also Mark Stapleton for his friendship and help

On a personal note, we (Erika and I) would like to thank David Vender, Dierdre O'Riordan, Elizabeth Breen and very specially Angus McCarter and Samantha Fahy for their help and support during an unfortunate event Our family is grateful for their kind support

We would also like to thank our many new friends in Ireland who made our life a more pleasant one Our "Irish mother", Judith Lennehan, and Seoirse, John and Raul, Milena and Jim, Cecilia and Jack, Carmen and Luke, Patricia and Des, Mayra and her family, Erika and Armando, Erika and Michael, Helen, Orla and Javier, and many other friends

Finally, I am very grateful to my wife, Erika Peña, for allowing us to come to Ireland and enduring the my studies I thank her and my children, Victor

and Rodrigo, for their unconditional support and for giving me a rather exciting life I reckon that Erika gave up her well established and happy life in Perú to come over and start a new one Erika's strength, energy, goodwill, courage, good humour and very hard work to support emotionally and financially this family are the ultimate reasons I can finally present this work

Contents

List of Figures

LIST OF FIGURES

List of Tables

LIST OF TABLES

CHAPTER 1

Introduction

In this chapter we give a description of the development of ion sources for Neutral Beam Injectors (NBI) for fusion devices We also explain the chemistry in H^- sources and explain the motivation for the work done

1.1 The Bucket Source

On the early seventies MacKenzie et al [1, 2] developed a multi-cusp source for containing a large volume of quiescent uniform plasma with densities higher than 10^{18} m^{-3} in Argon The source was a cylindrical vessel which was fitted with an arrangement of permanent magnets around the walls, it was called a Bucket source The plasma was produced and sustained by electron emission from tungsten filaments at low background pressures in Argon, Helium, Deuterium and Hydrogen This new design proved to be very

effective in producing a high density, low pressure, plasma. This attracted people working on the development of a volume ion source for neutral beam injectors (NBI). NBIs are used to introduce high energy neutral Hydrogen or Deuterium atoms into a fusion device to reach the fusion state. New sources with permanents magnets around the device were built to produce beams of positive ions of Hydrogen (H^+/D^+) which would be neutralised passing the beam though neutral gas to finally obtain a neutral beam of H/D [3].

The development of bigger fusion devices required high energy neutral beams but unfortunately the neutralisation efficiency decreased with the ion beam energy leading to large amounts of energy been waisted [4, 5]. On the other hand the neutralisation efficiency remained high if Hydrogen negative ion were used instead.

1.2 Hydrogen negative ion sources and chemistry

On the late seventies M Bacal et al(J. Phys. (Paris) 38, 1399) discovered unexpected large populations of negative ions (100 times greater than anticipated) in a low pressure Hydrogen filament discharge (H^-). They measured and confirmed their results with laser photodetachment onto a Langmuir probe [6]. This marked the start of research on volume negative ion sources for NBI.

After Bacal et al results the accepted chemistry of a Hydrogen discharge was not able to explain the large densities of negative ions measured until the large cross sections of dissociative attachment reactions of vibrationally excited Hydrogen molecules were accounted.

Here we present the main reactions leading to the creation and destruction

of H^- [7] It is important to note that the threshold energies and cross sections for the various reactions that follow picture a quite complicated series of requirements for the optimisation of the negative ion density, needless to say for the extraction

- The H^- losses
  - Collisional electron detachment Cross section 10^{-20} m^2

$$e(\geq 0\ 75eV) + H^- \rightarrow H + 2e \tag{1 1}$$

  - Wall collisions, this is a small rate due to confinement by positive plasma potential

$$H^- + \text{wall} \rightarrow H + e \tag{1 2}$$

  - Collisions with positive ions Cross sections for n=1,2 of the order of 10^{-18} m^2 This reactions encompass recombination $(H^- + H_2^+)$ and electron transfer $(H^- + H^+)$

$$H^- + H_n^+(n = 1, 2, 3) \rightarrow H + [H] \tag{1 3}$$

- The H^- production channels
  - Dissociative attachment to metastable molecules, cross section 10^{-22} m^2 and up to 10^{-21} m^2 with rovibrational excitation

$$e + H_2(^3\Pi u) \rightarrow H(2p) + H^- \tag{1 4}$$

  - Dissociative recombination of molecular ion, maximum cross section $1\ 6 \times 10^{-22}$ m^2

$$e + H_3^+ \rightarrow H_2^+ + H^- \tag{1 5}$$

$$e + H_2^+ \rightarrow H^+ + H^- \tag{1 6}$$

- A two step excitation and a dissociative attachment processes The first reaction requires high energy (≥20 eV) electron impact to create rovibrationally excited H_2 followed by radiative decay to a vibrationally excited level of the ground state

$$e(\geq 20eV) + H_2(v = 0) \rightarrow H_2^* + e \rightarrow H_2(v^*) + h\nu + e \qquad (1\ 7)$$

The second step involves low energy (0 14-3 75 eV) dissociative attachment producing the desired negative ion

$$e(\sim 0\ 14 - 3\ 15eV) + H_2(v^*) \rightarrow H^- + H \qquad (1\ 8)$$

This process is supposed to have the largest cross section and is assumed to be the main H^- volume production channel Table 1 1 show the dissociative attachment cross sections and threshold energies for different vibrational levels of H_2 [7–9] Notice the cross sections increase by several orders of magnitude with increasing vibrational energy level while the threshold energy drops significantly, this process is accessible to electron distributions with temperatures as low as 1 eV Mosbach et al [10] have measured the vibrational populations of H_2 m a magnetic multipole or "bucket" source and using the cross sections calculated the electron energy dependence to the dissociative attachment rate Their results show that vibrational states around $v = 8$ (created by electron impact, electrons with energies as low as 0 5 eV) are the most important for negative ion production Therefore the production and loss of vibrationally excited Hydrogen molecules is important for this negative ion production mechanism

- Other less important reactions like radiative capture (cross section

5×10^{-26} m^2),

$$e + H \rightarrow H^- + h\nu \tag{1 9}$$

three body capture

$$e + H + t \rightarrow H^- + t \tag{1 10}$$

and other reactions with reasonable cross sections only for incident particles with energies of the order of 10 keV, unlikely for a low temperature plasma

$$H + H \rightarrow H^- + \tag{1 11}$$

$$H + H_2 \rightarrow H^- + \tag{1 12}$$

$$H^+ + H_2 \rightarrow H^- + \tag{1 13}$$

$$H_2^+ + H_2 \rightarrow H^- + \tag{1 14}$$

For a full set chemical reactions in a Hydrogen plasma refer to Zorat et al [11, 12] and Zorat PhD thesis [13] A global model for and inductive Hydrogen discharge was developed and large list of chemical reactions were accounted including wall reactions and production and loss of vibrationally excited H_2 This model is used in our thesis to compare with experimental measurements in a Hydrogen plasma discharge

Since the eighties most of the research was developed in modified multicusp sources for negative ion extraction [14–18] The chemistry involved in the negative ion volume production of H^-/D^- required careful design of the source In particular to enhance the negative ion production through the vibrationally excited states of H_2 and to minimise the destruction through the electron detachment process

Volume sources were designed with three well defined regions First, the source region, where high energy is coupled to the gas to produce a high

v	E(eV)	$\sigma(DA)$ (cm^2)
0	3 75	$2\,8 \times 10^{-21}$
1	3 23	$8\,3 \times 10^{-20}$
2	2 75	$1\,0 \times 10^{-18}$
3	2 29	$7\,5 \times 10^{-18}$
4	1 86	$3\,8 \times 10^{-17}$
5	1 46	$1\,2 \times 10^{-16}$
6	1 08	$2\,9 \times 10^{-16}$
7	0 74	$4\,3 \times 10^{-16}$
8	0 42	$3\,2 \times 10^{-16}$
9	0 14	$4\,3 \times 10^{-16}$

Table 1 1 *Dissociative attachment cross section and threshold energy for different vibrational levels of H_2 [7–9]*

density plasma Second, the filter region, which consists of a magnetic field perpendicular to the plasma diffusion to filter high energy electrons And finally, the extraction region, a low electron temperature plasma bounded by extraction grids and focusing magnetic fields to extract a negative ion beam This modified "bucket" volume sources are called "tandem" sources Their structure is explained as follows The high density plasma is rich in high energy electrons which are necessary to produce vibrational states of hydrogen The magnetic filter is used to create a low temperature plasma region after the source, the extraction region, where the destruction rate (of negative ions) drops significantly while the dissociative attachment rate (negative ion production) is still significant Being neutral it is expected that the vibrationally excited Hydrogen molecules produced in the source would be transported across the magnetic field into the extraction region, where

the low electron temperature would favour the negative ion production

Theoretical work on the electron flow and cooling through the transverse magnetic field has been done by Holmes [19, 20] with good agreement on the experimental results Recently Fukano et al [21] have reviewed the calculation taking into account the conservation of electron particles and heat flux They calculate the production and destruction rates of H^- as a function of position through the transverse field Assuming a Maxwellian electron energy distribution function they show that the dissociative attachment reaction rate stays constant or drops depending on the magnetic field intensity and that the destruction electron detachment significantly drops

The negative ion concentration in Hydrogen mixtures with noble gases was studied by Curran et al [22] in the RF excited "bucket" source, DENISE (Deuterium Negative Ion Source Experiment) Their results showed that Argon was the best mixture to enhance the negative ion production Noble gases, in particular Argon and Xenon, affect the plasma by reducing the electron temperature, thus decreasing the H^- losses, and increasing the electron density The overall effect is to increasing the dissociative attachment rate But results on Argon, which showed better yield compared to Xenon, could not be explained just by these means so they proposed a resonant energy transfer from Argon metastable atoms to Hydrogen molecules to increase the production of vibrational molecules of H_2 and therefor enhance the volume production of H^- This is, Argon metastable energy transfered though a photon to Hydrogen singlet states which decay to ground-state vibrationally exited states, this reaction would result in an increase on the intensity of Lyman bands in the vacuum ultraviolet (VUV) from the discharge Bacal et al [23] measured the H^- densities and VUV radiation in a bucket source They confirmed that the negative ion density increases with the addition of

Argon but found no increment in the VUV radiation, they concluded that Argon does not enhance the production of vibrationally exited states of Hydrogen Mosbach et al [10] used laser induced fluorescence to measured the vibrational populations of H_2 in a "bucket" source in pure Hydrogen and Argon and Xenon mixtures up to 40% He also reported no effect on the vibrational populations of hydrogen by noble gas admixtures

1.3 Motivation

Most of the development of negative ion sources through the eighties and early nineties was based on filament based multi-cusp ("bucket") sources This sources have a few technical problems High emission of electron from hot filaments results also in contamination of the plasma and source walls with the material of the filament (typically tungsten or molybdenum) The coating of the filament material on the source walls changes its work function resulting in unexpected changes in the negative ion production due to enhanced wall production, this is actually pursued by allowing a seed material like caesium in the discharge The replacement of the filaments represent another technical problem More recently RF excited negative ion sources are being tested [22, 24] While in some cases basically the same design approach is used on RF excited sources as on filament driven discharges there are some differences The EEDF is bi-Maxwellian in low pressure filament discharges while it is approximately Maxwellian in RF inductive sources Therefore the multi-cusp tandem design does not seem to be that effective in RF excited sources [23]

While most of negative ion source prototypes are required to deliver large quantities of negative ions and are driven to extreme conditions it is still

necessary to work on a prototype of a RF negative ion source where basic plasma studies can be performed This motivated in Dublin City University (DCU) the development of the Applied Radio-frequency Ion Source (ARIS), this device is presented in the next chapter

The purpose of this PhD work is to setup this experiment and start to develop basic tools for electron energy distribution function measurements, negative ion densities, and other plasma parameters Throughout this document the basics of the diagnostics used are presented, experimental data is analysed and compared with single particle, full kinetic and global models Through the comprehensive understanding of the models and results we setup the basis for future research on this device

CHAPTER 2

Experiment The ARIS device

2.1 Introduction

The Applied Radio-frequency Ion Source (ARIS) is designed for the study of low temperature plasma chemistry –such as volume production of hydrogen negative ions (H^-)– and plasma transport, including transport into a magnetised region

The ARIS system consists of an inductively coupled radio-frequency source, a diffusion chamber, and an extraction plate, permanent magnets can be mounted on the end-plate and/or on the diffusion chamber It is designed so that various diagnostics can be implemented, mainly in the diffusion chamber, through its many access ports An axial DC magnetic field can be added to the source

2.2 Source and diffusion chambers

The ARIS experiment consists of two attached chambers The source which is mainly made of dielectric material where the plasma is excited with an external antenna and the diffusion chamber where plasma expands

The source region consists of an alumina cylinder closed on one end with a stainless steel cap, and open to the diffusion chamber on the other end Two different source types have been used, these differ on the dielectric cylinder length and attachment mode to the diffusion chamber The first type of dielectric cylinder protrudes into the diffusion region (*re-entrant* type) through a stainless-steel flange The second type of dielectric cylinder ends on the stainless-steel flange (*mating* type) The stainless-steel flange is part of the diffusion chamber and allows to connect the source with the diffusion region The source dielectric cylinder is 80-85 mm internal diameter, 100 mm external diameter and, 150 mm (*mating* type) or 170 mm (*re-entrant* type) long The source volume is 0 85 litre A two-turn antenna is wrapped around the dielectric cylinder The antenna voltage/current is driven with a radio-frequency generator (13 56 MHz) The power is coupled through the dielectric to the plasma

The diffusion chamber is a stainless-steel cylinder It is 410 mm internal diameter and 290 mm long The diffusion chamber volume is 38 3 litre It is closed on both ends with stainless-steel or aluminium flanges The source is connected to the diffusion chamber trough an aperture on one of the flanges (stainless-steel) The other end is closed with a solid stainless-steel or aluminium flange This flange and the diffusion chamber are fitted with diagnostic ports (KF40) providing access to the internal volume of the system The diffusion chamber has also two view-ports and one vacuum pump port (NW160 ISO-K) The aluminium end flange has been specially

designed to house four rows of permanent magnets, separated 80 mm between pairs

All metal surfaces in the ARIS device are grounded The total volume of the ARIS experiment –not considering extra volume due to extensions from attached diagnostics– is 39 1 litre Figure 2 1 shows a three-dimensional schematic diagram of the ARIS experiment source with antenna and matchbox and diffusion chamber Diagnostic, view and pump ports have not been included in this diagram

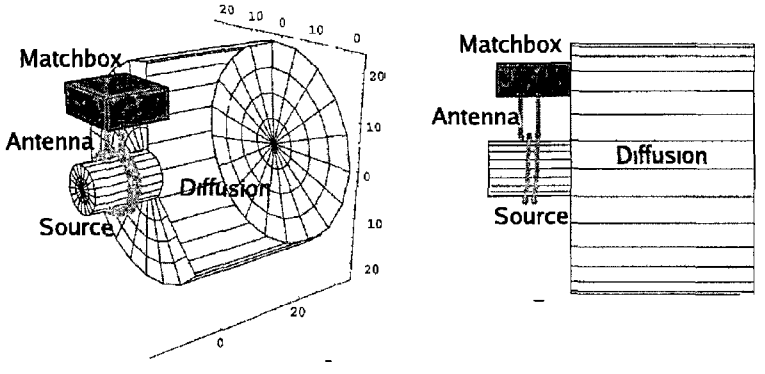

Figure 2 1 *Three-dimensional and side view of a 3D schematic diagram of the ARIS experiment*

2.3 Gas supply and vacuum system

The gases used are Argon and Hydrogen Gases are fed into the diffusion chamber through a set of mass flow controllers (Ar 100 SCCM and H_2 200 SCCM) and pumped using a turbo-molecular pump, pumping speed 520 litre/second

Inlet gas points are located at the bottom of the diffusion chamber and during Cavity Ring Down Spectroscopy (CRDS) measurements also at the far end of a pair of extension arms (section 2 6) The extension arms are

used to mount a pair of high reflectivity mirrors required for CRDS and the gas is fed in front of the mirrors to prevent plasma affects on them CRDS is described in section 3 3

Neutral pressure is measured with a hot filament pressure gauge Base pressure $< 1 \times 10^{-6}$ mbar and operation pressures are in the range 0 5-10 mTorr ($6\ 7 \times 10^{-4} - 1\ 3 \times 10^{-2}$ mbar) When the experiment is operated the pressure is set controlling the gas flow Once pressure is achieved the flow is kept constant during the rest of measurements

2.4 RF power supply and coupling

To excite and maintain the discharge a two turn antenna –a copper tube wound around the source tube– is driven at 13 56 MHz using an ENI OEM-28B 2 8kW power supply A matchbox is required to match the antenna impedance to the power supply output impedance (50 Ω) for maximum output power coupling

The dielectric cylinder and the antenna wrapped around are shielded with an external aluminium cylinder (130 mm internal diameter and 10 mm thick) to prevent radio-frequency radiation leaking out The matchbox connection to the antenna is also shielded with a rectangular aluminium section

The source is air and water cooled A fraction of the power is deposited in the antenna itself and is dissipated as ohmic heating Also ion bombardment on the source walls contribute to excessive heating of the dielectric cylinder and its end cap Air is flowed around the dielectric cylinder to prevent overheating and material stress and water cooling is used on the end cap

The ENI radio-frequency power supply forward power can be externally set by means of a serial connection (command mode) into a PC using Lab-

View subroutines or through an external –analog– voltage The command mode operation allows for extra features such as readings of the forward and reflected power

The matchbox is a modified AMAT (Applied Materials) PI-type It is powered by two voltage supplies through a 25 pin connector The tune inductor and load capacitor positions can be recorded measuring a couple of voltage signals from the Match-Box For further details on the matchbox and pin connection settings see section A 2

LabView routines developed to control the experiment and diagnostics can implement in-loop control to determine safe operation from the forward/reflected and matching readings

The discharge is initially triggered by means of capacitive coupling through the dielectric due to the high –radio-frequency– voltage on the antenna Once the plasma density is large enough the coupling turns mainly inductive although a fraction of the power is still capacitively coupled

2.5 Multi-cusp set-up

The end flange (opposite to the source) on the diffusion chamber can be fitted with permanent magnets to make a multi-cusp arrangement as shown in figure 5 1 (section 5 1 1) An extraction region is defined by means of the short range magnetic field produced by the multi-cusp An extra set of permanent magnets can be arranged around the diffusion chamber cylinder to further improve plasma confinement The permanent magnets used are bars of Samarium Cobalt (Sm Co, 5 kG)

2.6 CRDS set-up

Cavity Ring Down Spectroscopy is an optical diagnostic used on the diffusion region of the ARIS experiment to measure negative ion density, it is described in section 3 3 For this purpose two extension arms are attached to opposite horizontal ports on the diffusion chamber, arms are 300 mm long Highly reflective mirrors are mounted at each end of the extension arms on special mirror mounts, this mirrors define the CRDS cavity The mirror mounts have three adjusting screws for fine tuning the optics alignment The extension arms also have gas inlet points close to the mirror mounts to allow neutral gas flux in order to prevent mirror reflectivity drift due to the plasma 5 mm apertures are placed at the joints where the extension arms and the diffusion chamber meet to further prevent plasma affects on the mirrors, the highly sensitive side of the mirrors is exposed to vacuum/plasma

A Nd YAG laser is tuned on the second harmonic (532nm) and mounted on an optical table next to the diffusion chamber The laser beam is directed with a set of mirrors These are also used to align the beam in the cavity such that the beam joins the centres of the two highly reflective mirrors Apertures (1 5 mm diameter) are placed outside the cavity in-between mirrors to reduce the beam diameter A photo-multiplier (PMT) is mounted on one of the mirrors mount –opposite to the beam pumping end– to measure the output light intensity A pass-filter and a neutral density filter are placed between the PMT and the high reflectivity mirror to reduce the plasma light intensity and to filter other light sources except the laser source

The Nd YAG laser is synchronised with the radio frequency generator, Two signal generators are used for this purpose The first pulses the power supply at 5 Hz with a 50 % duty cycle while the second pulses the laser at 10 Hz The phase difference between the waveform generator is such that the

laser triggers 200 μs before the radio frequency generator turns the power level up or down This way successive CRDS signals for *on* (plasma) and *off* (no plasma) states can be recorded The PMT signal is amplified with a home made amplifier and recorded by a fast digitiser (National Instruments) at 5 MS/s (mega sample per second) and 14 bit resolution A LabView routine controls the data acquisition and performs fast treatment of the raw data followed by basic analysis in real time Figure 2 2 shows a schematic of the CRDS measurements set-up

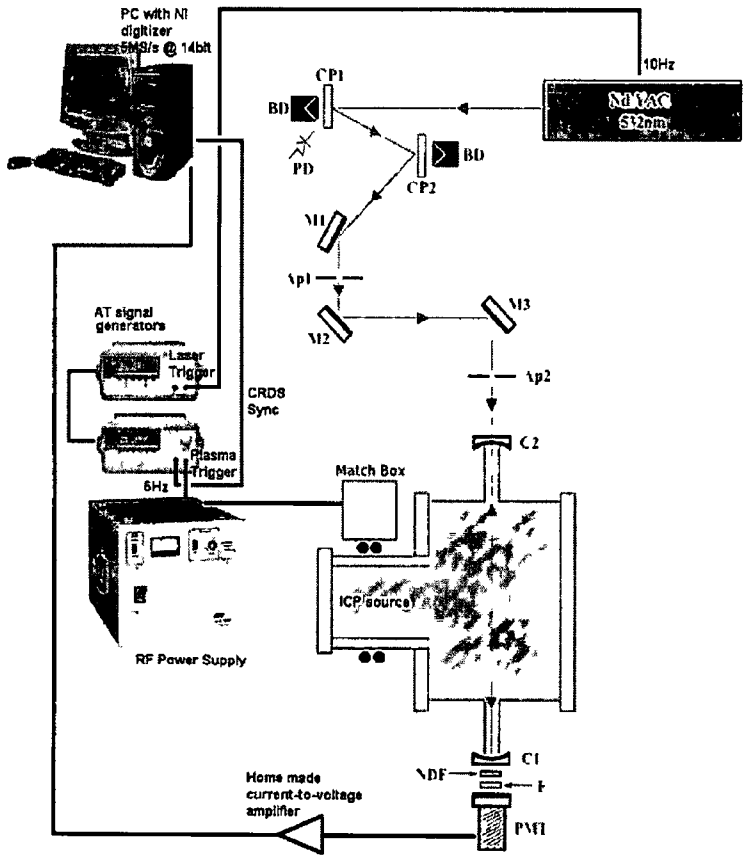

Figure 2 2 *CRDS measurement set-up*

2.7 EEDF measurements set-up

The electron energy distribution function (EEDF) is measured using a single Langmuir probe The technique and analysis are described in section 3 1 4 Figure 2 3 shows the hardware set-up for these measurements A small sinusoidal signal and DC voltage are generated with a waveform generator The full signal is amplified and used to drive a single Langmuir probe The *sync* signal from the waveform generator is used as an input oscillation to set the base frequency in a lock in amplifier, the lock in amplifier is set to detect second harmonic amplitude and phase respect to the set waveform signal The total current driven by the probe is measured with a 100 Ω resistor and amplified with an isolation amplifier The current signal is input into the lock-in-amplifier The probe voltage and current and floating potential measured by a second probe are recorded with a data acquisition (DAQ) card The waveform generator and the lock in amplifier are controlled with a PC through a GPIB connection A LabView routine controls the DC voltage setting on the waveform generator and the data recording from the lock in amplifier and data acquisition card

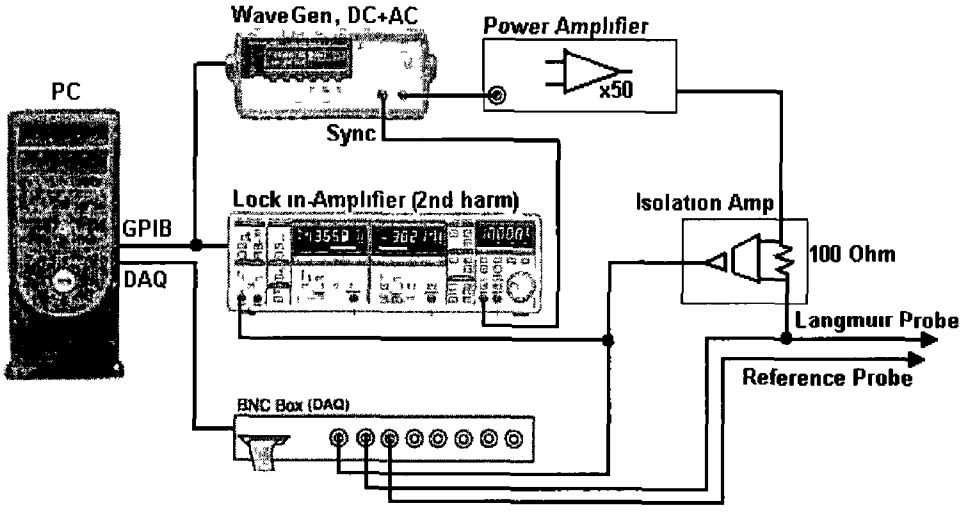

Figure 2 3 *EEDF measurement set-up*

CHAPTER 3

Diagnostics

Here we introduce the diagnostic techniques used on the experimental campaigns in ARIS

We developed a set of different electrostatic probes single and double Langmuir probes For the single probe we use the SmartProbe (Scientific Systems) system and analysis technique For electron energy distribution function measurements we develop our own single probe and use the AC superimposing technique with the Druyvesteyn method to analyse the data For the double probe we built a floating driver and current signal measurement electronic box, combined with a signal generator and a data acquisition card we record the I-V trace for analysis Section 3 1 presents the techniques and basic theory and give details of probe construction

We also set up and optical diagnostic in ARIS Cavity Ring Down Spectroscopy (CRDS) We use CRDS to measure negative ion density (H- den-

sity, 532nm) The theory and analysis technique developed for CRDS are presented in section 3 3

3.1 Electrostatic Probes

3.1.1 Introduction

In 1924 Langmuir and Mott-Smith developed the electrostatic probe, also known as the Langmuir probe They also developed the first probe theory Orbital Motion Limited (OML) [25] Since then the probe has been widely used, further developed (double/triple probes) and many theoretical, computational and experimental reports have been written to link the experimental characteristics of the probes and the actual plasma parameters [26–28] In this section we present the single and double Langmuir probes and some of the basic theories and techniques

A single Langmuir probe is a conducting material (a small electrode) inside the plasma region to study, it might have different shapes like a flat disk (planar geometry), a wire (cylindrical) or a sphere (spherical) The probe is usually biased (V_{bias}) with DC voltage or ramps with frequencies up to kHz, the bias respect to the vacuum chamber (if large grounded conducting area, otherwise double probe is preferred) Total current to the probe is measured electron and ion currents altogether, and a current-voltage characteristic (I-V trace, measured current v bias voltage) is plot Plasma parameters are calculated from the I-V trace electron temperature (T_e), plasma potential (V_P), floating potential (V_f), electron and ion density (n_e and n_i) and the Debye length (λ_D) Single probes scanning the full characteristic are even capable of measuring the electron energy distribution function (EEDF)

The double probe consists of two conductors (small electrodes), one bias respect the other Both electrodes are isolated from ground, floating This probe can follow low frequency oscillations but not radio-frequency oscillations of the plasma potential Again the current through the probe is

recorded and plotted against the bias voltage to plot a double probe I-V trace. Double probes are restricted to scan the plasma from the floating potential into the ion saturation region but are more sensitive to the tail of the electron energy distribution and do not perturb the plasma as much as a single probe does while it is biased around and beyond the plasma potential.

Figure 3.1 shows a basic diagram of a single and a double Langmuir probe immerse in a plasma.

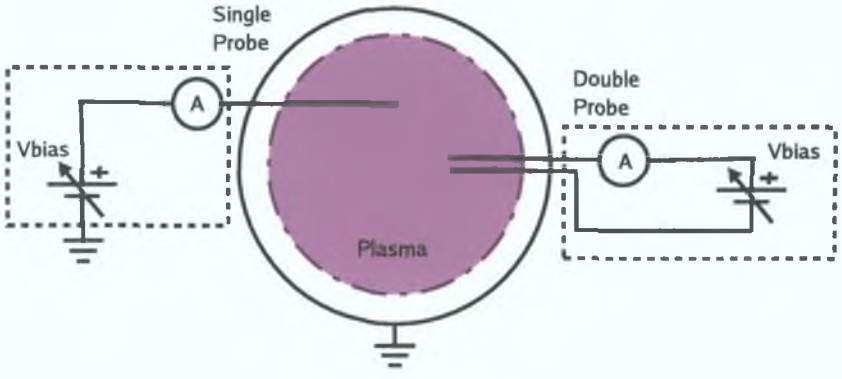

Figure 3.1: *Basic diagram of a single and a double probe immersed in a plasma.*

In 1930 Druyvesteyn showed that the electron energy distribution function can be calculated from the second derivative of a single Langmuir probe I-V trace (d^2I/dV^2) [29]. There are different techniques to measure the second derivative of the I-V trace of a Langmuir probe: numerical derivatives of experimental I-V traces [30, 31]; numerical calculation from the first derivative of the I-V trace by a differentiator circuit, or directly by a second derivative differentiator circuit [32] and, the AC signal superimposing method [33, 34].

The first technique requires a standard Langmuir probe voltage sweep driver with current measurement. The second and third include an extra differentiator circuit to generate the first and second derivative of the I-V trace

and store the data The last one adds an AC signal –on the order of kHz– to the DC voltage sweeper of the Langmuir probe For different DC voltages the current component of the second harmonic of the AC signal is proportional to the second derivative of the I-V trace For the first three techniques numerical instability on the EEDF (distortion) can develop from sweep steps too small or from a high noise to signal ratio To overcome this problem one can average the signal over many samples and/or use a combination of analog/digital filters But even though the I-V trace can be smoothed the second derivative might not be In some cases the smoothing might shadow the EEDF structure The AC superimposing technique requires a lock in amplifier to measure the second harmonic of the AC signal In any of these techniques the second derivative contribution of the ion current can be ignored or included in the calculation for correction, but unfortunately the actual shape of the ion current is not known in general, not even under some special conditions (OML)

We have constructed single and double Langmuir probes for our experimental work on ARIS We also have used a commercial Langmuir probe (Smart-Probe, Scientific Systems) and compared results with our home made ones Our single probes can be driven with the Smart-Probe voltage driver and analysed with its corresponding software (Smart-Soft) We have also built our own single probe driver, data can be collected and analysed by means of a data acquisition card and a Labview routines Standard techniques are used to calculate plasma parameters from the I-V traces and we also used the AC superimposing technique to measure the EEDF in ARIS

In this chapter we explain the basic structure of the I-V trace on Langmuir probes (single/double), we review the theory of Druyvesteyn and the AC superimposing technique for the EEDF measurements and present some

general formula to analyse the EEDF, and we explain the details of our home made probes (RF considerations) and the electronics setup.

3.1.2 Probe characteristics

Single probe I-V trace

In this section we explain the typical single probe I-V trace through key points. Consider that in low temperature plasmas –like the ones in ARIS– the average electron energy is much higher than the average ion energy and considering also the mass difference we should expect the thermal electron flux to be larger than the thermal ion flux. This fact should be appreciable as a high asymmetry in the I-V trace.

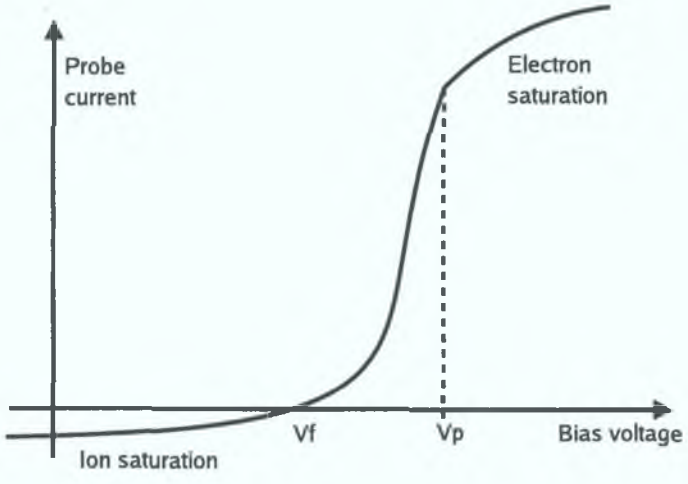

Figure 3.2: *Typical current-voltage characteristic for a single probe*

Figure 3.2 shows a typical I-V trace for a single probe. The electron current into the probe is taken as positive while the ion current is taken negative; this shall be the convention for probe characteristics throughout this thesis. The plasma and floating potential and electron and ion saturation currents are explained as follows.

- Plasma potential (V_P). If the bias voltage equals the plasma potential (or space potential) then the electron and ion currents are given by each species thermal flux since the probe does not build up any voltage difference with the plasma. At this point the electron current is by far larger than the ion current due to mass and temperature differences ($T_e \gg T_i$, $m_e \ll M_i$).

- $V_{\text{bias}} < V_P$. If the bias voltage is lower than the plasma potential the probe generates an electric field which becomes a potential barrier for electrons with energy $E < V_P - V_{\text{bias}}$. Therefore electron current is reduced while ions are attracted to the probe.

- Floating potential (V_f). The bias potential is called the floating potential if no net current flows through the probe; species currents cancel ($I_e = -I_i$).

- $V_{\text{bias}} < V_f$. If the bias voltage is lower than the floating potential the potential difference ($V_P - V_{\text{bias}}$) is large enough to repel most of the electrons. Most of the probe current is due to ions, so called ion saturation current.

- $V_{\text{bias}} > V_P$. On the other side if the bias is larger than the plasma potential no ions are collected by the probe and all current is due to electrons, so called electron saturation current.

- Electron and ion saturation currents

  - In either case (electrons or ions) the probe current continue to increase (positive/negative).

  - In this regimes there is a typical sheath expansion (collective plasma behaviour to shield the increasing electric field from the

probe) which leads to an increase of the effective collection area, this explains the fact that there is not a strict saturation

- The saturation currents shape in the I-V trace are dependent on the probe geometry/shape (planar, cylindrical, spherical)
- Saturation currents perturb surrounding plasma because of the sheath expansion and increased particle collection which may deplete the population of the collected species An auxiliary DC probe measuring the floating potential could be used to correct the I-V trace (non-corrected I-V traces exhibit higher plasma potentials V_P)

Double probe I-V trace

A double probe characteristic trace depends on the size of the probe tips If both tips are of similar dimensions then the I-V trace is symmetric On a double probe one probe tip is biased with respect to the other such that the return current from one tip to the other depends on the particles each can collect, this differs from the single probe where the return current is provided by the device walls

Figure 3 3 shows a typical I-V trace for a symmetric double probe, this is the probe tips are equal size (same collection area) It is also assumed that the probe tips are close enough to be exposed to similar regions of plasma (with similar plasma parameters), but not too close to interfere with each other The probe shape is explained as follows

- $V_{Bias} = 0$ If the potential difference between probe tips is null there are no current driven through the probe tips, both collect the same electron and ion currents from the plasma (symmetric probe) The

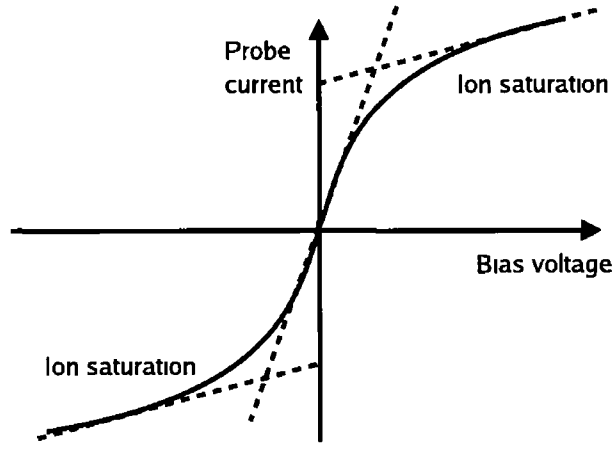

Figure 3 3 *Typical current-voltage characteristic for a symmetric double probe*

probe tips are floating and if we could measure the voltage of the tips respect to ground it would correspond to what a single probe would measure for a floating potential (V_f)

- $|V_{Bias}| > 0$ If one tip is biased positive or negative respect the other and if both tips are equal (symmetric probe) then it does not make a difference which way we bias (the same current magnitude is expected with opposite sign) The tip that is biased negative will collect ions whereas the other will collect electrons Since the electron flux is larger ($T_e \gg T_i$) the positive tip does not need much potential difference respect to the floating potential to collect enough electrons to balance the negative tip ion collection, which requires almost all the bias difference between the probe tips Usually the ion saturation current is small compared to the electron current so we can think that one probe tip is driven into the ion saturation region while the other one remains around the floating potential

- $|V_{Bias}| \gg 0$ As the potential difference is larger between probe tips

the negative one will saturate on ion current The saturation current continues to increase with lower steepness though due to ion sheath expansion similarly to the single probe case

Notice that since the probe tips are floating when biased the potential difference of each respect to the floating potential will be completely determined by the balance of the charge collection of each probe tip

3.1 3 Probe data analysis

Single probe analysis

In the case of a planar probe (on the X-Y plane), the general expression for the electron current to a biased electrode (V_{bias}) in the plasma is

$$I_e(V_{\text{bias}}) = eA \int_{-\infty}^{\infty} \int_{-\infty}^{\infty} \int_{v_{\min}(V_{\text{bias}})=\sqrt{2(V_P - V_{\text{bias}})e/m_e}}^{\infty} \mathbf{v} \;\; \mathbf{n} f_e(\mathbf{v}) d^3\mathbf{v} \qquad (3\ 1)$$

where A is the probe surface area, $\mathbf{n}$ is a unitary vector normal to the probe surface and $f(\mathbf{v})$ is the electron velocity distribution function The minimum velocity an electron can have in order to reach the probe (and be collected) is determined by the difference between the probe bias and the plasma potential This is, the kinetic energy of the particle has to be greater or equal to the potential energy required to reach the probe ($1/2 m_e v^2 \geq e(V_{\text{bias}} - V_P)$) Conventional analysis assumes that the electron velocity distribution function is Maxwell-Boltzmann [26, 27, 35, 36]

$$f_e(\mathbf{v}) = n_e \left(\frac{m_e}{2\pi e T_e} \right)^{3/2} \exp\left\{ -\frac{1}{2} \frac{mv^2}{eT_e} \right\} \qquad (3\ 2)$$

The electron current drawn by the probe in the electron retardation region results from the integration of (3 1) with distribution (3 2)

$$I_e(V_{\text{bias}}) = \frac{1}{4} e n_e \langle v_e \rangle A \exp\left\{ \frac{V_{\text{bias}} - V_P}{T_e} \right\} \qquad (3\ 3)$$

Here $\langle v_e \rangle = \sqrt{8eT_e/\pi m_e}$ is the average mean velocity for a Maxwellian distribution *The retardation region of a current-voltage characteristic is mainly the I-V trace section below the plasma potential (V_P) In this section the electron collection by the probe is limited to those electrons with enough energy to reach the probe in spite of the repelling potential difference between the probe surface and the plasma*

When the probe is biased to a voltage greater than the plasma potential ($V_{\text{bias}} - V_P$) the electron current is assumed to be constant This current is said to be in saturation For the case of an ideal planar probe the electron saturation current is constant

$$I_e = \frac{1}{4} e n_e \langle v_e \rangle A \tag{3 4}$$

Also for the ideal planar probe the ion current to the probe is assumed constant

$$I_i = -e n_i u_{\text{Bohm}} A \tag{3 5}$$

Here the Bohm velocity is given by $u_{\text{Bohm}} = \sqrt{eT_e/M_i}$ for $T_i \ll T_e$

Equations (3 3), (3 4) and (3 5) represent the simplest approach to probe theory (standard theory) This equations neglect limited probe size effects or collisional effects It is important to note that the electron current formula (3 3) holds correct in the retardation region for collisionless plasmas for any probe geometry (EEDF is required to be isotropic) Formula (3 3) is used in section 5 2 2 to analyse modelled electron current

In the case of a cylindrical probe, orbital effects for attracted species must be considered, in particular for ions This is, ions entering the sheath with some angular momentum may miss the probe although been attracted to it Orbital Motion Limited theory (OML) [25] deals with this for spherical an

cylindrical probes. The OML formula for Maxwellian (attracted) ions is

$$I_i = -\frac{en_iA}{\pi}\sqrt{\frac{eT_i}{M_i}}\exp\left\{\frac{V_{Bias}}{T_i}\right\}\left\{\sqrt{\frac{\pi}{2}}\left(1-\mathrm{erf}\sqrt{\frac{V_{Bias}}{T_i}}\right)+\sqrt{\frac{2V_{Bias}}{T_i}}\exp\left\{\frac{V_{Bias}}{T_i}\right\}\right\} \tag{3.6}$$

where M_i and T_i are the ion mass and temperature respectively. For $V_{\text{bias}} \gg T_i$ the error function equals to 1 and equation (3.6) is reduced.

$$I_i = -\frac{en_iA}{\pi}\sqrt{\frac{2eV_{Bias}}{M_i}} \tag{3.7}$$

More elaborated theoretical work by Laframboise [37] consider potential barriers on the ions orbits due to angular momentum when the ratio r_p/λ_{De} is greater than one; where r_p is the probe radius and λ_{De} is the electron Debye length. The potential barriers considered by Laframboise reduce the ion current collected by the probe. Laframboise calculated the electron and ion currents to a cylindrical and spherical probe for different plasma and probe conditions by exploring the following non dimensional ratios: r_p/λ_{De}, T_i/T_e and ϕ/T_e. Part of the Langmuir data analysis done during the work presented in this thesis was performed with SmartSoft (Scientific Systems) which uses the Laframboise traces with optional thermal or Bohm current factor to fit the experimental data. The electron temperature and other plasma parameters are calculated from the best fit of the theoretical traces [38].

It is important to note that the basic theory presented here applies to collision-less plasmas, although no plasma is really collision-less. The effect of particle-neutral collisions on the ion saturation current has been studied by Sternovky et al [39, 40] and is discussed in section 5.2.2. The results presented in references [39, 40] correspond to an extreme case of low pressure and very low plasma density where the probe sheath size is comparable to the ion mean free path (for example the ion mean free path for an Argon ion at 1 mTorr is about 3 cm). But when the density is large (typically $> 10^{16}$ m^{-3}) so that

the Debye length is on the order or tenths of a millimetre and the sheath is considerably smaller than the ion mean free path and the collision-less theory applies.

Double probe analysis

As explained in section 3.1.2, for a symmetric double probe, each probe tip is biased from about the floating potential (V_f) into the ion saturation region. This is because the ion current limits the probe current. There is no electron saturation region in the double probe I-V trace. From the balance of the electron current for both tips at different voltages, using equation (3.3), and constant ion saturation current, the basic ideal expression for the total current through the double probe is [26, 35]

$$I(V_{\text{bias}}) = I_i \tanh\left(\frac{V_{\text{bias}}}{2T_e}\right) \tag{3.8}$$

Experimental data does not fit well to this formula because of the ion sheath expansion increasing the ion saturation current with the probe bias. If we assume that the ion current increases linearly with the bias voltage and if we introduce an offset current and voltage in the formula to account for small asymmetries on the probe construction [41] the double probe current formula becomes

$$I(V_{\text{bias}}) = I_i \tanh\left(\frac{V_{\text{bias}} - V_{\text{off}}}{2T_e}\right) + MV_{\text{bias}} + I_{\text{off}} \tag{3.9}$$

In spite of the simple assumption on the ion saturation, formula (3.9) fits well to experimental data. From the fit parameters we obtain the electron temperature, which is related to the tail of the electron energy distribution function (not to the low energy range or electron bulk). Also the ion saturation current is estimated form the double probe data. Note that on deriving formula (3.9) the EEDF has been assumed to be Maxwellian. Full EEDF and

double probe measurements in ARIS (presented in section 5 1 1) show that estimated electron temperatures from the double probe data are sensitive to the actual shapes of the EEDF

Figure 3 4 shows a sample double probe characteristic recorded in the diffusion chamber in ARIS Data (points) are fitted using equation (3 9), the mean square root error of the fitting is on the order $\sim 10^{-2}$ Estimated electron temperature 2 9 eV and ion saturation current 26 0 μA

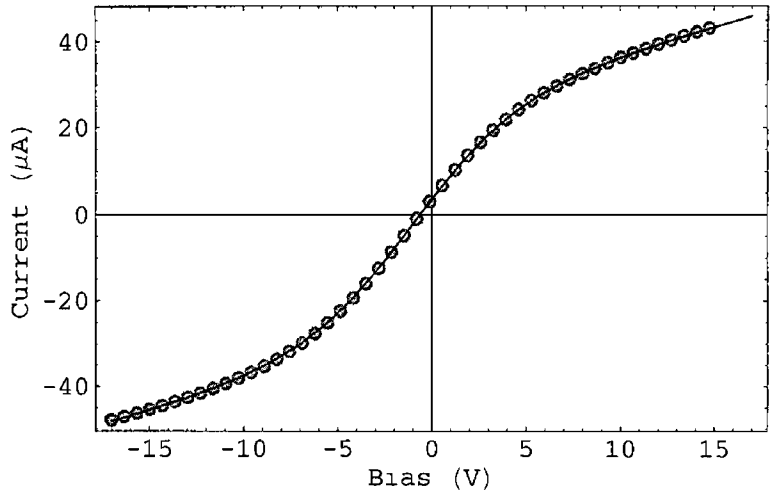

Figure 3 4 *Double Langmuir probe I-V characteristic curve taken in ARIS diffusion chamber, power 500 W, pressure 3 mTorr Argon Experimental (dots) and fit (continuous)*

3.1.4 The EEDF from a single probe

Introduction

In the next subsections we present the theory behind the EEDF estimation with a single probe, the technique we used in our experimental data and some considerations for the analysis of the data

Druyvestyen theory

Druyvesteyn [29] showed in 1930 that the EEDF could be extracted from a single probe I-V trace; here we present his calculation [35]. From equation (3.1) the electron current to a planar probe in a plasma (X-Y plane), biased at some voltage V_{bias} with $V_{\text{bias}} < V_P$ (plasma potential) for an arbitrary (unknown) electron velocity distribution function is

$$I_e(V_{\text{bias}}) = eA \int_{-\infty}^{\infty} dv_x \int_{-\infty}^{\infty} dv_y \int_{v_{\min}}^{\infty} dv_z v_z f_e(\mathbf{v}) \tag{3.10}$$

where

$$v_{\min} = \sqrt{\frac{2e(V_P - V_{\text{bias}})}{m}} \tag{3.11}$$

is the minimum velocity an electron needs to reach the probe due to the potential barrier built by the probe bias. In case of an isotropic distribution we can turn the integral into spherical coordinates for the velocity components

$$I_e = eA \int_{v_{\min}}^{\infty} dv \int_0^{\theta_{\min}(v_{\min})} d\theta \int_0^{2\pi} d\phi v \cos\theta v^2 \sin\theta f_e(v) \tag{3.12}$$

where $\theta_{\min} = \cos^{-1}(v_{\min}/v)$. Integrating (3.12) for θ and ϕ

$$I_e = \pi eA \int_{v_{\min}}^{\infty} v^3 \left(1 - \frac{v_{\min}^2}{v^2}\right) f_e(v) dv \tag{3.13}$$

With a change of variable $\epsilon = 1/2mv^2$ and calling the energy $E = V_P - V_{\text{bias}}$ (eV), which related to the bias voltage, the integral (3.13)

$$I_e = \frac{2\pi e^3}{m^2} A \int_E^{\infty} \epsilon \left[1 - \frac{E}{\epsilon}\right] f_e[v(\epsilon)] d\epsilon \tag{3.14}$$

Taking twice the derivative of this integral respect to the energy E we obtain a relation for the electron velocity distribution function ($f_e(\mathbf{v})$) and the second derivative of the electron current to the probe (in the electron retardation region)

$$\frac{d^2 I_e}{dE^2} = \frac{2\pi e^3}{m^2} A f_e[v(E)] \tag{3.15}$$

Note that the electron energy distribution function (EEDF) $g_e(E)$ is related to the electron velocity distribution function

$$g_e(E)dE = 4\pi v^2 f_e(v)dv \tag{3 16}$$

It is important to remark the difference between this two functions where one corresponds to the velocity and the other to the energy of electrons This are often confused or used with ambiguous notation in publications [42–45] Using the relation $v(E) = \sqrt{2eE/m_e}$ in (3 16) we obtain

$$g_e(E) = 2\pi \left(\frac{2e}{m}\right)^{3/2} E^{1/2} f_e[v(E)] \tag{3 17}$$

Combining equations (3 17) and (3 15) we obtain the EEDF relation to the second derivative of the single probe I-V trace

$$g_e(E) = \frac{4}{eA}\sqrt{\frac{mE}{2e}}\frac{d^2 I_e}{dE^2} \tag{3 18}$$

Notice that since $E = V_P - V_{\text{bias}}$ the derivatives $d^2/dV_B^2 = d^2/dE^2$ Therefore, taking the second derivative of the probe current respect to the bias potential equals the second derivative of the probe current respect to the corresponding energy $d^2I/dV_B^2 = d^2I/dE^2$ The energy (E) is in electron-volts (eV), therefore the electron temperature (T_e) is in electron-volts The density units (cm^{-3} or m^{-3}) depend on the units for the probe area

The electron density and averaged kinetic energy are calculated by integrating the EEDF

$$n_e = \int_0^\infty g_e(E)dE \tag{3 19}$$

$$\frac{3}{2}T_e = \langle E \rangle = \frac{1}{n_e}\int_0^\infty E g_e(E)dE \tag{3 20}$$

Relations (3 15) and (3 18) hold for any isotropic distribution function (non-Maxwellian distribution function in general), for any convex probe surface (cylindrical, spherical) and for any ratios T_e/T_i or R_p/λ_D [35]

The Maxwellian distribution function can be used as a reference since actual EEDFs in a plasma do not differ much from it Furthermore, standard analysis techniques assumed that electrons are in a Maxwell-Boltzmann equilibrium The Maxwellian EEDF formula is

$$g_e(E) = 2n_e\sqrt{\frac{E}{\pi T_e^3}}\exp\left\{-\frac{E}{T_e}\right\} \tag{3 21}$$

Very often it is useful to plot instead the logarithm of the electron energy probability function (EEPF) The EEPF relates to the EEDF as follows

$$P_e(E) = \frac{g_e(E)}{\sqrt{E}} \tag{3 22}$$

The EEPF shows Maxwellian distributions as a straight line with negative slope, thus it becomes very easy to identify non-Maxwellian distributions Notice that the second derivative of the electron current is directly proportional to the EEPF

$$P_e(E) \propto \frac{d^2 I_e}{dE^2} \tag{3 23}$$

A first look at the raw experimental data in logarithmic scale can give us an idea of the nature of the distribution

The theory presented requires good current-voltage characteristic second derivatives Experimentally, the traces usually contain some noise and it is known that numerical derivatives amplify the noise Therefore it usually requires digital or analog filtering and averaging a large number of samples to estimate the EEDF from numerical derivatives of the I-V trace [46] Another approach is to use analog differentiators [32] or the AC superimposing technique The last technique was preferred for the EEDF measurements in the diffusion chamber of ARIS This technique is introduced in the next section

The AC superimposing technique

Here we present the technique used for measuring the second derivative of the single probe I-V trace, used to obtain the electron energy distribution function (EEDF) This technique consists on adding a small AC voltage signal (V_{ac})§ to the usual DC bias voltage (V_{dc}) of the single Langmuir probe This technique is of wide-spread use now for EEDF measurements [28, 34, 47, 48] but has it origins in the 1930s and has evolved to the actual practise presented here, for an early historical overview refer to [49] The AC signal frequency is usually on the order of kilo-Hertz For the measurements presented in this thesis a 1 kHz signal was used

A probe is biased with a superposition of DC and AC voltages The total probe bias is

$$V_{bias} = V_{dc} + V_{ac} \sin 2\pi f t \tag{3 24}$$

The electron current collected by the probe is a function of the (DC and AC) bias voltage

$$I_e(V_{bias}) = I_e(V_{dc} + V_{ac} \sin 2\pi f t) \tag{3 25}$$

Making a Taylor expansion of the electron current and using trigonometric identities the probe current can be re-written

$$\begin{aligned} I(V_{bias}) = I(V_{dc}) + \frac{V_{ac}^2}{4}\frac{d^2I}{dV^2}\bigg|_{V_{dc}} + \frac{V_{ac}^4}{64}\frac{d^4I}{dV^4}\bigg|_{V_{dc}} + \\ + \left[V_{ac}\frac{dI}{dV}\bigg|_{V_{dc}} + \frac{V_{ac}^3}{8}\frac{d^3I}{dV^3}\bigg|_{V_{dc}} + \quad \right] \sin 2\pi f t + \\ - \left[\frac{V_{ac}^2}{4}\frac{d^2I}{dV^2}\bigg|_{V_{dc}} + \frac{V_{ac}^4}{48}\frac{d^4I}{dV^4}\bigg|_{V_{dc}} + \quad \right] \cos 4\pi f t + \end{aligned} \tag{3 26}$$

where the derivatives are evaluated at bias voltage equal to the DC bias (V_{dc}) The applied superimposed AC voltage signal produces harmonics on the probe current due to the variable probe sheath resistance Experimentally, a lock-in-amplifier is used to record the amplitude of the second har-

monic on the probe current for each value of the applied DC voltage bias The second harmonic ($4\pi f$) amplitude from equation (3 26) is

$$\mathcal{A}_{\text{2nd harm}}(V_{\text{dc}}) = \frac{V_{\text{ac}}^2}{4}\frac{d^2I}{dV^2}\bigg|_{V_{\text{dc}}} + \frac{V_{\text{ac}}^4}{48}\frac{d^4I}{dV^4}\bigg|_{V_{\text{dc}}} + \tag{3 27}$$

Neglecting the fourth and higher derivatives§, the second derivative is approximated

$$\frac{d^2I}{dV^2}\bigg|_{V_{\text{dc}}} \approx \frac{4\mathcal{A}_{\text{2nd harm}}(V_{\text{dc}})}{V_{\text{ac}}^2} \tag{3 28}$$

Substituting (3 28) into the Druyvesteyn relation (3 18) we obtain the EEDF

$$g_e(E) = \frac{16\mathcal{A}_{\text{2nd harm}}(V_P - E)}{eAV_{\text{ac}}^2}\sqrt{\frac{m_e E}{2e}} \tag{3 29}$$

where g_e is the electron energy distribution function (EEDF), m_e is the electron mass, A is the probe area and $E = V_P - V_{\text{dc}}$ is the energy (eV) Note that it is the electron current derivatives which yield the EEDF Separation of the electron and ion current is a typical problem in probe theory In general the ion current function remains unknown, even under well defined operating conditions (OML [50], Laframboise [37]) Experimentally the derivatives of the total current are taken so that errors are expect in the ion saturation current region (high energy electrons) where the ion current is larger than the electron current This problem sets a limitation on the energy range of the EEDF that can be measured

§ *Regarding the approximation from equation (3 27) to equation (3 28) it is important to note the following*

- *Formally the condition for the AC voltage amplitude would be given by comparison of the derivatives themselves This is, V_{ac} should be small enough so that the following condition is satisfied through the entire electron retardation region*

$$\frac{V_{\text{ac}}^2}{4}\frac{d^2I}{dV^2} \gg \frac{V_{\text{ac}}^4}{48}\frac{d^4I}{dV^4} \tag{3 30}$$

For a Maxwellian EEDF the electron current is exponential ($I_e \propto \exp\{(V_{bias} - V_P)/T_e\}$, equation (3 3)), therefore the derivatives are also exponential

$$\frac{d^2I}{dV^2} \propto \frac{\exp\{(V - V_P)/T_e\}}{T_e^2} \tag{3 31}$$

$$\frac{d^4I}{dV^4} \propto \frac{\exp\{(V - V_P)/T_e\}}{T_e^4} \tag{3 32}$$

Using these expressions in equation (3 30), we obtain the AC voltage amplitude condition

$$V_{ac} \ll 2\sqrt{3}T_e \simeq 3\ 5T_e \tag{3 33}$$

- *Last expression (3 33) is less restrictive that a direct comparison of the AC amplitude with the electron temperature In principle, the AC voltage amplitude should be smaller than the electron temperature, if not much smaller Though, the higher the order of the current derivative the smaller the derivative values The last effect relaxes the constraint Rundle et al [51] have found (by plotting V_{ac}^2 vs the second harmonic amplitude) that the AC amplitude could be as large as 3 V throughout the electron retardation region for measured EEDFs with average energy of 4-5 V, where the EEDFs shape were in between Maxwellian and Druyvesteyn*

- *No definition for the approximation condition has been found on publications referenced in this thesis, publications in which this technique has been used*

Plasma potential determination

In order to use the Druyvesteyn formula (3 28) and obtain the EEDF from the second derivative of the probe current, it is required to estimate the plasma

potential (V_P). The electron saturation section of the single probe I-V trace contains no information of the EEDF. Then determining the plasma potential (V_P), for which the electron current saturates, is important to scale correctly the EEDF. Although the idea of saturation is simple very often experimental data does not exhibit a clear saturation point. Usually it does not show a flat region on the I-V trace but an increasing current due to sheath expansion; see figure 3.2. The plasma potential determination is not trivial when there is no clear electron saturation. Typical approach requires to take the natural logarithm of the probe characteristic or the first and second derivatives. The plasma potential is estimated from this as one of the following:

- The bias voltage for the best graph criteria (manual selection of V_P).
- The bias voltage for which two linear fits, one of the electron saturation part and another of the electron retardation region, intersect (usually the probe current is converted to a logarithmic scale for this analysis).
- The bias voltage for which the first derivative of the probe current is maximum.
- The bias voltage for which the second derivative of the probe current is zero.
- The bias voltage for which the second derivative of the probe current is maximum (Rundle [51]).

These criteria, except for the last one, are widely used to determine the plasma potential. Also an emissive probe can be used to measure the plasma potential [35].

Ideally, the electron current should show a clear and sharp transition point from the retardation region to the electron saturation. This would be

also very clear on the first and second derivatives of the probe current The second derivative should show a discontinuity This discontinuity would be at the bias voltage equal to the plasma potential, the peak, the zero crossing of the horizontal axis and the minimum of the second derivative should all be at the same bias, the plasma potential Experimentally, this is never observed due to limited collection of low energy electrons This produces a roundness on the probe trace and its derivatives at the bias equal to the plasma potential And limits the resolution of the low energy range of the EEDF, this effect is reproduced by a kinetic model of a plasma in the vicinity of a cylindrical probe and presented in section 5 2 2 The voltage difference between the bias voltage for which the second derivative is maximum and zero should not be larger than the electron temperature

EEDF analysis

It is found often that EEDFs do not exhibit any complex structure, they are quite smooth and well behaved functions but simply do not fit a Maxwellian distribution Rundle [51] introduced an analytical function containing a small number of constants to model different distribution shapes

$$g(E) = C\sqrt{E}\exp\left(-BE^n\right) \tag{3 34}$$

Here n is related to the shape of the distribution, C is used to normalise the distribution and B determines the location of maximum If the distribution function is normalised to unity

$$\int_0^\infty g(E)\mathrm{d}E = 1 \tag{3 35}$$

Then the average energy results from the following integral

$$\langle E\rangle = \int_0^\infty Eg(E)\mathrm{d}E \tag{3 36}$$

Analytical integration of (3 35) and (3 36) yields expressions for C and B

$$C = \frac{n}{\langle E \rangle^{3/2}} \frac{\Gamma\left(\frac{5}{2n}\right)^{3/2}}{\Gamma\left(\frac{3}{2n}\right)^{5/2}} \tag{3 37}$$

$$B = \frac{1}{\langle E \rangle^{n}} \left\{ \frac{\Gamma\left(\frac{5}{2n}\right)}{\Gamma\left(\frac{3}{2n}\right)} \right\}^{n} \tag{3 38}$$

Where Γ is the Gamma function These expressions substituted in equation (3 34) yield an analytical formula for a generic EEDF in terms of the average energy

$$g(E) = \left\{ n \frac{\Gamma\left(\frac{5}{2n}\right)^{3/2}}{\Gamma\left(\frac{3}{2n}\right)^{5/2}} \right\} \frac{E^{1/2}}{\langle E \rangle^{3/2}} \times \exp\left(- \left\{ \frac{\Gamma\left(\frac{5}{2n}\right)}{\Gamma\left(\frac{3}{2n}\right)} \right\}^{n} \frac{E^{n}}{\langle E \rangle^{n}} \right) \tag{3 39}$$

This generic EEDF has a maximum (the most probable energy) An expression for the maximum is obtained by solving

$$\left. \frac{dg}{dE} \right|_{E_{\max}} = 0 \tag{3 40}$$

The expression for the maximum obtained is a function of n and the average energy

$$E_{\max}(n, \langle E \rangle) = \frac{\langle E \rangle}{2^{1/n} n^{1/n}} \left\{ \frac{\Gamma\left(\frac{3}{2n}\right)}{\Gamma\left(\frac{5}{2n}\right)} \right\} \tag{3 41}$$

The energy for the maximum in the distribution is equal to the average energy only when n equals $n_0 = 4\ 186$ For $n > n_0$ the average energy is smaller that the energy for the maximum $\langle E \rangle < E_{\max}$ and for $n < n_0$ the average energy is larger that the energy for the maximum $\langle E \rangle > E_{\max}$

Some particular values of B and n correspond to some known distributions

- Maxwell-Boltzmann distribution

$$B = \frac{3}{2\langle E \rangle} \quad \text{and} \quad n = 1 \tag{3 42}$$

- Druyvesteyn distribution

$$B = \frac{0\,547}{\langle E \rangle^2} \quad \text{and} \quad n = 2 \tag{3 43}$$

With this more suitable analysis, rather than simply assuming Maxwellian distributions, it is possible to calculate chemical rate processes with better confidence The correct values of this rates are important in many industrial applications and some diagnostic techniques (Laser-Induced-Fluorescence) Using this model to fit measured EEDFs, Heidenreich [34] reported differences in the estimated reaction rates, calculated with Maxwellian fits and the more general formula (3 34), of up to one order of magnitude

Limitations

When using the AC superimposing technique to measure the EEDF there is clearly a limitation on the low energy range of the EEDF due to limited collection of low energy electrons And there is also a limitation on the high energy end of the EEDF due to ion saturation current noise This is, when the ion current is comparable or larger than the electron current

The ion current is modulated by the AC signal, usually on the kilo-Hertz Though, not necessarily in phase with the electron current From equations (3 24) and (3 26) it is clear that the second harmonic of the electron current will be phase shifted by 90 degrees with respect to AC bias voltage This is used experimentally to put the lock-in-amplifier in phase with the electron current and record only the harmonic amplitude for the given phase shift This way the range of energy for which the EEDF measurement is acceptable is determined This methodology is discussed in section 5 1 1

We find that when using the AC superimposing technique to calculate the EEDF the range of energy of the measured EEDF which can use accepted

with confidence increases as the plasma density increases This is probably because the electron current is larger as the electron density increases This energy range also increases with the electron temperature, although the low energy resolution decreases with the temperature

3.1.5 Probe design, construction and electronics

Langmuir probe systems are basically composed of two parts, the electronics for driving the probe bias voltage and measuring the current signal and the probe themselves (probe tips, holders, feed-troughs and any electronic components on the probe shaft)

Single and double probe electronics are relatively different while the actual probes are based on a common design A selection of probe tips allows to use this common design to switch from single to double probe

In the following subsections we present the electronic circuit and probe designs used on the experimental campaigns in ARIS

Single probe

Some of the probe measurements were performed using a *SmartProbe* by *Scientific Systems* The *SmartProbe* system consists of a radio-frequency compensated probe and a probe driver and current recorder This system is PC controlled with *SmartSoft* software provided by *Scientific Systems* This system is capable of recording typical current-voltage characteristics as well as EEDF measurements based on numerical differentiation of the probe current

In spite of the EEDF measurement option of the *SmartProbe* it was decided that a sophisticated technique, AC superimposing technique, would be used to estimate the EEDF in ARIS This required to build a voltage

amplifier to bias the probe This amplifier was designed to output variables voltage in the range of ±100 V Figure 3 5 shows a diagram of the amplifier and the current measurement circuit

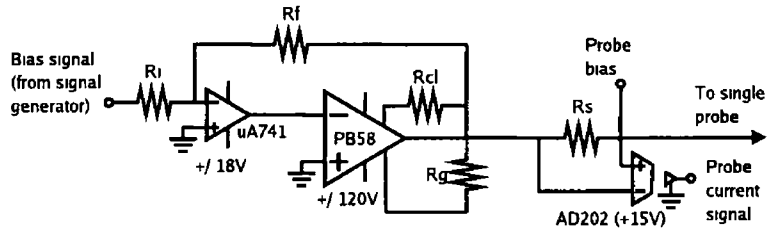

Figure 3 5 *Single Langmuir probe amplifier circuit and current signal measurement circuits digram*

The amplifier is a double stage voltage amplifier based on a low voltage operational amplifier (μA741) and a high power amplifier (PB58, *Apex Microtechnology*) The design has been based on APEX technical data sheet [52] The amplifier output voltage is approximately one order of magnitude larger than the input voltage The input voltage used is a mixture of a small AC signal and a DC offset, this is generated with a waveform generator

The current is calculated from measured voltage across a resistor in series with the probe An isolation amplifier (AD215, *Analog Devices*) with unity gain is used to isolate the voltage signal, which is floating The resulting signal is recorded with a data acquisition card and input into a lock-m-amplifier to extract the second harmonic of the probe current The bandwidth of the isolation amplifier covers from DC to tens of kilo-Hertz, this limits the frequency of the superimposed AC signal that can be used Phase shift in the current signal due to the isolation amplifier has to be corrected as well as possible attenuation

An auxiliary floating probe is usually placed in the plasma close to the

driven probe The purpose of this floating probe is to measure any disturbance in the plasma potential when the driven probe is in electron saturation current When the driven probe is in the electron saturation current region the plasma electron population could be depleted, which would raise the plasma potential To overcome this problem the bias voltage is corrected with the changes in voltage measured by the floating probe The voltage difference between the plasma and the floating potential is proportional to the electron temperature in a plasma with a Maxwellian EEDF In this case any change in the plasma potential is followed by a similar change in the plasma potential provided the electron temperature remains constant This is not valid for non-Maxwellian EEDFs, though it is still used as a reference

Double probe

In the case of a double Langmuir probe, the probe tips are isolated from ground and biased one respect to the other one Therefore the probe bias supply must not be ground referenced Since output voltage signals from a signal generator or a data acquisition card are ground referenced it is necessary to design a special circuit to drive the probe and measure the current The circuit developed to drive the probe and measure the probe current is shown in figure 3 6

This double Langmuir probe circuit is designed with two isolation amplifiers (AD202, *Analog Devices*), which completely isolate the double probe circuit from ground as required, and four operational amplifiers (OP07 and OP27, *Analog Devices*) The circuit is full battery powered and requires an external input voltage (range ±1 8 V) that is amplified with a gain of 10 (range ±18 V) The probe current is measured with a resistor (100 k-1 MΩ) The voltage across the resistor (current signal) is passed trough an isolation

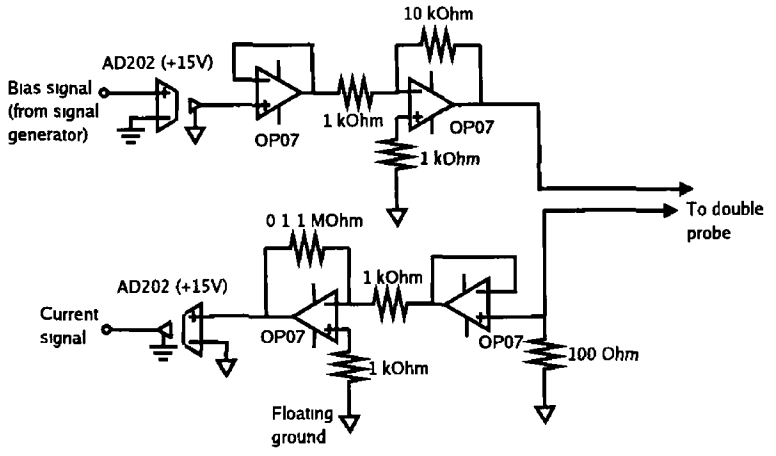

Figure 3 6 *Double Langmuir probe circuit diagram with floating ground*

amplifier (AD202, *Analog Devices*) with unity gain (output range ±4 V)

The input voltage for the double probe driver is provided by either a waveform generator or a data acquisition card In either case the signal can be averaged over many sweeps and/or samples A basic limitation on the circuit is amplitude attenuation and phase shift of the output current signal and the probe bias due to the limited bandwidth of the isolation amplifiers used Still the probe can be driven with triangular waveforms of a few tens of Hertz The probe system is controlled with a Labview routine, a fit of the recorded trace to equation (3 9) is implemented such that it allows to estimate the electron temperature and the ion saturation current in real time

The double probe is self-biased in the electron retardation region and the ion saturation current region Therefore the perturbation by the probe to the plasma is less than with a single probe And no floating probe is required Although, it is often used to estimate the electron temperature and ion saturation current without ramping the probe bias, such array of three probe tips is known as a triple probe

Common probe design

Single and double Langmuir probes are known to be susceptible to radio-frequency oscillations in the plasma potential [27, 53, 54] The effects of radio-frequency voltage oscillations across the sheath have been theoretically and experimentally studied by Garscadden and Emeleus [54] and Boschi and Magistrelli [53] One important result in references [53, 54] is that for moderate to low amplitude of the radio-frequency oscillations on the plasma potential the electron temperature can be correctly estimated with a single probe, without any type of compensation Is has also been theoretically shown by Annaratone et al [55] that the electron temperature can be correctly estimated with a double probe, without compensation

In spite of this, the plasma density can not be properly estimated with simple probes, probes without radio-frequency compensation This is why many researchers have focused on compensating the radio-frequency noise to the probe Two types of compensation have been developed, active and passive

In active compensation, a radio-frequency bias is added to the usual low frequency probe bias The amplitude and phase of the RF bias is explored until the floating potential of the current-voltage characteristic is maximised, this criteria is based on the theoretical results presented in reference [53] The bias radio-frequency is the same as the one used to excite the discharge Single and double probes have been actively compensated [55, 56]

In passive compensation, resonant circuits are added to the usual bias and current measurement probe circuit These resonant circuit elements can be placed outside the probe [57, 58], with the rest of the electronics, or inside the probe holder, as close to the probe tip as possible [32, 46, 59–61] In any case it is usual to add a capacitively coupled electrode, considerably larger

than the probe tip, to drop the RF impedance of the probe sheath

Passive compensation was compared to active compensation by Annaratone and Braithwaite [60] Their results showed that passive compensation provide a wider RF bandwidth for compensation and that the setup is considerably simpler and cheaper This is why passive compensation is the preferred compensation type implemented in commercial probes (*SmartProbe* by *Scientific Systems* and *Hiden ESPion Langmuir Probe* by *Hiden Analytical*)

The ARIS source is inductive and has a large ground surface area exposed to the plasma, therefore small RF oscillations on the plasma are expected *A large grounded area produces a low impedance to ground* According to references [53] and [55] there is no need to implement RF compensation in single or double probes if only the electron temperature is to be measured Though, for EEDF measurements it is better to implement some type of compensation to prevent distortion of the low energy range of the EEDF It is important to note that, even with full compensation in an RF plasma or with a simple probe in a DC plasma, it is difficult to measure the low energy range of the EEDF due to limited collection of low energy electrons, those with energies below the electron temperature

A general probe design for either type of probe was developed Passive compensation is implemented in the general design Two probe tips are exposed to the plasma, the probe tips are capacitively coupled (5nF, 1 35 Ω for 13 56 MHz) so that both tips follow the same RF oscillations Both tips are connected back to a pair of vacuum BNC feed-troughs to allow connection with external circuit A set of radio-frequency inductors, self-resonant at frequencies close to 13 56 and 27 1 MHz, are installed in-line close to the probe tips after the coupling capacitor These inductors have high impedance at the fundamental and second harmonics When the RF

impedance of the sheath is much smaller than the inductor impedance, the probe tip can follow the oscillation in the plasma potential Figure 3 7 show a schematic (not to scale) diagram of the general probe design A stainless steel tube holds a ceramic double bore piece which holds the probe tips The inductors (100 and 22 μH) are self-resonant at frequencies close enough to the first and second RF harmonics The capacitor and inductors are placed as close as possible to the ceramic tube to avoid stray capacitance inside the stainless steel tube The length of the ceramic and steel tubes are on the order of several centimetres

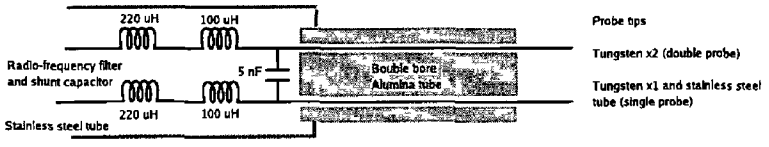

Figure 3 7 *General probe design with radio-frequency inductors and coupling capacitor*

For single probes, a tungsten wire (0 2 mm radius) is used as the driven tip while the second tip is made of a larger area stainless steel tube The probe tips is this case have to be separated by several millimetres to avoid interference, the driven tip is further inserted into the plasma, held by a thiner ceramic tube The second tip is left to float in the plasma The purpose of this tip is to reduce the RF sheath impedance and to follow the floating potential This improves the compensation by the self-resonant inductors and provides a measure of the effect of the probe on the plasma potential when the probe is biased into electron saturation *(If the EEDF is Maxwellian then any changes in the plasma potential are followed by the floating potential Therefore, in order to measure perturbation on the DC plasma potential it is enough to measure the floating potential)*

For double probes, both probe tips are same size and made of tungsten

wire (0 2 mm radius) The coupling capacitor makes both tips to follow the same RF oscillations and reduce the RF sheath impedance The RF self-resonant inductors make the probe tips to be a high RF impedance and force the tips to follow the RF oscillations of the plasma potential

Basic materials used to build the probes

- Probe tips (cylindrical probe), thin tungsten wire supplied by Goodfellow (W 005335 Tungsten, straight wire, 0 38mm diameter)
- Insulating holders for the probe tip, ceramic Alumina (Al_2O_3), supplied by OMG UK Limited (tube OD 0 8 ID 0 4 Cat No 121 11080 0)
- Stainless steel tube, support for ceramic, supplied by Radionics (Stainless Steel Stock, Seamless tube 316L to ASTM 269 1/4 in Stock no 682-905)
- PTFE (Teflon) insulated wire supplied by Farnell (BSG3G210 Type A 1/0 4mm (0 128mm^2) 26 AWG)

3.2 Summary

The most basic probe theories for single and double Langmuir probes have been presented Druyvesteyn theory for electron energy distribution function estimation from a single probe voltage-current characteristic has been presented And is complemented with the AC superimposing technique for EEDF measurements Finally, details of probe electronics, RF compensation and probe design have been presented

3.3 Cavity Ring Down Spectroscopy

3 3.1 Introduction

Cavity Ring Down Spectroscopy (CRDS) is a non invasive absorption technique which can be applied to the detection of very dilute or weakly absorbing species [62] This technique measures the rate of absorption of a light pulse emitted from an optical cavity which consists of two highly reflective spherical mirrors and contains the absorbing sample The sensitivity of this technique is dependent on mirror reflectivity where path lengths of several kilometres can be achieved

As a non invasive diagnostic CRDS represents and alternative diagnostic to photo-detachment (Bacal [63]) when detecting negative ion species, such as negative hydrogen ions (H^-) In the case of negative ions it is not absorption but a photo-detachment process which leads to the laser beam decay

CRDS has been used to measure line-integrated, negative hydrogen ion density in a multi-cusp negative ion source [64] and in a capacitive RF discharge [65] Here we use the technique to measure negative hydrogen ion density in the diffusion region of the ARIS experiment (inductively coupled)

3.3.2 Theory

A laser is pumped into a cavity which consists of a set of two highly reflective mirrors (R>0 9995) The laser beam that leaks into the cavity follows multiple reflections leaking back to the laser source on one end and to a photo multiplier on the other end The photo-multiplier signal is proportional to the beam light intensity This intensity decays exponentially in time as it leaks out of the cavity –at both ends– and it is absorbed by some particular

specie(s) in the cavity

$$I(t) = I_o \exp\{-(\text{No of round trips}) \quad (\text{Loss per reflection}) \quad (\text{No of reflections per round trip})\} \tag{3 44}$$

Where I_o is the initial intensity inside the cavity If the cavity is empty then the losses are only due to leakage at the mirrors so the intensity decay is

$$I(t) = I_o \exp\left\{\frac{tc}{2L} \quad (1 - R) \quad (2)\right\} \tag{3 45}$$

where c is light speed and L is the cavity length The cavity base ring down time (τ_o, for an empty cavity) is

$$\tau_o = \frac{L}{c(1 - R)} \tag{3 46}$$

This is the time it takes the light intensity to decay to $1/e$ (inverse of the Neperian number) of its original value For example if the reflectivity is 0 9998 and the cavity length 1 m the number of round trips after a time equal to the ring down time is 2500, corresponding to a path length of 5 km This long path length is an indicator of the extreme sensitivity associated with the diagnostic

If any speciesthat would absorb the laser radiation (for the given laser wavelength) is present in the cavity then the light intensity decays

$$I(t) = I_o \exp\left\{\frac{tc}{2L} \quad ((1 - R) + n\sigma d) \quad (2)\right\} \tag{3 47}$$

where n is the density of the species(m^{-3}), σ is the absorption cross section (m^2) at the laser wavelength and d is the absorption path length (m) The ring down time of the filled cavity (time for which the intensity decays $1/e$ of its original intensity) is

$$\tau = \frac{L}{\{(1 - R) + n\sigma d\}c} \tag{3 48}$$

From equations (3 46) and (3 48) the absorbing speciesdensity results

$$n = \frac{L}{\sigma c d}\left(\frac{1}{\tau} - \frac{1}{\tau_o}\right) \tag{3 49}$$

Absolute densities can be measured provided the cross section (σ) for the absorption process, the absorbing path length (d, length of the beam exposed to the absorbing specie) and the cavity length (L) are known No intensity calibration is required but to ensure the photo-multiplier is not operating under nonlinear regime

Figure 3 8 shows a basic diagram of the CRDS diagnostic technique

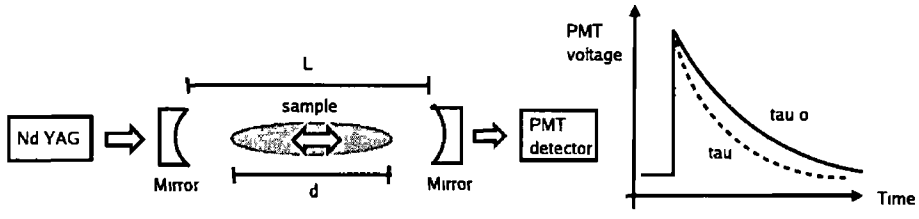

Figure 3 8 *Basic diagram of the CRDS diagnostic*

3.3 3 Analysis

The CRDS signal recorded with the photo multiplier is expected to be an exponentially decaying signal If the cavity is misaligned or the focal length of the mirrors are smaller than the cavity length, the signal may differ from the expected exponential behaviour The CRDS signal also contains a fair amount of noise whether it has been recorded with the plasma background light or not The plasma background light is attenuated with a small band-pass filter for the particular wavelength of the laser and a neutral density filter, the last one reduces the overall light intensity (laser beam and plasma)

The ring down time of a CRDS signal is calculated after a fit of the data to an exponential function or after a fit of the logarithm of the signal to a

linear function The ring down time is calculated with (τ) and without (τ_o) the absorbing species in the cavity Using the absorption cross section (σ), absorption path length (d), cavity length (L) and the calculated ring down times, the density of the absorbing speciesis calculated with formula (3 49)

Formula (3 49) is a non linear function of the ring down times The larger the difference in the ring down time ($\Delta\tau = \tau_o - \tau$), the larger the density of the absorbing specie Note that $\tau < \tau_o$, the absorption reduces the ring down time It is also clear from this formula that the larger the cross section for the absorption (σ) and the larger the ratio d/L the more sensitive is the diagnostic for density measurements This means that the laser wavelength should be chosen such that the cross section is as large as possible and that the cavity length should be as small as the sample length Experimentally it is not always possible to select the wavelength with such freedom and the length of the cavity must be large enough to prevent plasma affects on the mirror reflectivity (R) The base ring down time is a function of the reflectivity, equation (3 46) The smaller the base ring down time (τ_o) the less sensitive the technique is This might not be obvious from formula (3 49), but it can be shown with an example (figure 3 9 and table 3 1)

Figure 3 9 shows the negative ion density (n_{H^-}) as a function of the ring down time (τ) for cavity length 1 meter, absorption path length 40 cm, cross section of H^- electron detachment at 532 nm (2 33 eV) $3\,3 \times 10^{-21}$ m^2 and base ring down times 15, 20 and 30 μs The larger the base ring down time (larger reflectivity), the more sensitive is the technique Table 3 1 shows that for larger base ring down time, the larger the ring down time difference ($\Delta\tau = \tau_o - \tau$) expected for a given target density This is, for a large base ring down time, in order to measure a small density it is not required as high precision in the ring down time measurement as for lower base ring down

times

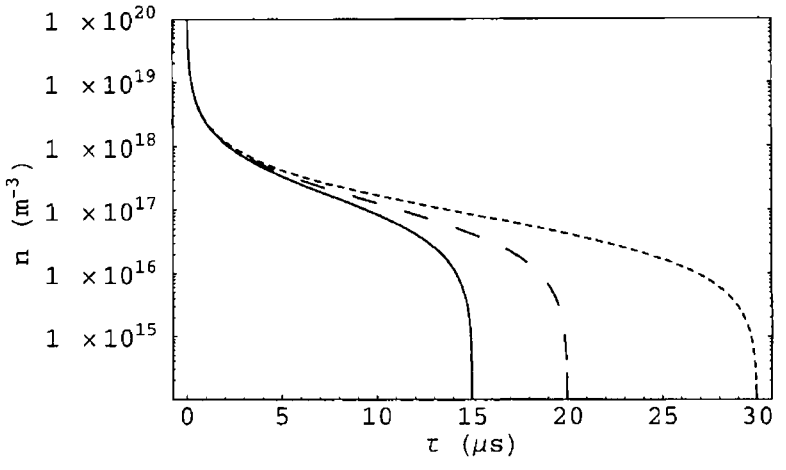

Figure 3 9 *Absorbing speciesdensity as a function of the ring down time (τ) for three different base ring down times 15, 20 and 30 μs (equation (3 49)) For cavity length 1 m, absorption path length 40 cm and photo detachment process cross section* $3\,3 \times 10^{-21}$ m^2 *(laser wave length 532 nm, photon energy* $\sim 2\,33$ *eV)*

The sensitivity of the diagnostic is essentially limited by the precision of the calculated ring down times ($\delta\tau_o$ and $\delta\tau$) This deltas are usually around ± 5 % of the ring down time, and represent an intrinsic noise on the CRDS signal The error on the density is calculated

$$\delta n = \left|\frac{\partial n}{\partial \tau}\right| \delta\tau + \left|\frac{\partial n}{\partial \tau_o}\right| \delta\tau_o \tag{3 50}$$

Taking the derivatives from equation (3 49) the error on the density

$$\delta n = \frac{L}{\sigma c d}\left(\frac{\delta\tau_o}{\tau_o^2} + \frac{\delta\tau}{\tau^2}\right) \tag{3 51}$$

This function is plotted in figure 3 10 for a base ring down time of 30 μs assuming $\delta\tau_o = \delta\tau$ for different $\delta\tau = 1, 0\,1, 0\,01$ and $0\,001$ μs (top to bottom curves) This should be compared to figure 3 9 for the same base ring down time Notice the overall error in the density drops as the errors in the ring

Table 3 1 *Ring down time difference ($\Delta\tau = \tau_o - \tau$) for negative ion densities $n_{H^-} = 10^{14}$-10^{17} m^{-3} For cavity length 1 m, absorption path length 40 cm and photo detachment process cross section 3 3 $\times 10^{-21}$ m^2 (laser wave length 532 nm, photon energy $\sim$ 2 33 eV)*

n_{H^-} (m^{-3}) $\rightarrow$	10^{14}	10^{15}	10^{16}	10^{17}
τ_o (μs)	$\Delta\tau$ (ns)	$\Delta\tau$ (ns)	$\Delta\tau$ (μs)	$\Delta\tau$ (μs)
5	0 99	9 88	0 097	0 83
10	3 96	39 44	0 381	2 84
15	8 90	88 57	0 841	5 59
20	15 83	157 16	1 468	8 84
30	35 60	352 22	3 186	16 29

down time ($\delta\tau$) drop down to about 1 ns Also the error in density grows as the ring down time difference increase, the last corresponds to an increase in density

We found on the ARIS experiment that the negative ion density is on the order 10^{14} m^{-3} for which the error on the ring down times is required to be on the order of nano seconds Experimentally the intrinsic noise on the produces a spread in the ring down time up to 1 μs (standard deviation) We improved the analysis of the data in order to reduce the statistical spread Figure 3 11 shows the sequence of the data analysis starting with the raw data (step a) First the recorded CRDS signal offset is corrected to zero with the DC voltage measured before the laser pulse enters the cavity and the time is inverted so that the signal grows exponentially rather than decay

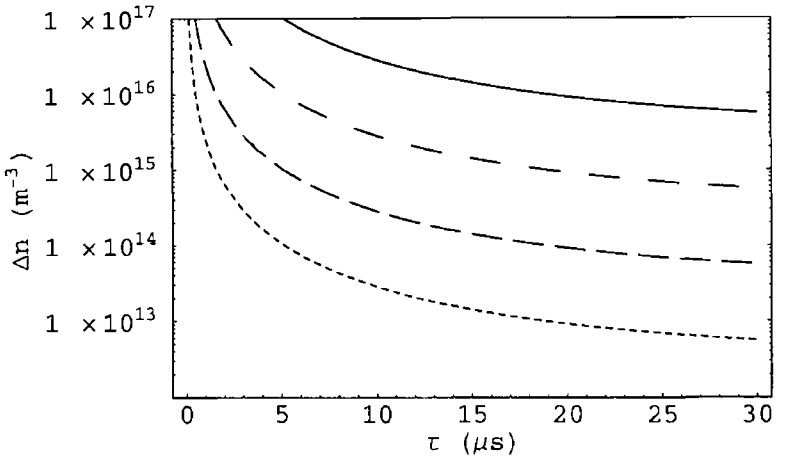

Figure 3 10 *Absorbing speciesdensity error as a function of the ring down time for base ring down time 30 μs for different $\delta\tau_o = \delta\tau$ = 1, 0 1, 0 01 and 0 001 μs top to bottom curves respectively (equation (3 51)) For cavity length 1 m, absorption path length 40 cm and photo detachment process cross section* $3\,3\times10^{-21}$ m^2 *(laser wave length 532 nm, photon energy* $\sim 2\,33$ *eV)*

(step b) Second the signal is time integrated (step c)

$$V_{\mathrm{CRDS,int}}(t) = \int_{to}^{t} V_{\mathrm{CRDS}}(t')\mathrm{d}t' \tag{3 52}$$

Here we use the fact that the integral of an exponential function remains an exponential function with the same exponential constant Also the advantage that numerically integrating data tends to reduce the noise (as opposed to differentiation which amplifies the noise) Finally the logarithm of the integrated signal is taken and fitted to a linear function (step d), the inverse of the slope corresponds the ring down time We have observed that only one numerical integration is sufficient to reduce the noise and that subsequent integrations do not reduce the noise any further Regular analysis of the CRDS signal lacks the numerical integration (bunch of references neglecting mostly the analysis technique)

Figure 3 12 shows a sample CRDS signal which is treated as outlined here

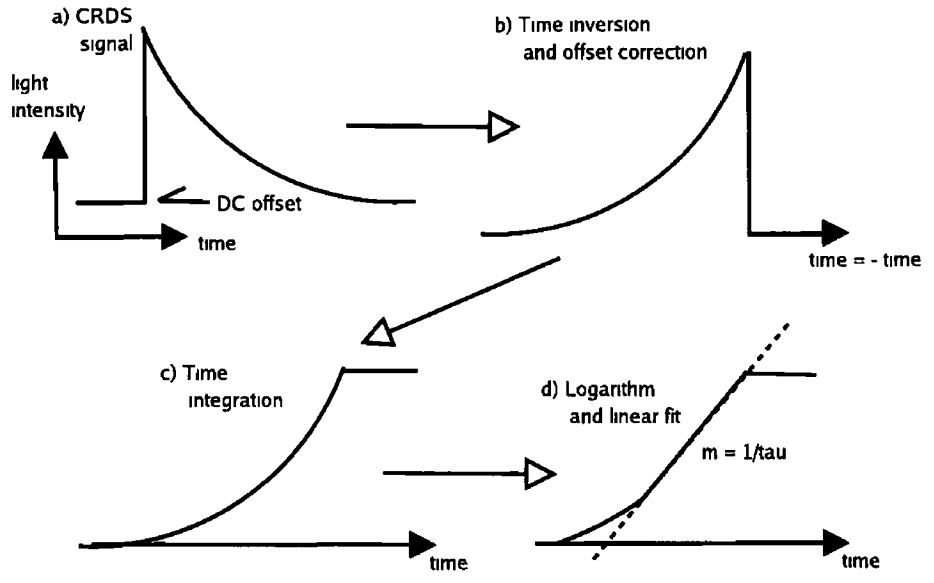

Figure 3 11 *Analysis sequence of CRDS signal a) CRDS signal, b) time inversion and offset correction, c) time integration and d) logarithm and linear fit*

Figure 3 12a is a one shot sample set of raw data (arbitrary units), proportional to the light intensity captured by the photo multiplier and recorded with a digital scope Remmember that the vertical scale is not important, it is the ring-down-time what is being measured The scope is triggered with the fast rise of the signal, the record runs for a 100 μs and consists of one thousand samples The trigger is time delayed so that the first 10 μs of the record are previous to the laser beam, this is required to calculate the vertical offset of the signal Figure 3 12b shows the CRDS signal time inverted (dots) and the integrated signal (continuous), traces are dc offset to allow better comparison Before the integration the CRDS data is offset corrected The exponential characteristic of the signal is reproduced by the integrated signal, simultaneously the noise around the signal is removed Figure 3 12c shows the natural logarithm of the CRDS signal (dots) and the integrated

CRDS signal (continuous), traces are dc offset to allow better comparison In either case the linear behaviour fails from 0 to 40 μs The ring down time of the signal equals the inverse of the slope of the logarithm of the CRDS signal In this particular example the ring down time is $\sim$ 20 μs The time section of the logarithm curves used for the linear fit is between 50 and 90 μs, about two times the ring down time section length The simply treated curve exhibits scattering of the samples while the integrated curve is consistently noiseless This reduces the statistical spread of the ring down time after the analysis of a number of CRDS signals, therefore the number of statistical ring down time samples required to achieve certain sensitivity is reduced Note the absolute values of the light intensity of the CRDS signal is not important but only the decay characteristic time (ring down time)

Following the analysis presented, the standard deviation drops from more than 1 μs to less than 0 5 μs in typical measurements (532 nm laser beam, $\tau_o \sim$ 20-30 μs) In spite of this improvement it is still not enough to make an accurate measurement of the negative ion density on the order 10^{14} m^{-3} A large number of pairs (τ_o, τ) are recorded and averaged The standard deviation of the record

$$\sigma_{\text{dev}} = \sqrt{\frac{\sum_i^N (\tau_i - \langle\tau\rangle)^2}{N-1}} \tag{3 53}$$

The standard error of the record

$$\delta\tau = \frac{\sigma_{\text{dev}}}{\sqrt{N}} \tag{3 54}$$

Where N is the number of pairs (τ_o, τ) A record of 50-100 thousand sample pairs is required in order to achieve a standard error of the order of a few nano seconds, data collection of large number of samples take several hours

In the ARIS experiment the density of negative hydrogen ions is low compared to the expected densities on the order of $10^{15} - 10^{16}$ m^{-3} in actual

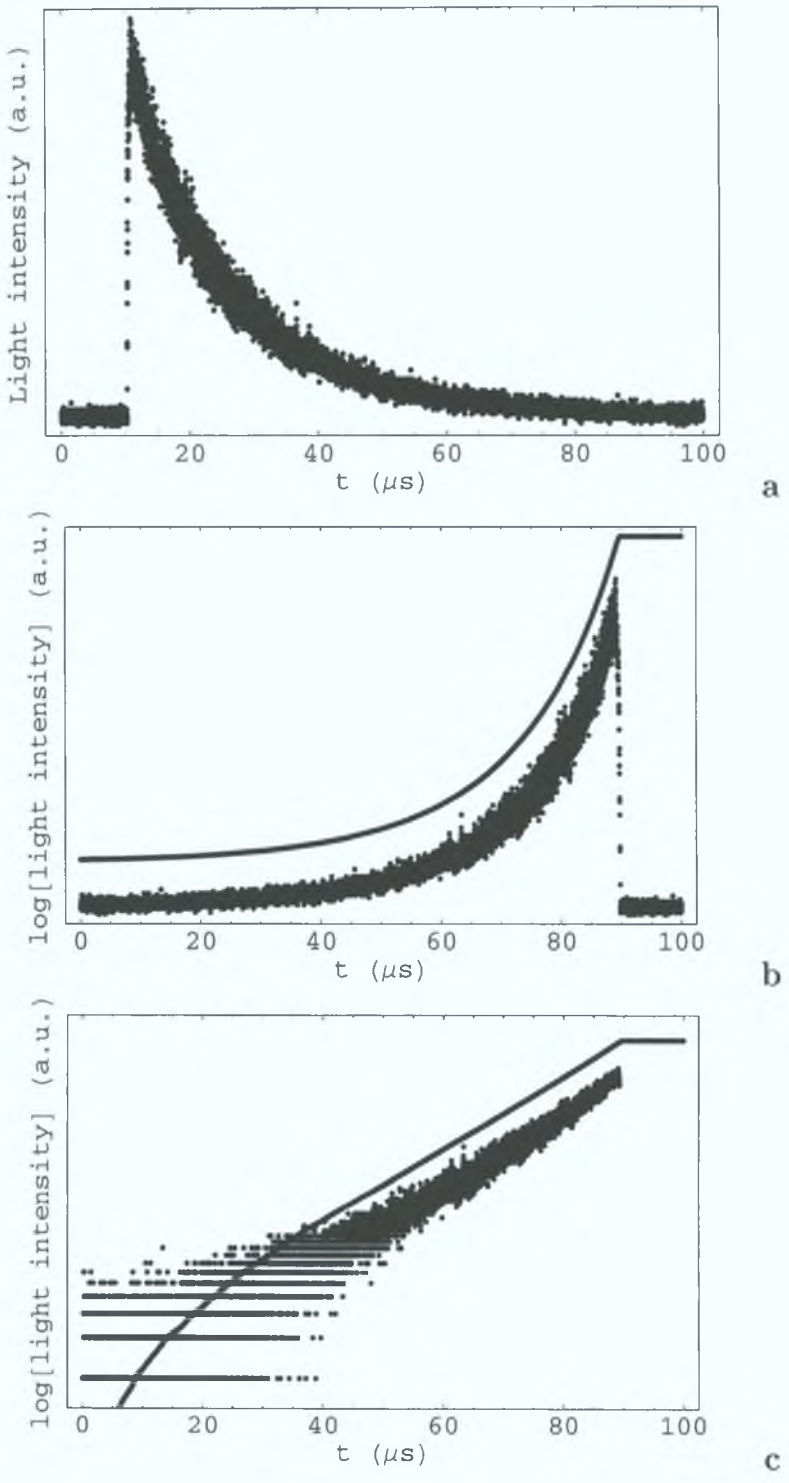

Figure 3.12: *Example of analysis of a CRDS signal: a) single shot raw data, b) time inverted raw data (dots) and numerical integration of the inverted data (continuous), and c) logarithm of the raw data (dots) and integrated data (continuous). Small vertical offset on figures b) and c).*

test negative ion sources (CamembertIII, Batman, Kamaboko, etc) The accuracy constriction of the technique for negative ion densities on this experiments would drop as the expected density is higher this results in smaller number of samples required and subsequently short data collection time

3 3 4 Summary

We have presented the CRDS technique basic theory and improved the analysis We have shown that by performing a numerical integration of the CRDS signal the noise on the data is reduced This reduces the shot to shot variation on the ring down time due to noise on the signal The ring down time is consistently more accurate when including the numerical integration of the signal in the analysis for a given number of samples We believe this improvement in the analysis will be of benefit to other researchers on the field using the CRDS technique diagnostic In particular the hydrogen negative ion (H^-) density measurements, where CRDS represents a non invasive option to photo detachment (Bacal [63])

CHAPTER 4

Modelling

Here we present a description of a single particle model and a full kinetic model

The first model is developed to study single particle dynamics of a charged particle in the presence of a magnetised boundary It is a two-dimensional collisional model Single particle trajectories governed by a magnetic field (no electric field) are modelled in a the presence of a buffer gas

The second model is developed to study the self-consistent evolution of a plasma in the vicinity of a cylindrical Langmuir probe and the particle collection by the probe surface It is a one-dimensional, electrostatic model Electrons and ions trajectories governed by an electric field (no magnetic field) are modelled in the presence of a buffer gas

4.1 Single particle modelling

4.1.1 Introduction

We present a model developed to study single particle interaction with a magnetised boundary The magnetised boundary is designed to emulate a simplified magnetic multi-cusp as the one set-up on the end plate of the diffusion chamber in ARIS (figure) Checker-board (multi-cusp) configuration of permanent magnets provide enhanced magnetic confinement in bucket sources as described in chapter 1 The multi-cusp set-up is designed to produce a highly magnetised region m the vicinity of the wall with a low field penetration into the plasma volume (magnetic field free) The dynamics of a charged particle in the plasma bulk is not affected by the magnetic field When the charged particle approaches the magnetised boundary depending on the field intensity, background pressure, particle mass and energy it may be trapped by the field, loss to the wall (mainly at the cusp) or bounced back to the plasma bulk We have done a statistical study of the transport of a large sample of charged particles in the transition region from the plasma bulk to the magnetised boundary neglecting electric fields The work is repeated for a wide range of background pressures to study collisional effects on the particles transport

The charged particles modelled are electrons and the background gas is molecular Hydrogen Collisional effects are studied with particle-neutral cross section for elastic collisions ($e^- + H_2$) The particles are loaded from the plasma boundary –where the magnetic field is negligible– with random energies such that the energy distribution of the sample is Maxwellian The particles trajectories are tracked and analysed

The magnetic field is determined from a set of modelled magnetic bars

The magnetic bars are orientated to the plasma with the same polarity set for even bars and inverse polarity for odd bars

4.1.2 The model

The magnetic field

The magnetic field produced by a magnetic bar is effectively modelled with the magnetic field from a current density distribution The field of an infinitely long magnetic bar is modelled with the magnetic field due to two opposing current densities as shown in figure 4 1 The currents are uniformly

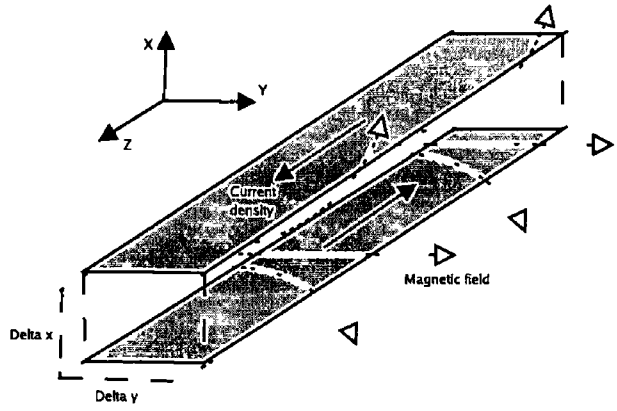

Figure 4 1 *Magnetic field of an infinitely long magnetic bar modelled as the magnetic field induced by an infinitely long flat current density loop*

distributed on the side surfaces of the bar If the bar is long enough to neglect the end effect, the magnetic field due to the current density at each side is analytical The current density on one side

$$\mathbf{J}(\mathbf{r}) = (0, 0, \delta(x)J_z) \quad -\Delta y < y < 0 \tag{4 1}$$

where $\mathbf{r} = (x, y, z)$, the bar side is at $x = 0$, $y[-\Delta y, 0]$ and is infinitely long in the Z axis (ends neglected) The magnetic field is calculated from the

integral

$$\mathbf{B}(\mathbf{r}) = \frac{\mu_o J_z}{4\pi} \int\int\int \delta(x')\mathbf{k} \times \frac{\mathbf{r}-\mathbf{r}'}{|\mathbf{r}-\mathbf{r}'|^3} dx'dy'dz' \tag{4.2}$$

Integrating on x the integral is reduced

$$\mathbf{B}(\mathbf{r}) = \frac{\mu_o J_z}{4\pi} \int\int dy'dz' \left(\frac{y-y'}{|\mathbf{r}-\mathbf{r}'|^3}\mathbf{i} - \frac{x}{|\mathbf{r}-\mathbf{r}'|^3}\mathbf{j} \right) \tag{4.3}$$

With analytical solution

$$B_x(\mathbf{r}) = \frac{\mu_o J_z}{4\pi} \left\{ -\ln\left(x^2+y^2\right) + \ln\left(x^2+(y-\Delta y)^2\right) \right\} \tag{4.4}$$

$$B_y(\mathbf{r}) = \frac{\mu_o J_z}{4\pi} \left\{ 2\tan^{-1}\left(\frac{y}{x}\right) - 2\tan^{-1}\left(\frac{y-\Delta y}{x}\right) \right\} \tag{4.5}$$

Combining the field components (4.4) and (4.5) we model the magnetic field of a infinitely long magnetic bar.

$$B_{x\text{bar}}(x,y) = B_x(x+\frac{\Delta x}{2},y) - B_x(x-\frac{\Delta x}{2},y) \tag{4.6}$$

$$B_{y\text{bar}}(x,y) = B_y(x+\frac{\Delta x}{2},y) - B_y(x-\frac{\Delta x}{2},y) \tag{4.7}$$

The magnetic bar dimensions used on the single particle model are $\Delta y =$ 1.7 cm and $\Delta x = 1$ cm. The bar faces are centred at (0,0) and (0,$-\Delta y$). The current density J_z is set such that the magnetic field intensity at the face centres equals 600 Gauss. Using the magnetic field of one bar as a base, the magnetic field of different multi-cusp arrays of permanent magnets are modelled. Three-dimensional plots of three different magnetic cusps are show in figure 4.2.

a Magnetic field due to only two bars separated by $2h$. The field is orientated on the Y axis and the polarity of one bar is inverted with respect to the other (N-S). Figure 4.2a shows the magnetic bars and the field lines and field intensity on the X-Y plane.

$$B_{x\text{total}}(x,y) = B_{x\text{bar}}(x-h,y) - B_{x\text{bar}}(x+h,y) \tag{4.8}$$

$$B_{y\text{total}}(x,y) = B_{y\text{bar}}(x-h,y) - B_{y\text{bar}}(x+h,y) \tag{4.9}$$

b Magnetic field due to only four bars separated $2h$ from each other Similarly to case (a) the field is orientated on the Y axis and the polarity of the even bars is inverted respect to the odd ones (N-S-N-S) Figure 4 2b shows the magnetic bars and the field lines and field intensity on the X-Y plane Note the magnetic field lines connect contiguous bars but can also connect non-contiguous bars with opposite polarity This is due to the limited number of bars and produces regions of null field (cancelled) and reversed field (outer set of bars field cancel/reverse the internal set of bars field)

$$B_{x\text{total}}(x,y) = B_{x\text{bar}}(x-h,y)-B_{x\text{bar}}(x+h,y)-B_{x\text{bar}}(x-3h,y)+B_{x\text{bar}}(x+3h,y) \tag{4 10}$$

$$B_{y\text{total}}(x,y) = B_{y\text{bar}}(x-h,y)-B_{y\text{bar}}(x+h,y)-B_{y\text{bar}}(x-3h,y)+B_{y\text{bar}}(x+3h,y) \tag{4 11}$$

c Field of a large number of cusps, modelled by periodically evaluating the field only due to the two nearest magnetic bars Cancelled and reversed field regions are removed this way Also the field represents symmetric cusps

Configurations (a) and (c) where implemented for the single particle model Case (b) was dropped because the cusps are not symmetrical, it would require more magnetic bars to achieve so and would demand longer computational time Configuration (b) requires fields (4 4) and (4 5) to be evaluated eight times each while (a) and (c) only requires 4 evaluations each Cases (a) and (b) represent a non-symmetric and a symmetric cusp configuration respectively The simulation results of case (a) and (b) are compared with field free model runs The rectangular region of space (X-Y plane) modelled is shown bounded by a dashed border on figure 4 2 On the model the

bars are set to be separated by $2h = 3$ cm, as shown on figure 4 2

Particle dynamics

Particles are loaded from the plasma boundary, at $y = 10$ cm, with random initial x position between $x = -3$ and $x = 3$ cm and random velocities selected according to a Maxwellian distribution

$$f(v) = n\sqrt{\frac{2}{\pi}}\left(\frac{m}{\kappa T}\right)^{3/2} v^2 \exp\left\{-\frac{1}{2}\frac{mv^2}{\kappa T}\right\} \tag{4 12}$$

The Maxwellian distributed velocities are calculated with a uniform random number generator (number between 0 and 1) by means of a transformation The mam procedure for this transformation is outlined in appendix B The probability for an electron of having a velocity in the interval [0,v] is given by

$$F(v) = \text{erf}\left(v\sqrt{\frac{m}{2\kappa T}}\right) - \sqrt{\frac{2m}{\kappa T\pi}} \exp\left\{-\frac{1}{2}\frac{mv^2}{\kappa T}\right\} \tag{4 13}$$

This can be related numerically to a uniform density of probability function $p(x) = 1$, probability function $P(x) = x$, x in [0,1] given by a random number generator [66], by the inverse function

$$x = F(v) \rightarrow v = F^{-1}(x) \tag{4 14}$$

which is solved numerically, the results presented here correspond to a 3 eV electron energy distribution temperature

The particles trajectories are integrated using a Runge-Kutta algorithm of fourth order [66] The equations of motion as a set of first order ordinary

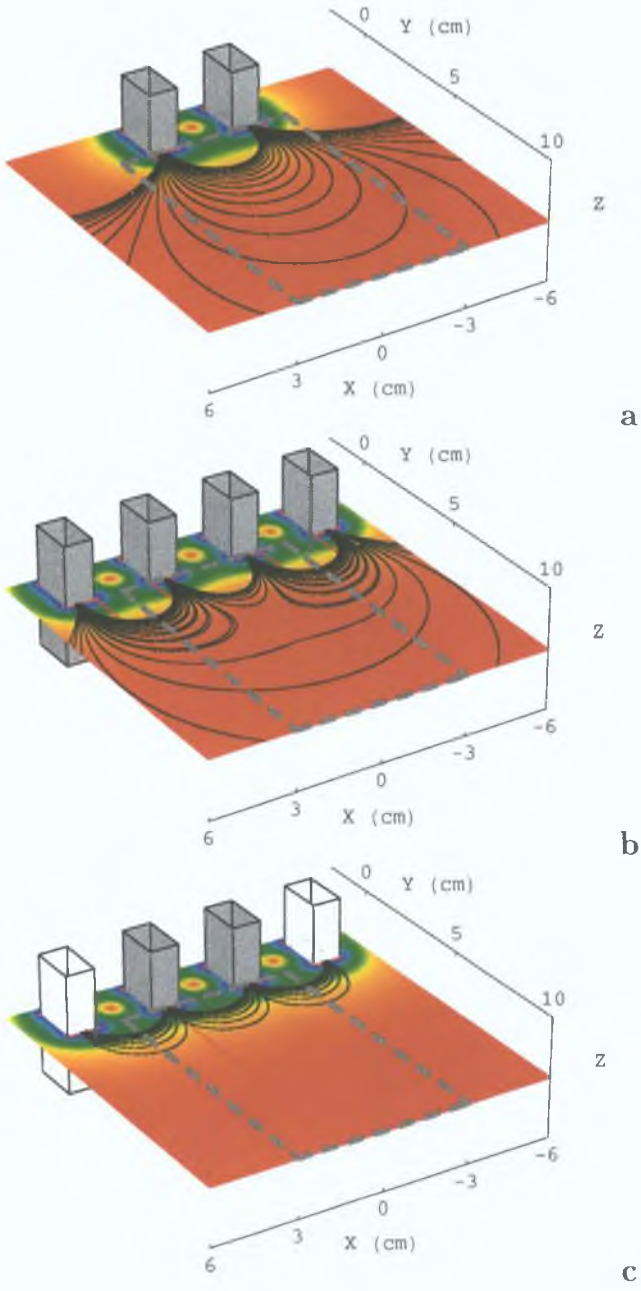

Figure 4.2: *3-dimensional plots of the magnetic cusps. Magnetic bars are infinitely long in the Z axis. Magnetic field of the bars is orientated on the Y axis. Magnetic field lines for:* ***(a)*** *only two magnetic bars (asymmetric cusps; bar polarity at $y = 0$ N-S),* ***(b)*** *only four bars (asymmetric cusps; polarity N-S-N-S, notice the field line connection from extreme opposite bars) and,* ***(c)*** *infinite number of magnetic bars (simplified by calculating the magnetic field of only the two closest bars; symmetric cusps; polarity N-S-N-S). The spatial region of the X-Y plane considered on the single particle model is indicated by dashed grey contour.*

differential equations

$$\frac{\mathrm{d}x}{\mathrm{d}t} = v_x \tag{4.15}$$
$$\frac{\mathrm{d}y}{\mathrm{d}t} = v_y \tag{4.16}$$
$$\frac{\mathrm{d}z}{\mathrm{d}t} = v_z \tag{4.17}$$
$$\frac{\mathrm{d}v_x}{\mathrm{d}t} = -\frac{q}{m} B_{y\mathrm{total}}(x_1, x_2) v_z \tag{4.18}$$
$$\frac{\mathrm{d}v_y}{\mathrm{d}t} = \frac{q}{m} B_{x\mathrm{total}}(x_1, x_2) v_z \tag{4.19}$$
$$\frac{\mathrm{d}v_z}{\mathrm{d}t} = \frac{q}{m} \left\{ B_{y\mathrm{total}}(x_1, x_2) v_x - B_{x\mathrm{total}}(x_1, x_2) v_y \right\} \tag{4.20}$$

where the only force considered is the Lorentz force; this model is non-self consistent and neglects collective behaviour or electric field. Note that since the magnetic field is independent of z, it is not important to update the particle position on the Z axis to determine the magnetic field force. Depending on the strength of the magnetic field the time step is selected in the range $\Delta t = 10^{-11} - 10^{-10}$ s. The cyclotron frequency at the maximum magnetic field (at the magnetic bar face; 600 Gauss) is 1.98 GHz, which is greater than the collision frequency for pressure 0.1-100 mTorr. The time step is selected such that the orbital particle trajectories around the magnetic field lines can be resolved.

Boundaries

The analysis of the particle trajectories is limited to the plane X-Y between $x = -3$ and $x = 3$ cm and $y = 0$ and $y = 10$ cm; this region is shown in figure 4.2. At $y = 10$ cm the magnetic field intensity is less than approximately 2 Gauss ($f_{\mathrm{cyclotron}} \simeq 5.6$ MHz); comparable to the earth magnetic field (0.5 Gauss, $f_{\mathrm{cyclotron}} \simeq 1.4$ MHz). Three different types of boundary conditions are defined. If particle position $y < 0$ the particle is counted as

collected by the magnetic boundary If $y > 10$ cm the particle is counted as returned to the plasma bulk If $x < -3$ or $x > 3$ cm the particle is bounced back with reversed v_x velocity Injected particles trajectories are tracked for a maximum period of 1 μs If the particles have not been returned to the plasma bulk or collected by the magnetic boundary their last position (x, y) is noted

Neutral pressure

The neutral pressure effect on the particle trajectories is included in the model by considering electron-neutral elastic collisions, collision cross sections for molecular hydrogen ($e + H_2 \rightarrow e + H_2$) form reference [67] ($\sigma$) Given the electron energy when a particle is loaded, the collision mean period (τ) is calculated

$$\tau = \frac{1}{n_{H_2}\sigma(v)v} \tag{4 21}$$

The probability of a collision in an interval t

$$T(t) = 1 - e^{-t/\tau} \tag{4 22}$$

Which can be analytically transformed to a probability function $P(x) = x$ (x [0,1]) The time between collisions is randomly selected using the explicit formula

$$x = T(t) \rightarrow t = T^{-1}(x) = -\tau \log(1 - x) \tag{4 23}$$

In this case is is possible to transform the probability of a collision in a time into a uniform distribution The motion equations determine the particle trajectory in-between collisions When the particle experience an elastic collision is velocity is randomised where every direction has the same probability A particle is said to be magnetised if its cyclotron frequency is greater

than its collision frequency ($f_{\text{cyclotron}} > \nu_{\text{elastic}}$)

$$f_{\text{cyclotron}} = \frac{q|\mathbf{B}|}{2\pi m_e} \tag{4 24}$$

$$\nu_{\text{elastic}} = n_{H_2}\sigma(v)v \tag{4 25}$$

The cyclotron frequency depends on the intensity of the magnetic field while the collision frequency depends on the particle velocity (energy) and the neutral gas pressure

Figure 4 3 shows a basic flow chart of the single particle model presented

4.1.3 Summary

The single trajectory model presented here is developed to study the confinement effect of a magnetised boundary onto single particles Neutral pressure effects on the magnetised particles are also considered in the study The model is not self-consistent, furthermore it neglects the electric field on the particle trajectory calculation In spite of the last limitation expected basic trends on the pressure effect are reproduced with the model A full 2D kinetic (PIC) or hybrid model would be necessary for a self-consistent simulation Though such approach would be computationally more expensive than the present model

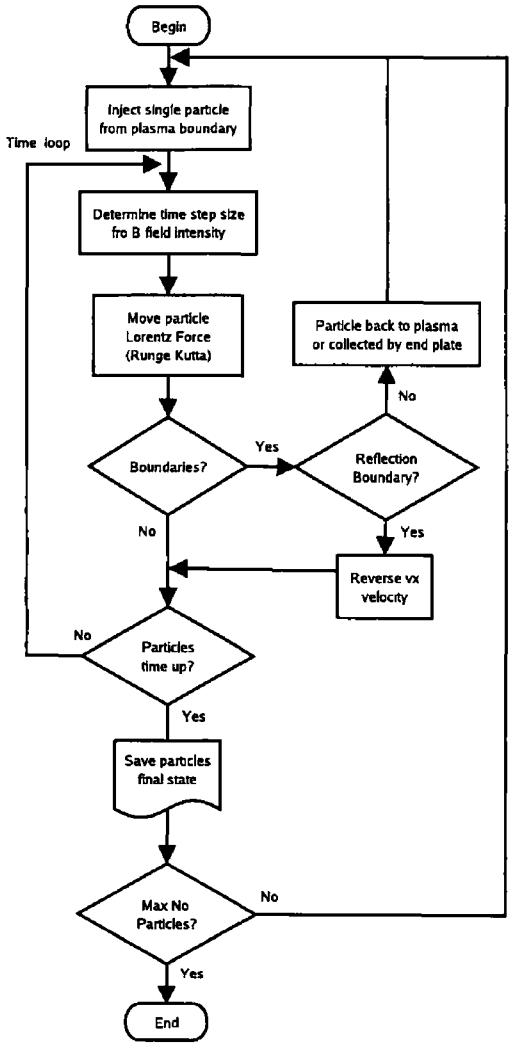

Figure 4 3 *Basic flow chart of the single particle model*

4.2 One dimensional PIC-MCC model of a plasma in the vicinity of a cylindrical Langmuir probe

4 2.1 Introduction

The work developed in this section is inspired on one of the most basic, complicated to analyse though, diagnostics for low temperature plasmas the Langmuir probe An electrostatic or Langmuir probe is basically a small electrode in contact with a plasma Typically the probe is biased with respect to ground (vacuum chamber) and the current drawn form the plasma is measured The current and bias voltage record is called the characteristic I-V trace The main problem is to determine plasma parameters form the characteristic such as electron and ion saturation current, plasma and floating potential and electron temperature

Since the introduction of the Langmuir probe (1924) several basic theories have been developed to analyse the probe data, each limited by its own approximations Different theories apply to different particular situations Although the problem is clear enough we still lack a general probe theory, even for a single ion species plasma Section 3 1 presents an introduction to some of the electrostatic basic theories and techniques

The main theories used to analyse probe data on low temperature plasmas are

- Orbital Motion Limited (OML) The attracted species drifts from infinite without collisions, Maxwellian velocity distributions are assumed
- Allen-Boyd-Reynolds (ABR) The attracted species has no thermal mo-

tion and falls radially into the probe. Zero collection of the repelled species is assumed. This theory is valid for large voltages (ion saturation).

- Bernstein-Rabinowitz (BR). The attracted species distribution is monoenergetic and isotropic. Zero collection of the repelled species is assumed. This theory is valid for large voltages (ion saturation).

- Bernstein-Rabinowitz-Laframboise (BRL). Velocity distribution functions are assumed to be Maxwellian. The spherical and cylindrical probes are analysed potential. Potential barriers are so that all type of trapped orbits are neglected on the analysis. This work represents an extension of the OML theory.

Typical problems when analysing probe data are

- Separation of electron and ion currents drawn by the probe. This is non trivial and is where probe theories are most needed to model the ion/electron current.

- Most probe theories rely on the assumption that the electron energy distribution function (EEDF) can be approximated as Maxwellian. This is not always true as Godyak [32] and others [34, 68] have demonstrated experimentally. This leads to erroneous electron temperatures for most of the standard probe theories.

- Ion collisions in the sheath can affect the ion current drawn by the probe. Sternovsky et al [39, 40, 69] have shown that OML can fail under conditions where it would be typically used for probe data analysis.

- Many plasma sources use radio-frequency to excite and sustain a discharge. The plasma potential would typically present RF modulation.

In certain cases such as capacitive discharges this oscillations can be as large as several times the electron temperature. Data analysis of uncompensated probes would overestimate the electron temperature [59].

- Determination of the plasma potential (V_P) is another non-trivial problem in RF discharges –due to plasma potential oscillations– and plasmas in general due to probe difficulties to collect low energy electrons.

Solutions to many of this problems can be approached with various probe techniques and or careful construction design. For example non-Maxwellian EEDF can be estimated from the second derivative of the electron current form the probe I-V characteristic [29]; see section 3.1.4. The RF plasma potential oscillations can be corrected with active or passive compensation built on the probe; see section 3.1.5. Though, other problems remain.

In this section we present a one dimensional particle-in-cell (PIC-MCC) model with Monte-Carlo collisions of a plasma in the vicinity of a cylindrical Langmuir probe. Although one of the most used theories (Laframboise [37]) was developed for spherical and cylindrical probes we developed our PIC model for a cylindrical geometry as it is the most used. Our model is inspired on the lack of a general theory for electrostatic probes required to deal with analysis problems. A full kinetic model (PIC) can provide information about plasma parameters and give a better picture of the plasma dynamics. Also in this particular case the plasma interaction with a cylindrical probe can be studied by means of reproducing current-voltage characteristics (I-V trace).

Most of the probe theories assumptions –such as radial fall into the probe for attracted ions (to deal with collisions), collision-less dynamics or Maxwellian distribution – can be dropped on our kinetic model. Finally on the model we present here we only assume –like most probe theories– cylindrical symmetry around the probe and that the probe is long enough to

neglect probe end effects With this assumptions we can reduce the model to a one dimensional problem

4.2 2 The model

General remarks

A particle in cell is a purely kinetic model where electrons and ions are treated as individual particles moving according to a self-consistent electric field while eventually experiencing particle-neutral collisions (charged particle collisions with background neutrals)

Since a real plasma may contain millions of particles per species even in small volumes it is practically impossible to keep track of such large number of particles with actual computers It is common use to represent many real particles of one species (10^2-10^4) with one computational particle called *superparticle* [70] The superparticle factor (S_k) is the number or real particles per superparticle Every superparticle velocity and position is susceptible to change due to the self-consistent electric field or due to particle-neutral collision It is understood that all the real particles represented by a superparticle change their phase space position accordingly Note that although a superparticle represents many real particles the charge to mass ratio of a superparticle is the same to that of real particles The motion equations of a superpaticle and a real particle are the same so the fact that a superparticle represent many real particles does not affect its motion

The model developed here is *electrostatic* which means that no electromagnetic effects –such as radiation (electric and magnetic field propagation)– are considered on the calculation of the self-consistent field The field is cal-

culated solving the Poisson equation.

$$\nabla^2\phi = -\frac{\rho}{\varepsilon_o} \tag{4.26}$$

The Poisson equation is numerically integrated using boundary conditions and the charge distribution function (ρ) determined from the position of all superparticles at a given time. The electric field is calculated from the spatial potential.

$$\mathbf{E} = -\nabla\phi \tag{4.27}$$

Particles position and velocity are updated with a *leap-frog* scheme using the calculated electric field. Particle motion equations.

$$\frac{\mathrm{d}\mathbf{v}}{\mathrm{d}t} = \frac{q}{m}\mathbf{E} \tag{4.28}$$

$$\frac{\mathrm{d}\mathbf{r}}{\mathrm{d}t} = \mathbf{v} \tag{4.29}$$

If particle-neutral collisions are accounted a number of superparticles will experience a collision which –depending on the type of collision– could change the velocity ($\mathbf{v}$) and/or the kinetic energy ($mv^2/2$) of the superparticle. Boundaries may also absorb or emit superparticles. Once new positions and velocities are calculated the space potential and electric field are updated and so on. This steps define the basic loop in an electrostatic PIC model. Other in-loop steps could be diagnostics and consistency controls to check for non-physical results.

The field and motion equations are numerically solved, this requires time and space discretization. The field equation is solved at a number of finite positions in space, this defines a grid. On the grid cell boundaries the field is known and the field every where else is calculated by interpolation. The simulation loop has also a time step associated. This time step cannot be larger than the time period for any particular phenomena to be studied with

the PIC model. Restrictions such as to keep a small percentage of particles colliding every time step or to prevent a typical particle from flying past more than one space grid cell in one time step apply.

Probe-PIC model

The PIC model presented here has been developed to study plasma interaction with cylindrical probes. Assumptions are that the probe is long enough ($l \gg r_o$) with respect to its radius (r_o) and that the probe is a perfect cylinder and the plasma parameters are only dependent of the distance to the probe (r). This way the model is reduced to a one-dimensional problem where the radial distance to the probe is the only spatial parameter needed to study the particle dynamics around the probe. All directions pointing from the probe axis are equivalent.

A particle moving around a cylindrical probe where the field is purely radial is an example where the particle motion is restricted a to a plane perpendicular to the probe axis. This is essentially a central force field problem [71]. Unlike planar geometries here we have to be careful that although the central force is radial the particle motion is determined also by its angular velocity. This comes from the angular momentum conservation.

Figure 4.4 shows a diagram of the cylindrical system. The superparticles represent charged cylindrical shells infinitely long. The system is bounded by the probe surface at the inner radius and an external radius where the plasma parameters are those set for the plasma bulk. It is clear that only the superpaticles radial position requires to be updated together with the radial, angular and parallel velocities. The parallel velocity is only important in collisional situations where the three-dimensional output velocity after a collision depends on all three components. In a collision-less case only the

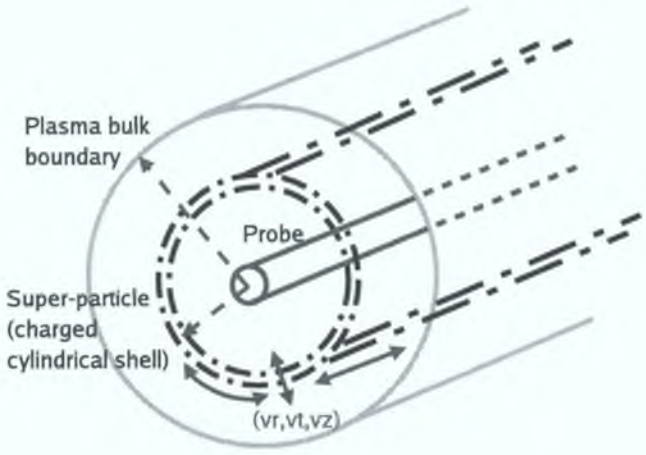

Figure 4.4: *Diagram of the Probe-PIC system. Superparticles represent charged cylindrical cells.*

radial and angular velocities are required.

Following the symmetry assumptions the potential (4.26) and field (4.27) equations are reduced.

$$\frac{1}{r}\frac{\mathrm{d}}{\mathrm{d}r}\left(r\frac{\mathrm{d}\phi}{\mathrm{d}r}\right) = -\frac{\rho(r)}{\varepsilon_o} \tag{4.30a}$$

$$E_r = -\frac{\mathrm{d}\phi}{\mathrm{d}r} \tag{4.30b}$$

And the equations of motion.

$$\frac{\mathrm{d}v_r}{\mathrm{d}t} = \frac{q}{m}E_r + \frac{v_\theta^2}{r} \tag{4.31a}$$

$$\frac{\mathrm{d}r}{\mathrm{d}t} = v_r \tag{4.31b}$$

$$L = mrv_\theta \tag{4.31c}$$

Where L is the angular momentum. The equations of motion can be derived using classical mechanics calculus of variations [71, 72]. This principles are powerful enough to immediately derive some constants of motion such as the angular momentum.

The model is bounded on one side by the probe surface at the probe radius (r_o) and on the other side by a quasi-neutral steady plasma at the plasma

radius (r_P) The plasma radius is set large enough so that quasi-neutrality and a negligible electric field can be expected The model simulates a plasma region around a cylindrical probe This plasma develops from the plasma injection into the study region The injection point is at the plasma radius[1] The plasma parameters –such as plasma density, electron temperature or energy distribution functions and plasma potential– surrounding the probe are driven from the plasma injected at the plasma radius The time and space evolution of the injected plasma with very well defined parameters up to the probe particle collection count is the essence of the model attempting to connect the unperturbed plasma with the measured probe characteristic

The boundary conditions are the probe bias (V_B) at the probe surface (r_o) and the plasma potential (V_P) at the plasma radius (r_P) An extra boundary condition at the plasma radius is imposed It is that at the plasma radius there should be none or little electric fields This is controlled on the model by adding a drift velocity to each of the loading species according to any arising fields at the plasma radius Particles are only loaded at the plasma radius although the model can be extended to study probe emission Finally any particle is absorbed/collected at the boundaries If collected at the probe radius then it is counted for the species current density Secondary electron emission from ion bombardment on the probe surface is not considered in the model

From symmetry assumptions, superparticles represent axis-symmetric charged cylinders All superparticles axis and the probe axis are centred at $r = 0$ As a superparticle approaches the probe surface radius (r_o) its density grows due to the geometrical factor The number of particles required to represent

[1]This is not related to the plasma size which typically measures the length in general of a confined discharge

a certain charge density is a function of the radius (r) and grows with it. The superpaticles have three velocity components (v_r,v_θ,v_z) and one constant of motion, the angular velocity (L). The radial and angular velocity evolve as the particle travels around the probe while the parallel velocity is only considered when particle-neutral collisions occur.

The radial dimension is discretized using equal spacing. In a cylindrical geometry this results in that the volume represented by each cell is a function of the radius. This results also in that a number of particles in one particular cell does not represent the same density in another cell. Discretization is required to solve numerically the field equations. The radial length is divided in N equally spaced cells of size Δr. Cell boundaries are called r_i where i runs form 0 to N. The probe surface radius ($r_0 = r_o$) and the plasma radius ($r_N = r_P$) define the boundaries of the discretized region.

After discretization the Poisson equation (4.30a) reads.

$$\phi_{i-1}\left\{r_i - \frac{\Delta r}{2}\right\} - 2\phi_i\{r_i\} + \phi_{i+1}\left\{r_i + \frac{\Delta r}{2}\right\} = -\frac{\rho_i r_i (\Delta r)^2}{\varepsilon_o} \tag{4.32}$$

Where ϕ_i is the space potential at positions r_i (i from 0 to N) and ρ_i is the charge density calculated at cell boundaries r_i (i from 1 to $N-1$). The space charge density is calculated at the cell boundaries using first order weighting (uniformly charged cloud) [70]. The charge of a superparticle j of species k at position $r_{j,k}$ bounded by r_{i-1} and r_i is assigned to the cell boundaries as follow

$$Q_{i-1,j,k} = q_k\left(\frac{r_i - r_{j,k}}{\Delta r}\right) \tag{4.33a}$$

$$Q_{i,j,k} = q_k\left(\frac{r_{j,k} - r_{i-1}}{\Delta r}\right) \tag{4.33b}$$

where q_k is the electric charge of the superparticle of species k. The contribution of the superparticle to the charge density at the cell boundaries

is

$$\rho_{i-1,j,k} = \frac{Q_{i-1,j,k}}{2\pi r_{i-1}\Delta r l} \tag{4 34a}$$

$$\rho_{i,j,k} = \frac{Q_{i,j,k}}{2\pi r_i \Delta r l} \tag{4 34b}$$

where l is the length of the probe Notice that for a given charged superparticle the contributed charge density is inversely proportional to the radial distance of the cell boundary to the probe axis Finally the charge density at cell boundaries (ρ_i) is the cumulative contribution of the charge density of every charged particle from every species to the boundaries of the cell where they are located

Equation (4 32) represent a set of $N-1$ equations with $N-1$ unknowns Extreme boundary voltages –the bias voltage on the probe ($\phi_0 = V_B$) and the plasma potential ($\phi_N = V_P$)– are known This set of equation can be written as a matrix equation

$$\begin{pmatrix} -2r_1 & r_1+\frac{\Delta r}{2} & 0 & 0 & 0 & 0 & 0 \\ r_2-\frac{\Delta r}{2} & -2r_2 & r_2+\frac{\Delta r}{2} & 0 & 0 & 0 & 0 \\ 0 & r_3-\frac{\Delta r}{2} & -2r_3 & r_3+\frac{\Delta r}{2} & 0 & 0 & 0 \\ & & & & & & \\ 0 & & 0 & 0 & 0 & r_{N-2}-\frac{\Delta r}{2} & -2r_{N-2} \quad r_{N-2}+\frac{\Delta r}{2} \\ 0 & & 0 & 0 & 0 & 0 & r_{N-1}-\frac{\Delta r}{2} \quad -2r_{N-1} \end{pmatrix}$$

$$\times \begin{pmatrix} \phi_1 \\ \phi_2 \\ \phi_3 \\ \\ \phi_{N-2} \\ \phi_{N-1} \end{pmatrix} = -\frac{(\Delta r)^2}{\varepsilon_o} \begin{pmatrix} \rho_1 r_1 - \phi_o\{r_1+\frac{\Delta r}{2}\}\frac{\varepsilon_o}{(\Delta r)^2} \\ \rho_2 r_2 \\ \rho_3 r_3 \\ \\ \rho_{N-2} r_{N-2} \\ \rho_{N-1} r_{N-1} - \phi_N\{r_{N-1}+\frac{\Delta r}{2}\}\frac{\varepsilon_o}{(\Delta r)^2} \end{pmatrix} \tag{4 35}$$

This set of equations is solved in general calculating the inverse of the first left hand side matrix and multiplying the equation by the inverse matrix. In this particular case we notice it is a tridiagonal matrix problem and we use a custom algorithm (Numerical Recipes in C [73]) to calculate the internal space potential unknowns.

The electric field is calculated at the cell boundaries (r_i) from the discrete set of space potential values (ϕ_i); from equation (4.30b).

$$E_{r,i} = \frac{\phi_{i-1} - \phi_{i+1}}{2\Delta r} \tag{4.36}$$

Linear interpolation is used to evaluate the electric field at any radius (r).

The radial position (r) and velocity (v_r) and angular velocity (v_θ) of each particle are updated considering the angular momentum (L) conservation. The parallel velocity (v_z) is tracked as it is updated after a collision and it can affect the particle motion with the energy stored in it. From (4.31) the discretized particle motion equations are

$$v_{r,t+\Delta t} = v_{r,t} + \frac{q}{m} E_r \Delta t + \frac{v_{\theta,t}^2}{r_t} \Delta t \tag{4.37a}$$

$$r_{t+\Delta t} = r_t + v_{r,t+\Delta t} \Delta t \tag{4.37b}$$

$$v_{\theta,t+\Delta t} = \frac{L}{m\, r_{t+\Delta t}} \tag{4.37c}$$

Particles are loaded at the plasma radius with velocities v_r, v_θ and v_z. The angular and parallel velocity of a particle are randomly selected with an overall Maxwellian distribution using a Box-Muller transformation [74, 75]. The radial velocity is randomly selected so that it is negative (incoming particle) and with an overall $v_r \times$ Maxwelliam distribution.

$$f(v_r) = \frac{1}{\sqrt{2\pi}} v_r \exp\left\{-\frac{v_r^2}{2\sigma^2}\right\} \tag{4.38}$$

where $v_r \in [0, \infty\rangle$ and if $\sigma = 1$ then for a given distribution temperature the random radial velocity is assigned $v_r = -v_{r,\sigma=1} v_{\text{thermal}}$. This distribu-

tion is used to ensure a Maxwellian distribution on the radial velocity space in the simulation region This particular distribution prevents large injection of slow particles which would spend more time in the simulated region, creating a distortion of the expected distribution Plasma species densities (n_k) and temperatures (T_k) are given at the start of the simulation define the Maxwellian distributions Although the model has been used assuming Maxwellian distributions for all the plasma loaded species, other distributions –such as Druyvesteyn– can be implemented to study their effect on the probe collection and the PIC model

The number of superparticles to be injected every time step (Δt) is determined by the random thermal fluxes of every species and the field boundary condition which may introduce an extra drift velocity The random thermal flux of species k

$$\Gamma_k = \frac{1}{4} n_k \langle v_k \rangle \tag{4 39}$$

where the average velocity modulus

$$\langle v_k \rangle = \sqrt{\frac{8 q_k T_k}{\pi m_k}} \tag{4 40}$$

The number of new superparticles every time step

$$\mathcal{N}_k = (\Gamma_k + n_k v_{\mathrm{drift},k}) \frac{\mathcal{A} \Delta t}{S_k} \tag{4 41}$$

where $\mathcal{A} = 2\pi r_P l$ is the area at the plasma radius (r_P), l is the probe length and S_k the superparticle factor for species k The drift velocity is calculated from the change of space potential on the last two cells

$$v_{\mathrm{drift},k} = \mathrm{sign}(q_k \Delta\phi) \sqrt{\left| \frac{2 q_k \Delta\phi}{m_k} \right|} \tag{4 42}$$

where $\Delta\phi = \phi_N - \phi_{N-2}$ This drift velocity controls the flux of particles –in particular the lightest– to prevent the development of large electric fields on the last two cells before the plasma radius

Particle neutral collisions are handled by calculating the collision probability of each particle every time step The probability of a particle collision in a lapse of time t

$$P_{collision}(t) = 1 - \exp\{-\nu(v)t\} \tag{4 43}$$

Where ν is the collision frequency, function of the particles velocity modulus (v)

$$\nu(v) = n_n \sigma(v) v \tag{4 44}$$

Where n_n is the neutral gas density and $\sigma(v)$ is the collision cross section If the time step is restricted to $\Delta t \ll \nu(v)$ for the fastest species (typically the electrons) the probability of a collision in the time step Δt is approximated

$$P_{collision}(\Delta t) \simeq \nu(v)\Delta t \tag{4 45}$$

The model accounts for elastic and inelastic particle neutral collisions For each collision a cross section set $(\sigma(v))$ is required to calculate the total collision probability and type of collision A maximum collision cross section (σ_{max}) is calculated for every species within a range of possible energies for the species Using the maximum cross section the probability of a collision for a given particle every time step –a function of the modulus of the particle velocity– approximates

$$P_{collision}(\Delta t) \simeq n_n \sigma_{max} v \Delta t \tag{4 46}$$

A random number $(0 \leq n_{r1} \leq 1)$ is generated and compared to this probability If it is smaller or equal to $P_{collision}$ then the particle undergo a collision The collision type is determined with another random number $(0 \leq n_{r2} \leq 1)$

and restricted by the threshold energy of each collision type

$$n_{r2} \leq \frac{\sum_{i=j}^{n} \sigma_i(v)}{\sum_{i=1}^{n} \sigma_i(v)} \quad \text{and} \quad E_{j,threshold} \leq \frac{1}{2} m v^2 \tag{4 47}$$

Conditions (4 47) are tested for $j = \{n, \quad , 1\}$ The cross sections (σ_i) are ordered from inelastic collisions ($i = n$) to elastic collision ($i = 1$) Elastic collisions have no energy threshold therefore if no other type of collision condition is satisfied the particle undergoes an elastic collision

The plasma gas modelled in this thesis is Argon Particle-neutral cross sections for this gas were taken from collision cross section data found in [76–78], see Miles Turner EN electrostatic PIC model

In order to have a stable simulation we have to impose certain limits to the time step and cell size The cell size (Δr) is restricted by the Debye length (λ_D)

$$\frac{\Delta r}{\lambda_D} \leq 0\,5 \tag{4 48}$$

And the time step (Δt) is restricted by the collision frequency (calculated for the thermal velocity) of the fastest species,

$$n_n \sigma_{max} v_{thermal} \Delta t \leq 0\,01 \tag{4 49}$$

the time of flight through a cell (calculated for the thermal velocity) of the fastest species

$$\frac{v_{thermal}}{\Delta r} \Delta t \leq 0\,25 \tag{4 50}$$

and the plasma frequency (ω_p)

$$\omega_p \Delta t \leq 0\,2 \tag{4 51}$$

Take Δt as the minimum of the three. The thermal velocity is set at stat-up of the model from the distribution temperature of the injected particles at the plasma boundary.

The main input parameters required to run a simulation with the *Probe*-PIC model are the probe radius (r_o), the plasma radius (r_P), the probe length (l), the number of cells (N),the probe bias voltage (V_B), the plasma density n_o, the species temperature (T_k) and the background neutral gas pressure (P_o). The plasma potential is set to zero ($V_P = 0$). Therefore the probe bias is already referenced to the plasma potential; there is no ground surface defined in the present model.

Main outputs are phase space ($\{r, v_r, v_\theta, v_z\}$) for each species; the charge density (ρ), the space potential (ϕ) and electric field (E_r) profiles ir r and, the energy and radial velocity distribution function (EDF and v_r-DF) of each species at 20 different positions in the radial dimension. It also returns the collected current at the probe per species (I_k) as a function of the time or the probe bias voltage.

In some simulations the introduction of a ficticious negative ion (Ar^-) has been introduced where the cross sections for this particle have been taken as the ones for Ar^+; this was done to model a plasma with a negative ion species.

Figure 4.5 shows a basic flow chart of the particle model presented.

4.2.3 Summary

The kinetic model presented here is an attempt to provide a more complete option to actual probe theories by solving self-consistently the plasma particle motion and field equations. Thus we remove most of theory assumptions except for the geometrical simplification to reduce the problem to a one-

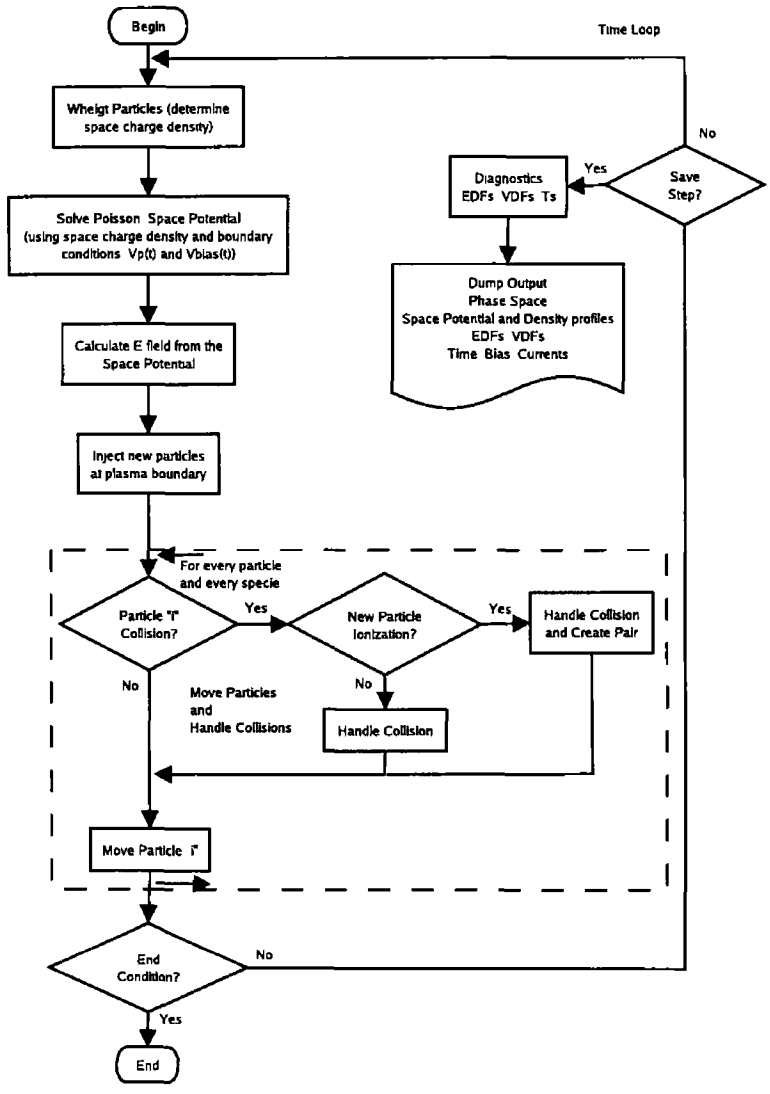

Figure 4 5 *Basic flow chart of the PIC-MCC model*

dimensional model This model simulates a plasma in the vicinities of a cylindrical Langmuir probe

By means of this model we open up the possibilities of exploring different ratios of probe radius to Debye lengths (r_o/λ_D), ion to electron temperature ratios (T_+/T_-) and energy distribution functions per species, collisional effects and types of collisions, radio-frequency (RF) affects on probe characteristics (RF prototype probes), fast probe sweeping, probe current hysteresis, probe collection in multiple ion plasmas (photo-detachment signals), generation of trapped ion orbits, etc

CHAPTER 5

Discussion

We present here experimental and computational results The experimental work has been divided into electrostatic probe measurements and laser absorption measurements The computational results are divided into single particle dynamical behaviour in a magnetised region and self-consistent model of a plasma in the vicinity of an electrostatic probe

5.1 Experimental results

5.1.1 Electrostatic probes and electron energy distribution function measurements

Introduction

A multi line cusp field is arranged in four rows of magnetic bars facing the flange N-S-N-S, (Samarium Cobalt, 5 kG) on the extraction flange (stainless steel) The flange is moderately ferromagnetic and partially shields the magnetic flux into the diffusion chamber ($|\mathbf{B}| < 50$ G) We test the plasma diffusion across the magnetic field at the mid-point between the line-pole faces Figure 5 1 shows a diagram of the ARIS experiment with the permanent magnet bars The axial axis scale is shown as a reference to spatial measurements of the plasma parameters Single and double Langmuir probes are introduced axially through a port at the end-plate and placed at different positions (Z) in the diffusion chamber The magnetic field lines are perpendicular to the probe tip

The Langmuir probes are home made and incorporate radio-frequency filters and a floating reference probe, their design has been explained in detail in section 3 1 (Soberon [79]) We use the AC superimposing technique to measure the electron energy distribution function (EEDF), this technique is reviewed in section 3 1 4 A diagram of the instrument set up for the EEDF measurements is presented in figure 2 2, section 2 6 Using a waveform generator we input a small sinusoidal signal to a power amplifier where the sinusoidal signal is amplified (1 35 V_{pp}) The probe is biased (DC mode) by varying the DC offset of the signal generator A 100 Ω resistor placed between the output of the voltage source and the probe tip gives a voltage

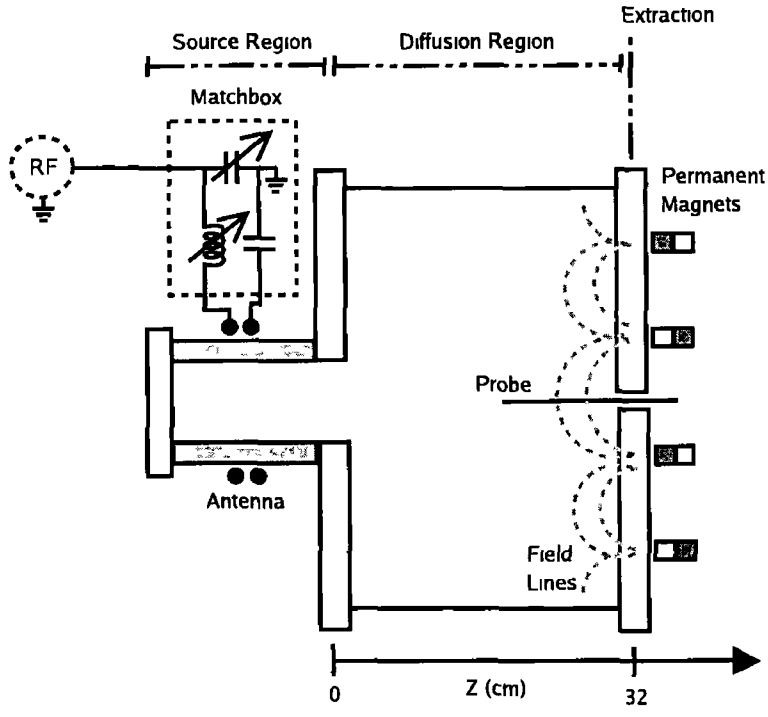

Figure 5 1 *Schematic diagram of ARIS (Applied Radio-frequency Ion Source) with permanent magnet array at the end plate (extraction) Langmuir probes are driven through the extraction flange and scan the EEDF and I-V traces at different positions (Z)*

proportional to probe current, an isolation amplifier (Analog Devices AD202) set for unity gain converts the voltage difference across the resistor to a ground-referenced signal This signal is used as input for a dual phase lock-in-amplifier (Stanford Research Systems SR830) locked on the 2^{nd} harmonic of the original AC bias using the signal generator Sync output into the input reference of the lock-m-amp The lock-in amplifier yields the second harmonic amplitude (R), phase (θ), and Cartesian representations of X (R $\cos\theta$) and Y (R $\sin\theta$) The current signal, the DC probe bias and the DC reference floating probe voltage are recorded by a DAQ card

A LabView routine controls the EEDF measurement keeping the AC bias

constant and varying the DC bias Before data collection at a specified DC bias, the probe tip is cleaned by biasing the probe to +100V for 1-5 seconds depending on the plasma density For each DC bias the second harmonic data (R, θ, X, Y), DC bias, reference potential, and DC current are measured Measuring a single point takes about 10 seconds, so typical runs of 50 points take more than 8 minutes

A few technical details need to be noted Modern lock-in amplifiers are capable of automatically choosing the phase to give the maximum amplitude of second harmonic signal The specific data which should be used, magnitude (R) versus X has not, to our knowledge, been discussed before Selecting a reference phase which compensates for phase shifts caused by the voltage bias amplifier (180 degrees phase shift) and current measurement electronics (isolation amplifier, 45 degrees at 2 kHz) and subtracting 90 degrees due to the sine term in equation (3 25), we find the parameter X yield the best EEDFs According to equation (3 25), if no phase shift associated with the instrumentation or properly compensated, the first harmonic of the AC current is in phase with the AC bias voltage, and the second harmonic of the AC current is +90 degrees (of the fundamental period) out of phase with the AC bias voltage (the second harmonic current is sinusoidal and follows the AC bias voltage with T/4 seconds delay, where T is the period)

Following the technique of Rundle [51], we use the peak of the 2nd derivative, on the X component, as the definition of the plasma potential In our experiment we find significant deviation between the R and X values above the plasma potential, which would give rise to incorrect identification of V_P The difference between R and X arise from the fact that X phase is set, as explained above, in order to be in phase with the second harmonic of the current while R adds up any contribution from the Y component which is

out of phase with the second harmonic of the current R and X are effectively equivalent in the electron retardation region, but may differ in the electron and ion saturation regions of the probe characteristic Figure 5 2 shows the amplitude (R) and X component for a typical trace of the second harmonic of the current versus the probe bias voltage The corresponding phase of the second harmonic of the current as a function of the probe bias is shown in figure 5 3, data is shown with standard deviation over a few hundred samples per bias voltage It can be verified that through the retardation region the second harmonic is in phase (null degrees difference) with the selected phase Also notice the noise on the phase is negligible through the retardation region The noise grows when the probe is biased into ion or electron saturation The range of useful information to estimate the EEDF can be determined from the phase information This information is usually ignored in recent publications, those where dual phase lock-in-amplifiers have been used [47, 48]

Results and Discussion

Single probe measurements (SmartProbe)

A series of EEDF measurements were taken with a *SmartProbe* at different positions in the source and diffusion chamber of the ARIS experiment The probe was introduced through the centre of the diffusion chamber end plate as shown in figure 5 1 The EEDF was obtained by a numerical differentiation algorithm (*SmartSoft*) Figures 5 4 and 5 5 show the EEDF spatial scan in ARIS at two different pressures (1 37 and 3 46 mTorr respectively) and with and without the end plate magnetic multi-cusp The EEDF curve distinguished in grey colour marks the position where the diffusion and the source chambers meet The EEDF measurements where made every centime-

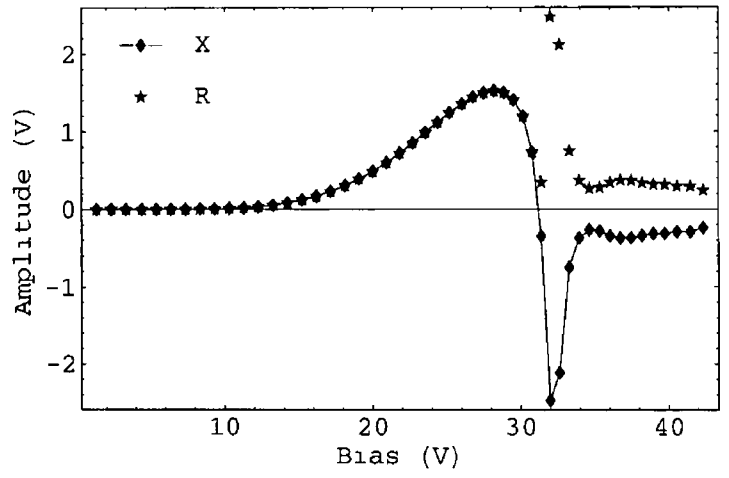

Figure 5 2 *X component and amplitude (R) of the second harmonic of the probe current as a function of DC probe bias The phase is set for the second harmonic of the electron current to be in phase with the reference signal in the lock-in-amplifier, through the retardation region*

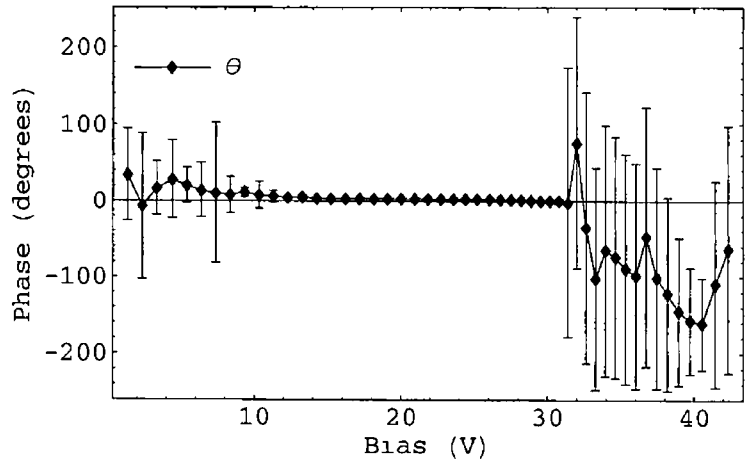

Figure 5 3 *Phase of the second harmonic as a function of the DC probe bias*

tre in the source chamber Similarly in the diffusion chamber but only for the region close to the source, nearby the end plate the measurements were made every 5 cm EEDF measurements in the diffusion chamber close to the end plate where made using the ac superimposing technique and are shown in figure 5 8 Results presented here are limited to low pressure (< 5 mTorr)

It is seen in figures 5 4 and 5 5 that the EEDFs in the source exhibit a large population of low energy electrons, the EEDFs can be taken as structured with two electron energy distributions, similar to a bi-Maxwellian This has been observed by Godyak et al in RF discharges [80, 81], the two component difference is stressed with decreasing pressure and increasing power The high energy population is associated with electrons that gain energy from the RF fields within the skin depth while the low energy population corresponds to electrons with not enough energy to overcome the sheath potential in the source

Single probe current-voltage characteristics were also recorded at same positions, pressure and power The probe traces were analysed by *SmartSoft* using Laframboise theory [37] The floating and plasma potential, electron density and temperature are shown in figures 5 6 and 5 7 as functions of the probe position with and without magnetic multi-cusp on the end plate of the diffusion chamber, for pressures 1 37 and 3 46 mTorr respectively The electron temperature is also calculated by integrating the EEDFs, using equations (3 19) and (3 20) Note that direct analysis of the probe traces implies the EEDF is Maxwellian Therefore basic estimates of the electron temperature may differ from calculated ones after EEDF integration Also the electron temperature calculated form the EEDFs is more properly termed *average electron kinetic energy* [82]

Figures 5 6a and 5 7a show the electron temperature and averaged ki-

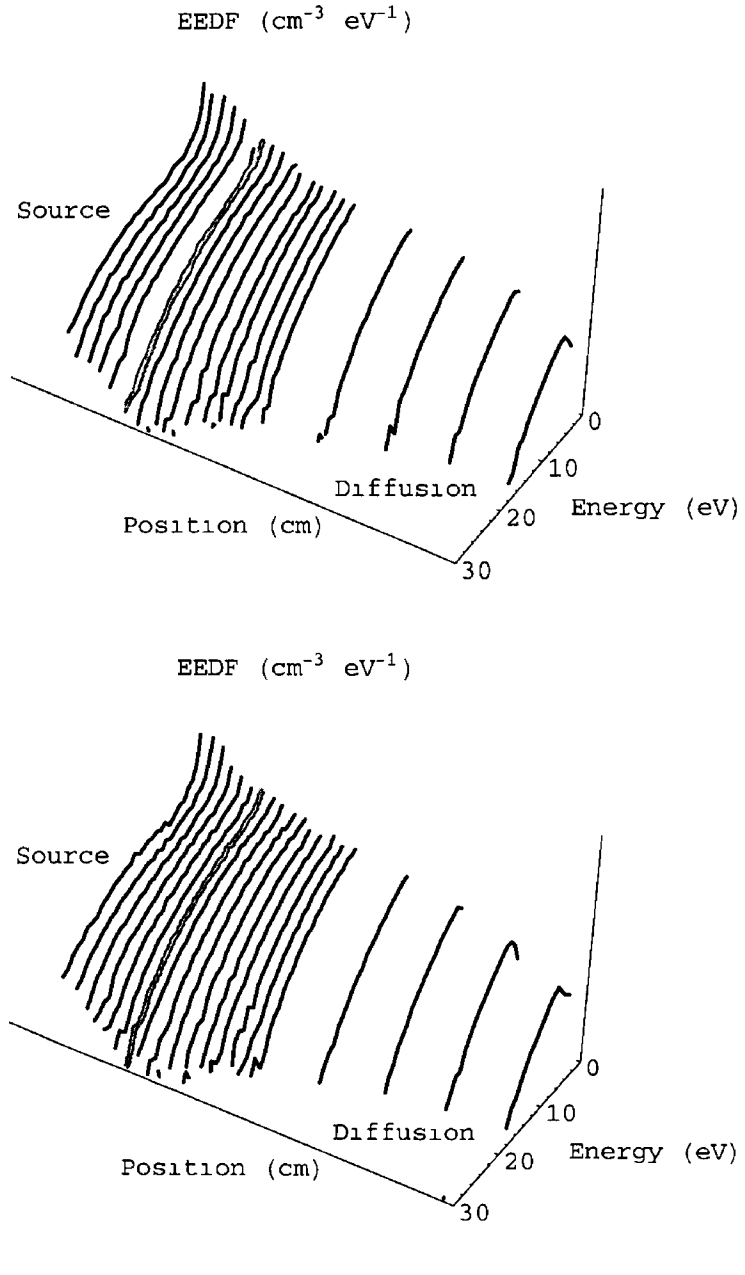

Figure 5 4 *Measured EEDFs with SmartProbe at different position in the source and diffusion chamber in ARIS with (b) and without (a) magnetic field Pressure 1 37 mTorr, Power 1 25 kW*

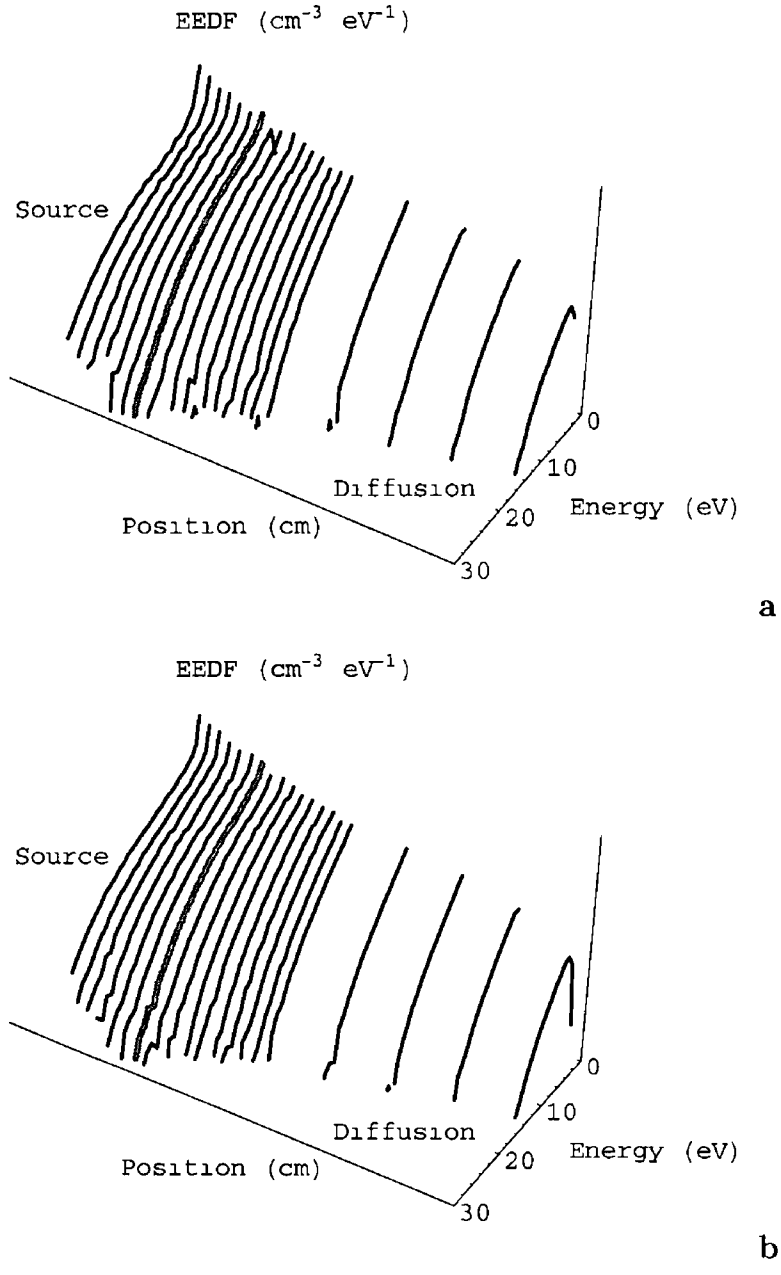

Figure 5 5 *Measured EEDFs with SmartProbe at different position in the source and diffusion chamber in ARIS with (b) and without (a) magnetic field Pressure 3 46 mTorr, Power 1 25 kW and no magnetic fields*

netic energy as a function of probe position Discrepancies of the electron temperature (after the I-V trace) and the averaged electron energy are due to deviations of the EEDFs from Maxwellian distributions

The floating and plasma potential (figures 5 6b and 5 7b) are slightly affected by the presence of the magnetic field, being larger the effect at low pressure This is expected since the magnetic confinement affects more effectively the plasma parameters at low pressures [1]

Figures 5 6c and 5 7c show the electron density as a function of probe position in the diffusion and source chambers The ion density was also calculated but is omitted here because it does not give any further information, the ion density calculated form the ion current usually differs from the electron current by a factors up to 10 [83], although *SmartSoft* compensates this resulting in quite similar densities This is a well know discrepancy on the probe technique [35, 38, 83] which can be explained with ion-neutral collisions in the sheath [39, 40, 69] and/or non isotropy of the ion distribution function Both effects are reproduced with the kinetic model presented in section 4 2, results are presented and discussed in section 5 2 2 From the kinetic model results we conclude that the electron density is a more reliable estimate of the plasma density At the low pressure high plasma density conditions reported in ARIS for the given pressures and powers the effect of ion-neutral collisions is not important, this effect requires the ion mean free path to be small compared to the sheath size and ion orbital motion around the probe (OML [25])

In general the parameters presented in figures 5 6 and 5 7 remain mostly unaffected by the presence of the magnetic multi-cusp on the end plate of the diffusion chamber We can conclude that for the magnetic setup used the source is decoupled from the diffusion chamber We can also conclude from

the large difference in the plasma parameters from the source to the end of the diffusion chamber, that the non-local approximation (used for example in a global model) is not applicable, the electron energy relaxation length is smaller than the diffusion chamber and the power deposition is non uniform in the diffusion chamber

Single (AC superimposing technique) and double probe measurements

A second series of EEDF measurements in the diffusion chamber were performed with a single Langmuir probe using the AC superimposing technique (refer to section 3 1 4) Also double probe current-voltage characteristics were recorded in the extraction region of the diffusion chamber (see figure 5 1) Using the double and single (AC superimposing) techniques we study in detail the magnetised region of the diffusion chamber and compared to unmagnetised case Experimental conditions were 1 5 mTorr Argon, and 1 kW RF power Double probe traces were taken at slightly different conditions, 1 4 mTorr Argon, 1 25 kW RF power

Figure 5 8 shows normalised plots of the electron energy distribution functions (in linear-scale on the left and log-scale on the right) as a function of position in the diffusion chamber Black lines show the EEDF with magnetic filter, and grey lines are without magnetic filter Details of the low energy portion of the EEDF is most clearly seen in figure 5 8a, and details of the high energy portion of the EEDF is most clearly seen in figure 5 8b The first feature to note is that all EEDFs have depleted high energy populations Looking at Z= 6 5 cm (magnetic field free region) the EEDFs agree to within experimental error In contrast, for Z> 24 cm (inside the magnetic cusp region) there are substantial changes in the shape of the EEDF In particular, the magnetic filter results in higher relative population in the low energy portion of the EEDF, and suppressed high energy component These

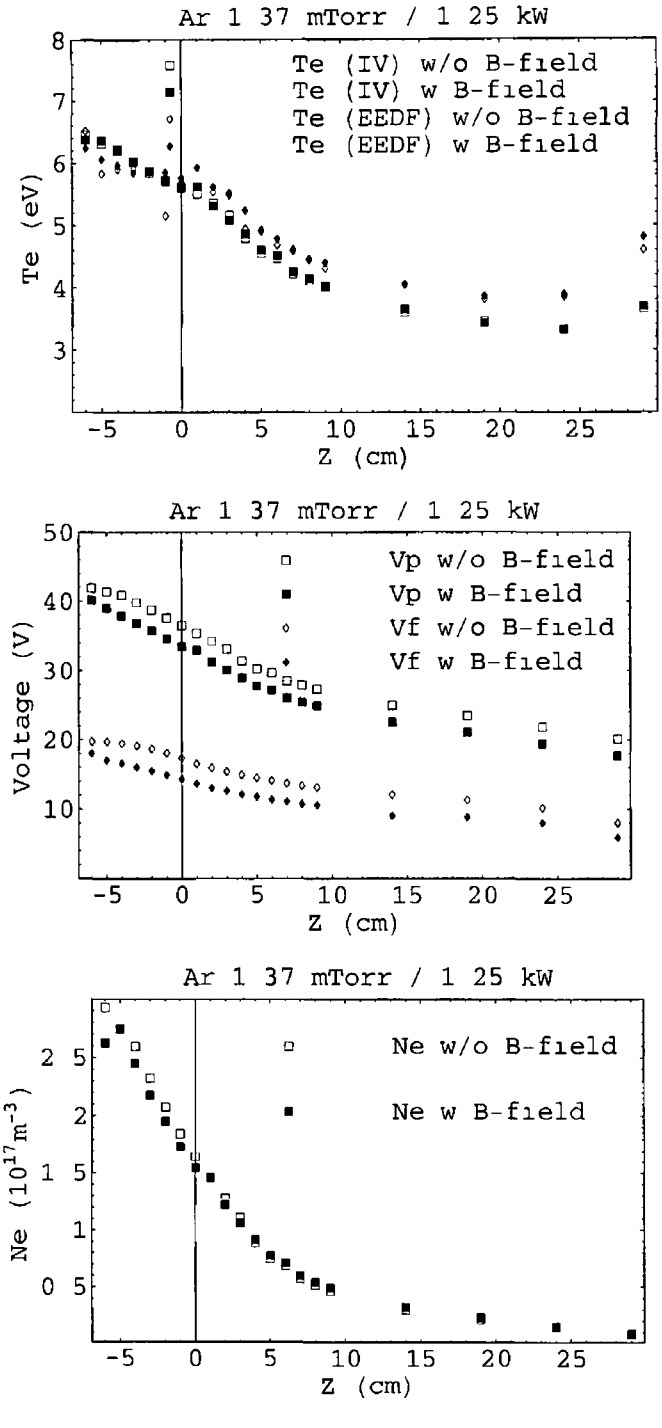

Figure 5 6 *Floating and plasma potential (b), electron density (c) and electron temperature (a) as functions of position in ARIS with and without magnetic field Pressure 1 37 mTorr, Power 1 25 kW*

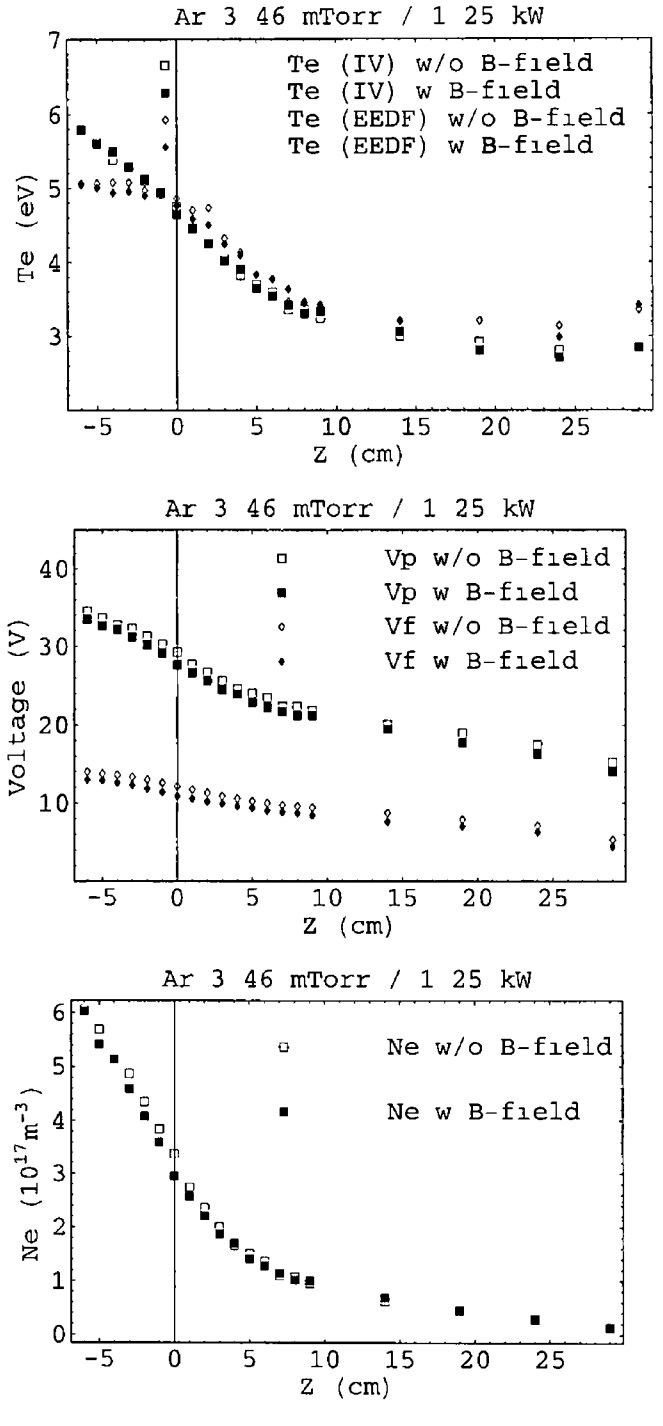

Figure 5 7 *Floating and plasma potential (b), electron density (c) and electron temperature (a) as functions of position in ARIS with and without magnetic field Pressure 3 46 mTorr, Power 1 25 kW*

measurements are consistent with the physical picture of plasma confinement by the magnetic field Close inspection of figure 5 8b at Z= 15 cm, a region in which magnetic filed effects should be unimportant ($B << 1$ Gauss), reveals that the high energy component is higher with the magnetic field than without This is consistent with the physical picture of high energy electrons being reflected by the magnetic filter, results on a model of single particle interaction with a multi-cusp field are presented in section 5 2 1

Figures 5 9, 5 10 and 5 11 show the plasma potential and electron density and temperature as a function of position in the diffusion chamber (the boundary between the source and the diffusion regions is at Z= 0 cm and the end-plate of the diffusion chamber – where ions would be extracted– is located at Z= 32 cm) Parameters are calculated from the integration of the EEDFs fitted with equation (3 34) Figures 5 10 and 5 11 plot probe data versus position in the diffusion chamber, comparing data with and without magnetic field

From figure 5 10 we see that the plasma density with the magnetic field is higher The ratio of density with to without magnetic field increases with proximity to the end flange, and the high magnetic field region We have identified two mechanisms arising from plasma confinement by the magnetic field which would contribute to this effect The first is an effective reduction in the loss area of the diffusion chamber, thus yielding an increase in plasma density The second is the reflection of high energy electrons back into the diffusion chamber, resulting in increased ionisation in the diffusion chamber

Figure 5 11 plots the electron temperature corresponding to the measurements with and without the extraction magnetic field Also a second electron temperature set is shown which was measured with a double probe [41, 55, 79, 84] at slightly different discharge conditions (1 4 mTorr Argon at 1 25 kW

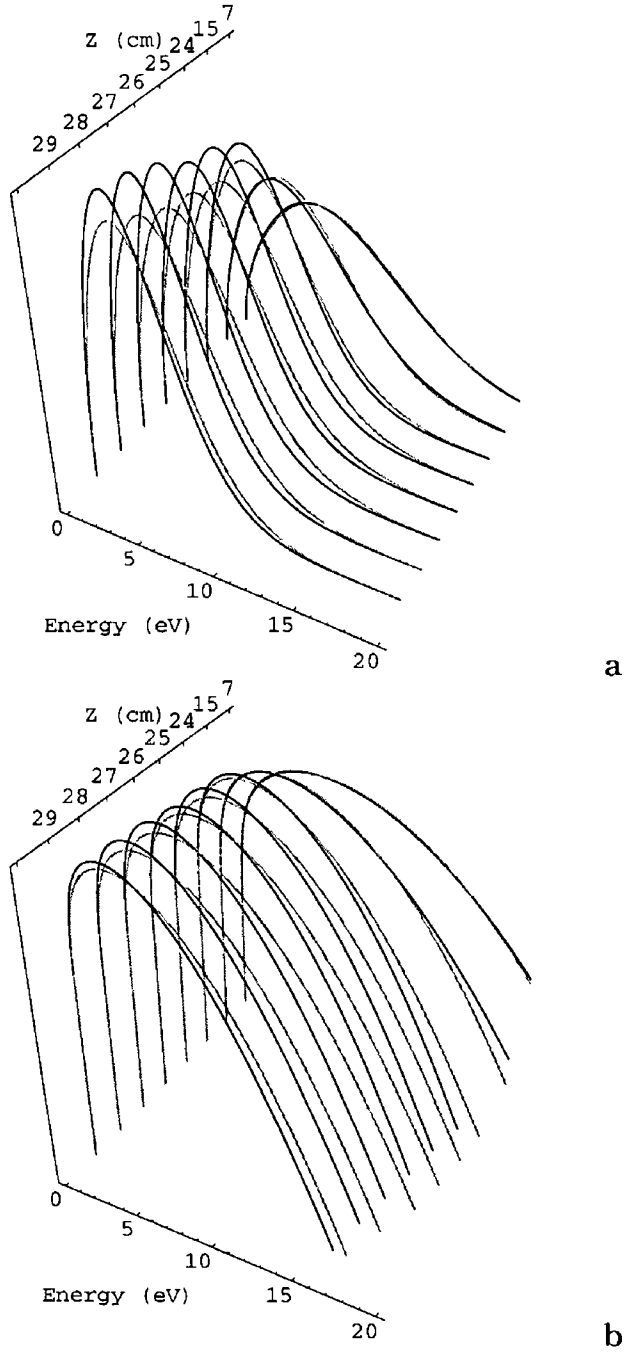

Figure 5 8 *Normalised plots, linear (a) and log (b) scale, of the EEDFs as a function of position in the diffusion chamber Grey data is magnetic field free and black with magnetic filter*

of RF power) With either technique (single probe with AC superposition or double probe) the presence of a magnetic field array reduces the electron temperature in the region where the magnetic field is present The substantial differences between the two techniques are due to the energy range of the EEDF that the two techniques are sensitive to Double probes scan the tail of the electron distribution (from the plasma potential into the ion saturation region) Thus the double probe is sensitive to any changes on the high energy electron population The temperature derived from the single probe is the integration of the full EEDF, resulting in the average kinetic energy Thus, the single probe is more dependent on the low-energy section of the EEDF

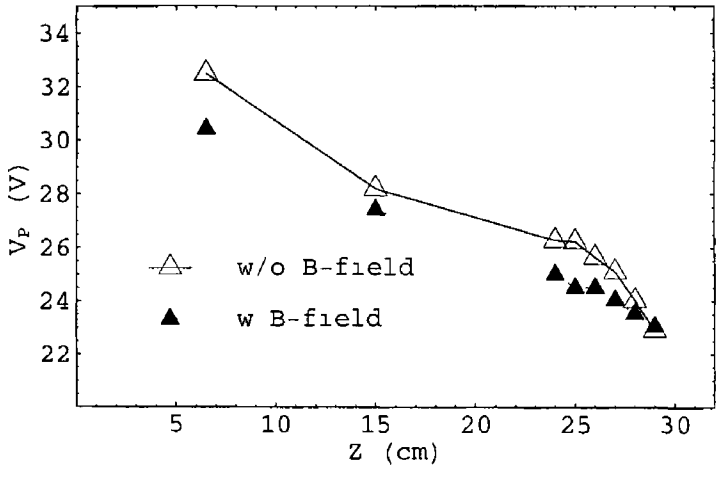

Figure 5 9 *Plasma potential (V) in the diffusion chamber Filled triangles data for magnetised (with magnetic filter) end plate and unfilled triangles data for unmagnetised (without magnetic filter) end plate*

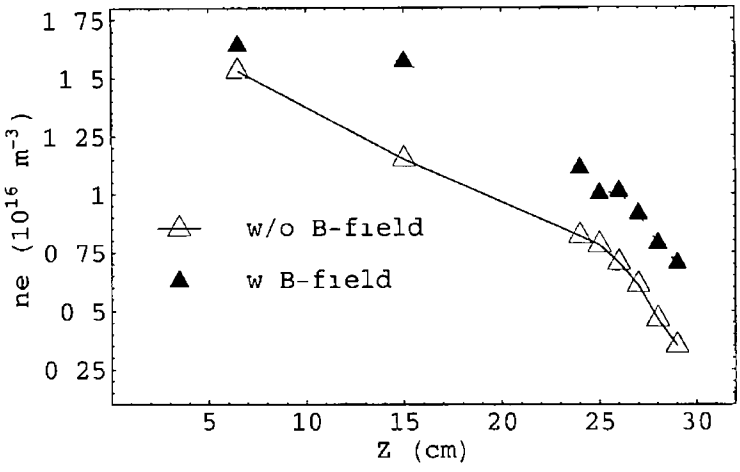

Figure 5 10 *Electron density ($\times 10^{16}$ m^{-3}) in the diffusion chamber Filled triangles data for magnetised (with magnetic filter) end plate and unfilled triangles data for un-magnetised (without magnetic filter) end plate*

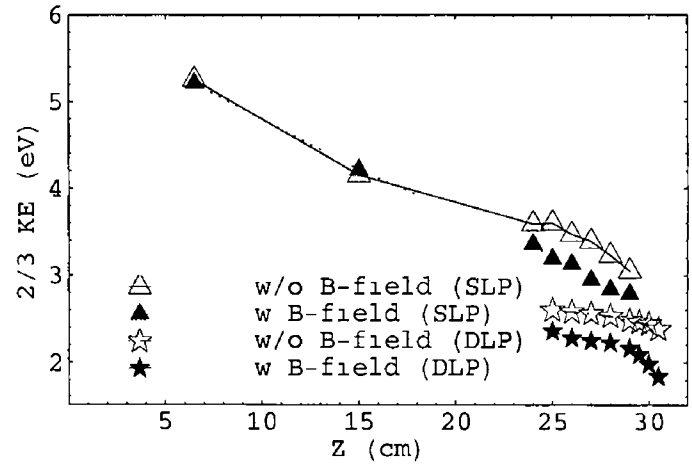

Figure 5 11 *Electron temperature (eV) in the diffusion chamber T_e calculated from measured EEDF with single Langmuir probe filled triangles data for magnetised (with magnetic filter) end plate and unfilled triangles data for un-magnetised (without magnetic filter) end plate Star data sets correspond to T_e measured with a double Langmuir probe (1 4 mTorr Argon, 1 25 kW) filled stars with magnetic field, unfilled without magnetic field*

5.1.2 Cavity ring down spectroscopy results: negative ion measurements in the diffusion chamber in ARIS

Introduction

The negative ion density is measured in the diffusion chamber in the ARIS experiment using Cavity Ring Down Spectroscopy (CRDS) technique, basic details of this technique have been described in section 3 3 The neutral gas used is Hydrogen at 5 mTorr A negative Hydrogen ion (H^-) is present in small quantities in low pressure Hydrogen discharges The CRDS diagnostic is in general very sensitive, and it is also non-invasive The absorption of the laser radiation by the negative ion sample is actually a photo-detachment process The cross section for the process is $3\,3\times10^{-21}$ m^2 The energy threshold for the process is 0 75 eV We use a Nd YAG laser tuned at the second harmonic (532 nm) for which the photons have an energy 2 33 eV The cavity is 1 meter long and the mirror's reflectivity is $\sim$ 99 998 %, the reflectivity of the mirrors can be affected by the plasma The corresponding base ring down time (τ_o) for this set up is in the range 20-30 μs

We find that for H^- density measurements the experimental sensitivity of the CRDS technique is low if the negative ion density is below 10^{14} m^{-3} In order to improve the sensitivity we use a combination of numerical integration of the CRDS signal and large number of samples records This way we have increased the sensitivity of the technique by at least one order of magnitude, the standard deviation with the integration technique is one order of magnitude smaller while averaging of thousands of samples reduces the standard error by another order or magnitude Details of the CRDS data analysis are presented in section 3 3

CRDS measurements were taken in the diffusion chamber at Z= 20 cm, see figure 5 1 The diffusion chamber end plate used during all the CRDS measurements is made of non ferromagnetic material aluminium The CRDS measurements were taken with three different magnetic setups with no magnetic field, with magnetic multi-cusp on the end plate of the diffusion chamber and with the multi-cusp plus an arrangement of multi-pole permanent magnet bars around the cylindrical wall of the diffusion chamber Magnetic flux through the end plate is of the order 100 G The magnetic flux through the cylindrical walls of the diffusion chamber is partially shielded due to the ferromagnetic characteristic of the wall material (stainless steel) Twelve small (Samarium Cobalt, 5 kG, $5 \times 1 \times 1$ cm^3) magnetic bars are used around the cylindrical walls of the diffusion chamber The magnetic confinement in the diffusion chamber is poor compared to other experimental setups such as those reported in references [1, 16, 24, 63] and others

Results and discussion

Figure 5 12 shows the negative ion density as a function of neutral gas pressure Filled triangles correspond to measurements with permanent magnets at end plate and around the diffusion chamber (full magnetised chamber case) The un-filled triangles correspond to measurements with permanent magnets only on the end plate of the diffusion chamber And the un-filled box correspond to measurement without any permanent magnets on the diffusion chamber

Figure 5 12 shows that the highest negative ion density correspond to the lowest pressure when the diffusion chamber is fully magnetised An increase in pressure or a reduction of the magnetic confinement result in lower H^- density As shown on the previous section the presence of magnetised walls

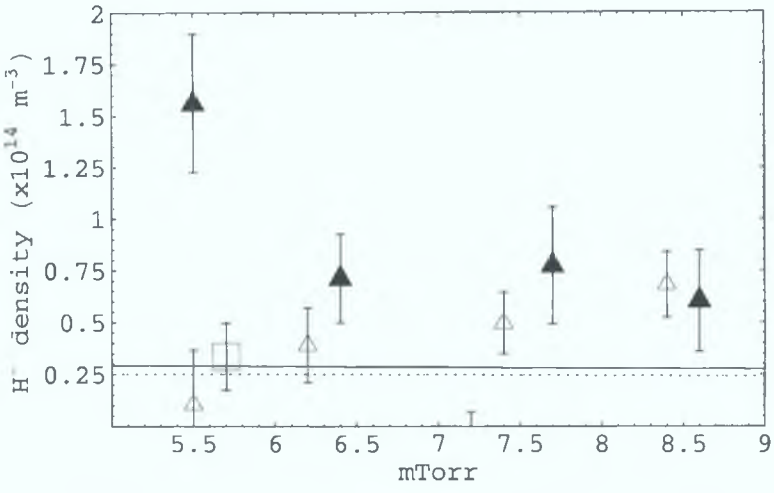

Figure 5.12: *Negative hydrogen ion density as a function of neutral pressure in the diffusion region in ARIS; 750 W. Filled triangles are for full magnetised chamber including the end plate, unfilled triangles for a magnetised end plate only and unfilled box for a non-magnetised chamber. Continuous and dotted lines correspond to Global Model results with and without magnetic confinement respectively.*

decreases the electron temperature and increases the plasma density, which favours the negative ion production when the electron temperature is above 1 eV [7, 22]. Also single particle model, section 5.2.1, shows that the magnetic confinement improves at low pressure. The neutral density affects the plasma transport from the source to the diffusion chamber and form the plasma bulk to the chamber walls.

Also Global Model results are included in figure 5.12. The Global Model was developed by R. Zorat and is described elsewhere [11–13]. The diffusion chamber dimensions are input in the model and the power is set to 500 W while pressure is scanned in the range 1-10 mTorr. Although the power input in the experiment is 750 W it is believed that most of that power is lost in the source and only a fraction of it is actually deposited in the diffusion chamber, therefore 500 W is an optimistically high input power when compared with

the real experiment. Particle losses to the chamber walls can be controlled with an option in the Global Model; this resembles a boundary condition such as magnetic confinement. The model is run with no confinement and 75% cofinement, this being a very optimistic situation compared to the actual setup on the diffusion chamber in ARIS.

The negative ion density predicted by the model with no confinement is clearly small and compares well with the experimental result. On the other hand the confined result is slightly higher and underestimates the negative ion density, specially at low pressure. This, combined with Langmuir probe results, lead us to believe that a global model is not capable of producing good quantitative results for the diffusion chamber in ARIS. The non local approximation is not applicable here, a two or three dimensional self-consistent model is required to produce better results.

Figures 5.13 and 5.14 show other parameters product of the global model as a function of pressure. Figure 5.13 shows that the plasma potential and the electron temperature decrease with pressure and confinement. This are typical results from global models. Figure 5.13 shows the electron density and again the negative ion density as functions of pressure. It shows that the densities increase with confinement, this is in qualitatively good agreement with the CRDS results. It also shows that the negative ion density is less than 1% of the electron density. This low proportionality is expected in the experimental results although it has not been confirmed with probe measurements.

The Global Model results confirms that the electron temperature drops while the density increases with improved confinement. We expect the electron temperature to be larger than 1 eV, therefore a drop in T_e simultaneously with an increase in density will favour the negative ion production [7]. Still

another important element in the chemistry of the negative ion production are the vibrationally excited molecules of Hydrogen. Figure 5.15 shows the density of excited levels 1 to 9 for the confined (continuous curve) and unconfined (dotted curve) case. The lower the excited level the higher the density. The effect of confinement is to increase the density of the low energy levels (1-4) and to reduce the density of the high energy levels. According to table 1.1 it is the highest levels which have the largest collision cross section and the lowest energy thresholds for the dissociative attachment which creates the negative ion.

A high electron temperature plasma is required to produce a rich in high vibrational energy Hydrogen molecules. This is where a source decoupled form the diffusion/extraction region is required. Langmuir probe results show that in ARIS the source is decoupled from the diffusion region. Therefore it is possible that the increase in negative ion density measured at low pressure and largest confinement is the product of a high density and low temperature effect in the diffusion chamber combined with a large flux of vibrationally excited Hydrogen molecules from the source into the diffusion chamber; note that the probe measurements show the electron temperature in the source is higher at lower pressures. Since the Global Model assumes the plasma parameters are uniform it is clear why it fails to exhibit better quantitative agreement with the experimental results.

The limitation of the Global Model can be analysed by estimating the electron energy relaxation length. This requires to calculate the electron-neutral and electron-electron collision frequencies. For noble gases the electron-atom collision frequency is given by [28]

$$\nu_a(\varepsilon) = \nu_0 p \left(\frac{\varepsilon}{\varepsilon_1}\right)^{\gamma} \tag{5.1}$$

where p is the pressure in Pascal, ε is the electron energy in eV and pa-

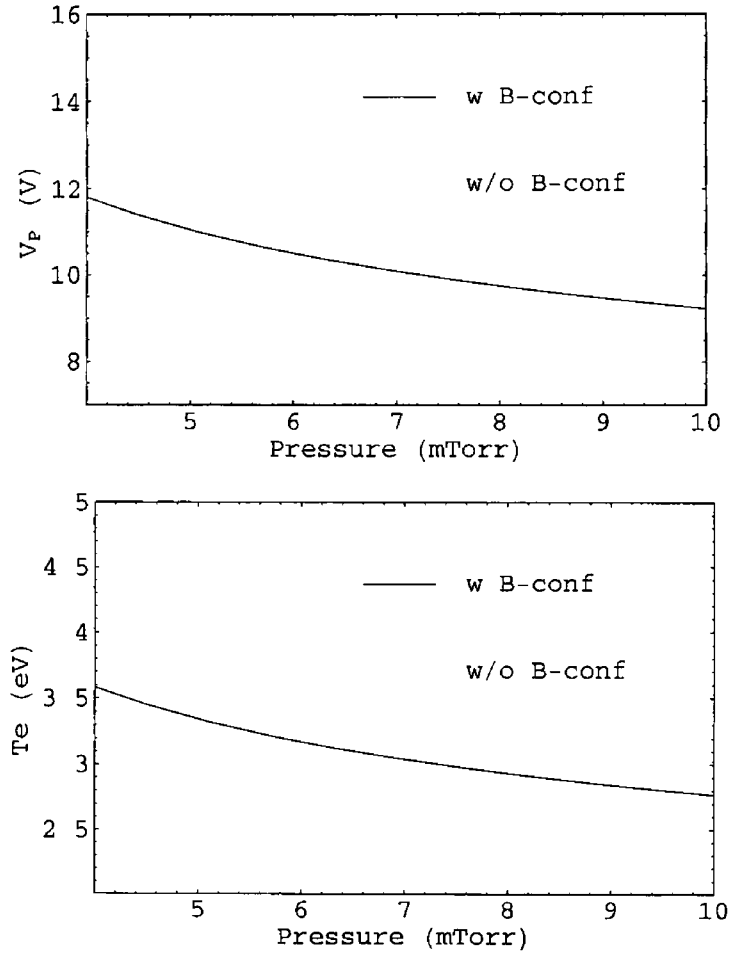

Figure 5 13 *Plasma potential and electron temperature as functions of pressure from Global Model with and without confinement*

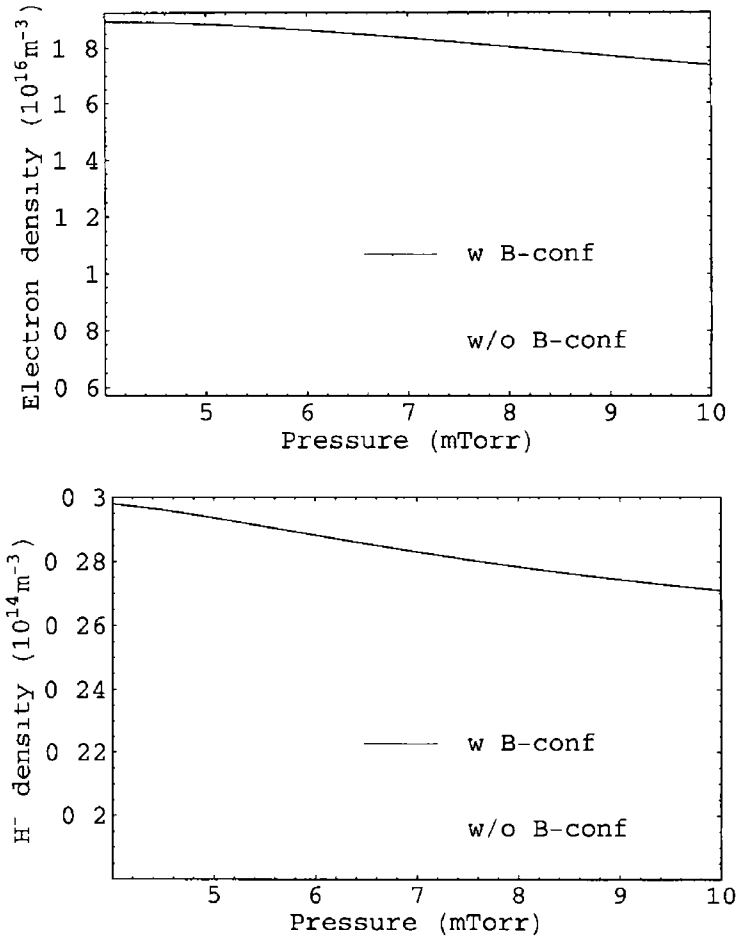

Figure 5 14 *Electron and negative ion densities as functions of pressure from Global Model with and without confinement*

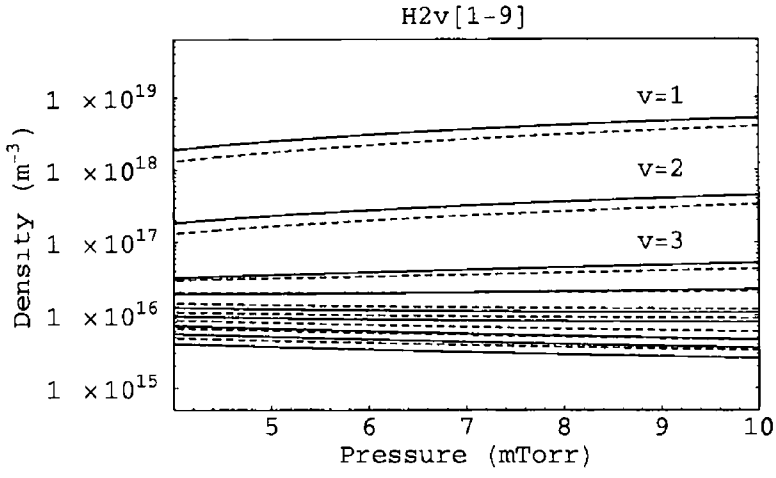

Figure 5 15 *Density of vibrationally excited Hydrogen molecules for levels 1 to 9 (top to bottom) of the electronic ground state Continuous and dotted curves with and without confinement respectively for every vibrationally excited molecule density*

rameters $\nu_0 = 1\,28 \times 10^8$ $s^{-1}Pa^{-1}$, $\varepsilon_1 = 11\,2$ eV and $\gamma = 3$ in the case of Argon The electron-electron collision frequency of and electron with other electrons which have a Maxwellian distribution and temperature T_e (eV) is given by [28]

$$\nu_{ee}(\varepsilon) = 1\,54 \times 10^{-11} \frac{n_e}{\varepsilon^{3/2}} \ln\left(5\,17 \times 10^{12} \varepsilon \sqrt{\frac{T_e}{n_e}}\right) \qquad (5\,2)$$

where n_e is the electron density in m^{-3} and ε is the electron energy in eV Figure 5 16 shows the electron-atom elastic collision for Argon as a function of electron energy for pressures 1 and 10 mTorr It also shows the electron-electron collision frequency for electron densities 10^{15}, 10^{16} and 10^{17} m^{-3} and $T_e = 3$ eV The electron-electron collision frequency has a week dependence with the electron temperature It is clear that only for low energy electrons the electron-electron collisions would be dominant The energy relaxation

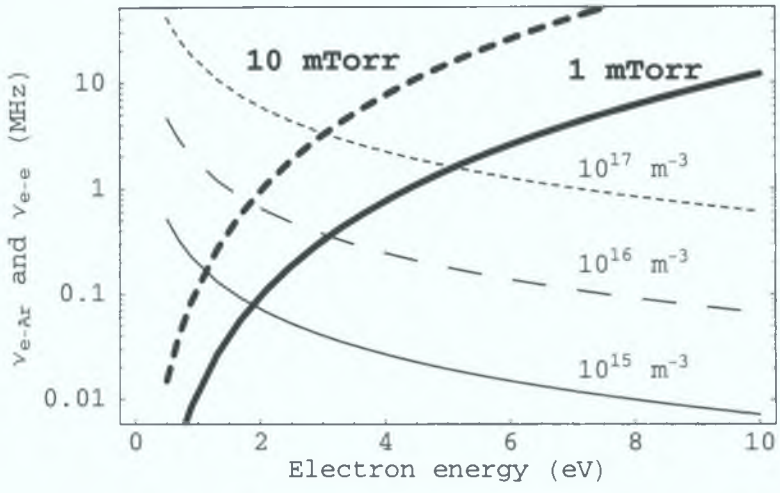

Figure 5.16: *Elastic electron-atom (bold curves) and electron-electron (thin curves) collision frequency as a function of electron energy. The electron-atom collision frequency is shown for 1 and 10 mTorr Argon neutral gas while the electron-electron collision frequency is shown for three different electron densities and* $T_e = 3$ *eV.*

length is given by [28]

$$\lambda_\varepsilon = 2\sqrt{\frac{D_e}{\nu_{ee} + \delta\nu_a + \nu^*}} \tag{5.3}$$

where $D_e = \lambda_e v/3$ is the electron diffusion coefficient , $\delta = 2m_e/m_{atom}$ and $\nu_e e$, ν_a and ν^* are the electron-electron, electron atom elastic and electron-atom inelastic collision frequencies respectively. The electron mean free path is calculated $\lambda_e = v/\nu_e(v)$ and the electron collision frequency is given by addition of the electron-electron and electron-atom collision frequencies. Figure 5.17 shows the electron energy relaxation length as a function of electron energy for 1 and 10 mTorr Argon neutral gas, three different electron densities and $T_e = 3$ eV. Curves for each density split in two branches when the electron-atom collision dominate where the lower branch correspond to the highest pressure. The inelastic collision frequency (ν^*) is roughly estimated as a factor of 0.05 of the electron-atom collision frequency when the

electron energy is above the first excitation threshold energy (inelastic cross sections are roughly one order of magnitude smaller than elastic collision for electron-Ar collisions). The purpose of this approximation is to show that electrons with enough energy to undergo inelastic collisions with neutrals have a considerably smaller energy relaxation length. The relaxation length in figure 5.17 becomes almost independent of the electron density for the high energy electrons; electron-Ar collisions dominate in this range.

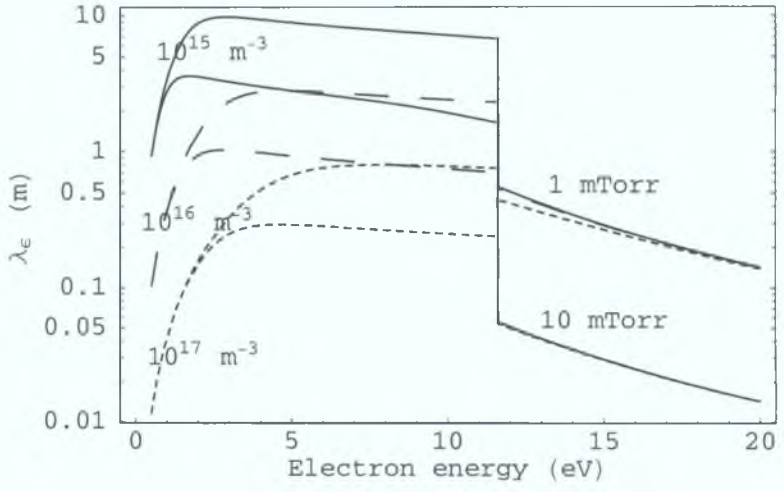

Figure 5.17: *The electron energy relaxation length as a function of electron energy for 1 and 10 mTorr Argon neutral gas, three different electron densities and* $T_e = 3\ eV$.

It is clear now that the energy relaxation length of the low energy electrons is comparable or larger to the diffusion chamber dimensions for the measured plasma density while the energy relaxation length of the high energy electrons is considerably smaller, at best comparable to the diffusion chamber length. Therefore, this is not enough to sustain a uniform plasma in the diffusion chamber, it would be required a considerably larger relaxation length; this can be achieved at lower pressures. Effectively, most of the high energy electrons, from the source, are sustaining a plasma in the vicinity of the

source-diffusion region A global model would require $\lambda_\epsilon \gg L$, where L is the typical size of the device

The analysis of the energy relaxation length has been limited to the case of Argon

5.2 Computational results

5.2.1 Study of single particle transport into a magnetic multi-cusp

Introduction

Here we present the results of the model of single particle dynamics into a magnetic multi-cusp The model is described in section 4 1 Two magnetic configurations (as seen on figures 4 2a and 4 2c) and a non-magnetised case are modelled The non-magnetised results are used to compare the effects of the magnetic field on the single particle transport on the other two situations The particles studied are electrons In addition to the magnetic field effects on the particle transport, elastic collisions are considered in the model The background gas is molecular hydrogen The collisional effects are studied for a wide range of pressure 0 1-100 mTorr The electric field is neglected m the model In-between collisions, the particle trajectories are determined by the Lorentz force Since the particles only experience elastic collisions and the magnetic field force is perpendicular to the particle trajectory the energy of each particle is conserved through all the trajectory Each particle trajectory is integrated up to 1 μs in time The boundary conditions are that the particle may return to the plasma bulk ($y > 10$ cm in figure 4 2), be collected by the magnetised boundary ($y < 0$ cm in figure 4 2) or remain in the modelled region after 1 μs, the particle is bounced back at $x = -3$ and $x = 3$ cm Results are organised in three groups according to the particle final state

The effect of particle-neutral collisions becomes important when the collision frequency becomes greater than the cyclotron frequency Effectively the

particle can not complete an orbit around the magnetic field lines and therefor is said to be non-magnetised On the contrary if the cyclotron frequency is greater than the collision frequency then particle may complete more than one orbits around the field lines and is said to be magnetised Figure 5 18 shows a log-scale plot of the cyclotron and collision frequencies for 3 eV electrons as a function of the distance to the magnetised boundary (at $y = 0$) The cyclotron frequency is calculated for the magnetic field intensity down form the front of a magnetic bar face ($|\mathbf{B}(x = 1\,5, y)|$ or $|\mathbf{B}(x = -1\,5, y)|$) and down from in-between bars ($|\mathbf{B}(x = 0, y)|$) The collision frequency is calculated for the different neutral pressures (0 1-100 mTorr) assuming the neutral pressure is constant through the modelled region Figure 5 18 shows that at low neutral background pressure (< 10 mTorr) particles (electrons) are magnetised everywhere in the modelled region It is also clear that even at higher pressure (up to 100 mTorr) the particles remain magnetised when close to the magnetised boundary (where the high intensity magnetic field)

Results

For every magnetic field configuration and for the non-magnetised case the model is run for sixteen different pressures 0 1, 0 2, 0 3, 0 5, 0 7, 1, 2, 3, 5, 7, 10, 20, 30, 50, 70 and 100 mTorr Every run requires a large number of single particle shots in order to achieve a good statistical representation of the particles distribution (Maxwellian) One million electrons are shot for each pressure and magnetised or non-magnetised configurations

For every run the number of particles bounced back to the plasma bulk, retained in the magnetised region and collected by the magnetised boundary are recorded Magnetised cases are compared to non-magnetised case by calculating

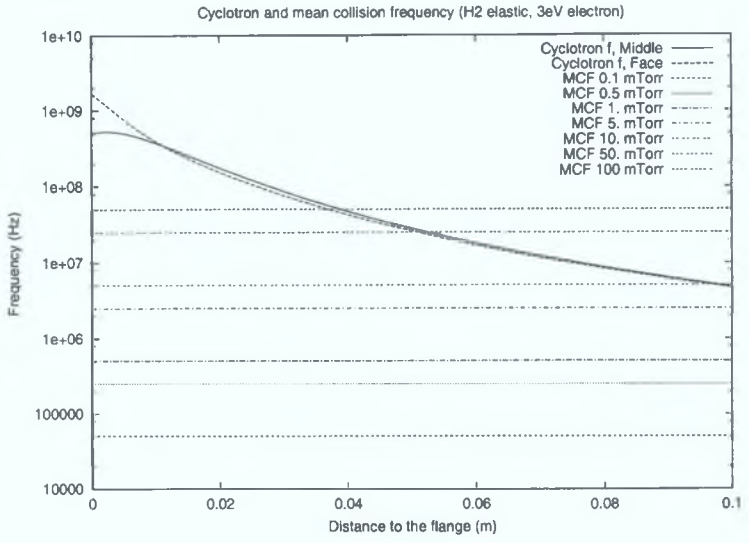

Figure 5.18: *Cyclotron frequency and mean collision frequencies for electrons with energy 3 eV as a function of the distance (y) to the magnetised boundary ("flange"). The cyclotron frequency is calculated for the magnetic field intensity (*$|\mathbf{B}|$*) from the magnetic bar face and in-between bars into the magnetised region. The collision frequency is calculated for neutral pressures 0.1-100 mTorr.*

(a) The ratio of the number of particles bounced back to the plasma when magnetised to the number of particles when non-magnetised,

(b) The ratio the number of particles retained in the magnetised region when magnetised to the number of particles when non-magnetised (after 1μs) and

(c) The ratio of the particles collect by the magnetised boundary when magnetised to the number of particles when non-magnetised.

Figure 5.19 shows a log-linear plot of the ratios (b) and (c) for both magnetised configurations as a function of the neutral pressure. Diamonds correspond to ratios (b) and the pentagons to ratios (c). Open diamonds/pentagons correspond to the two magnetic bar configuration (figure 4.2a) and filled

diamonds/pentagons correspond to the symmetric multi-cusp configuration (figure 4 2c) Both magnetic configurations present qualitative similar results Ratios (b) and (c) show that at low neutral pressure the number of particles collected and in the magnetised region is small compared to the non-magnetised case This is due to the effective confinement which reduces the losses at the magnetised boundary to almost null and pushes back the particles to the plasma At intermediate pressures (5-10 mTorr) ratio (b) shows some sort of trapping effect where the particles are prevented from being lost at the magnetised boundary, indicated clearly by ratio (c) which remains well below 10%, but also prevented from returning back to the plasma bulk At higher pressure (50-100 mTorr) ratio (b) equals unity indicating that the magnetic field effect on the magnetised region is destroyed by the neutral collisions In spite of this ratio (c) is below 40this indicates that even at high pressure the magnetised boundary magnetic field is strong enough to control the particle losses

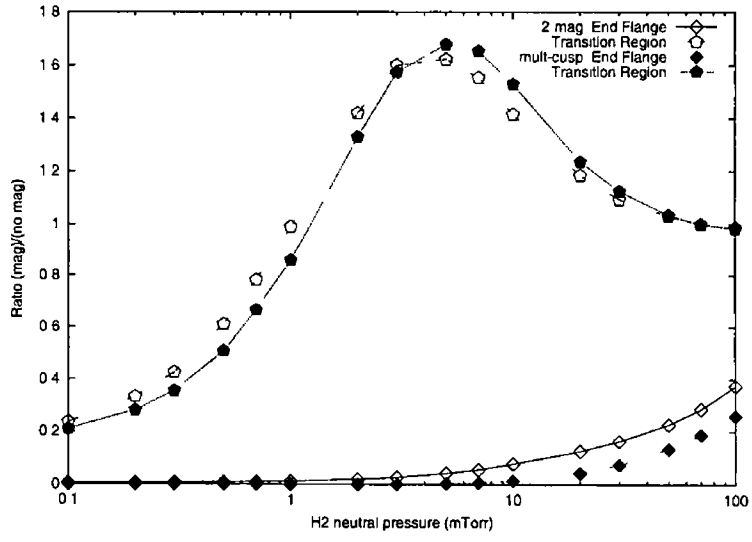

Figure 5 19 *Log-linear plot of ratios (b) and (c) as a function of pressure for two-magnets and multi-cusp configurations*

The field effect on the particle losses to the magnetised boundary can be seen on figure 5.20. Here, we present a normalised plot of the particle losses to the magnetised boundary (at $y = 0$) as a function of x and neutral pressure 0.1-100 mTorr (front to back respectively). The magnetic bars are centred at $x = -1.5$ and $x = 1.5$ cm, and are 1 cm width facing the magnetised region. Figure 5.20a and 5.20b correspond to the two magnetic bar (figure 4.2a) and symmetric multi-cusp (figure 4.2c) configurations respectively. It is clearly seen that for both magnetic configurations the particle losses occur only at the cusps (the magnetic bar faces to the magnetised region) at low pressures (< 10 mTorr) but that at higher pressures the more frequent particle-neutral collisions disrupt the orbits allowing some particles to lose from the magnetic field lines.

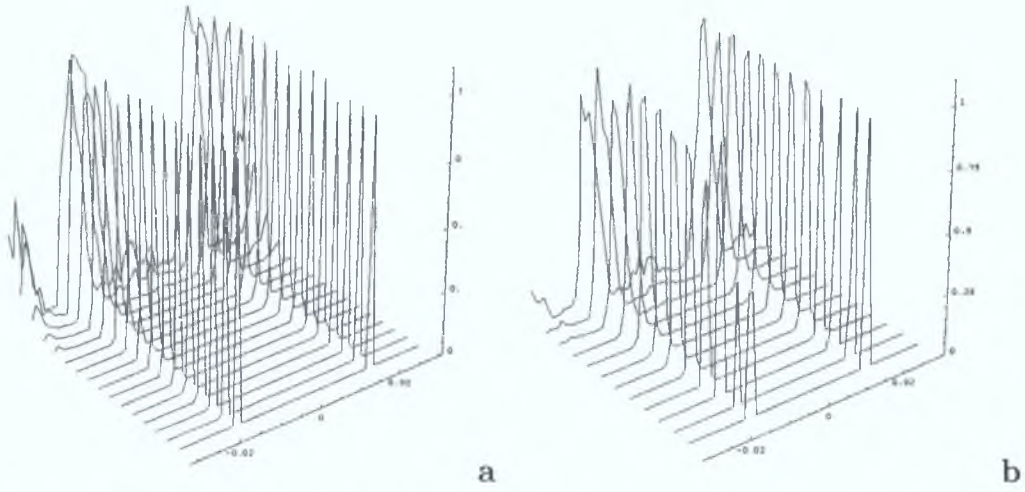

Figure 5.20: *Normalised plot of the particle losses to the magnetised boundary ("flange") as a function of x for pressures 0.1 (front) to 100 mTorr (back). For two magnet (a) and symmetric multi-cusp (b) configuration.*

The spatial distribution of the particles retained in the magnetised region (x:[-3,3] and y:[0,10] cm) after 1μs can provide us some insight of the magnetic field effect on the particles transport and confinement. Figure 5.21 shows a

schematic diagram of the modelled region in the X-Y plane. It shows a cross section of the magnet bars (which extend infinitely in the Z axis) and delimits the magnetised region. The spatial distribution of particles is plotted as on this delimited region with the same orientation in figures 5.23, 5.24 and 5.25 for the non-magnetised, two bar and symmetric multi-cusp configurations respectively. These figures are normalised so that the same colour scale is

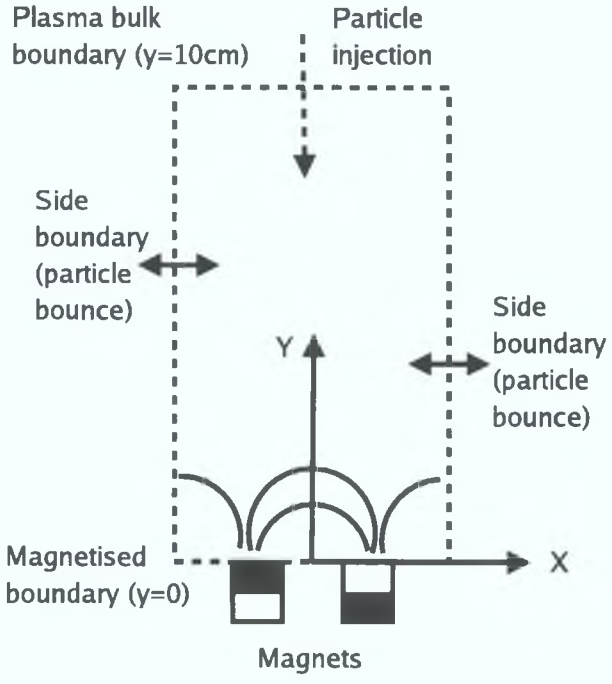

Figure 5.21: *Schematic diagram of the modelled magnetised region on the X-Y plane.*

used on every pressure and magnetic configuration; the colour scale is shown in figure 5.22.

Figure 5.22: *Normalised colour scale for figures 5.23, 5.24 and 5.25.*

Figure 5.23, 5.24 and 5.25 show spatial density distribution plots for dif-

ferent background pressures left to right and top to bottom the pressure are 0 1, 0 2, 0 3, 0 5, 0 7, 1, 2, 3, 5, 7, 10, 20, 30, 50, 70 and 100 mTorr Figure 5 23 is presented as a reference to the magnetised configuration results

Figures 5 24 (two bar magnetic configuration) and 5 24 (symmetric multicusp) show that at low pressures (< 5 mTorr) the particle distribution follow the magnetic field lines as seen on figures 4 2a and 4 2c respectively This is, the particles are clearly magnetised and orbit around the field lines Also is clear the effect of the magnetic field is to contain the particles away the magnetised boundary, only to have an escape point where the field lines are perpendicular to the X-Z plane at the cusps The non-magnetised density plots (5 23) are clearly different from the magnetised ones (5 24 and 5 25) at low neutral pressures but turn to be quite similar at higher pressures (> 50 mTorr) The cusps are clearly defined at low pressure but quite undistinguishable at the highest pressure The main difference between magnetic configurations is on the field lines themselves But overall we observe the same qualitative effect

The pressure (collisions) effect is to destroy the electron orbits around the magnetic field trajectories This enables many particles to cross perpendicularly to the magnetic field lines and access regions of high magnetic field other than the cusps The density plots make evident the strong confinement of the electrons by the magnetic field with some particle trapping in the magnetised region at low pressures, (electrons bounce between magnets, see electron trajectories) and reduced magnetic effect for high pressures but still with some confinement effect at the magnetised boundary compared with the magnetic free case (from figure 5 20)

Figures 5 26 show three sample particle trajectories on the X-Y plane (modelled region as sketched on figure 5 21) for three different electrons

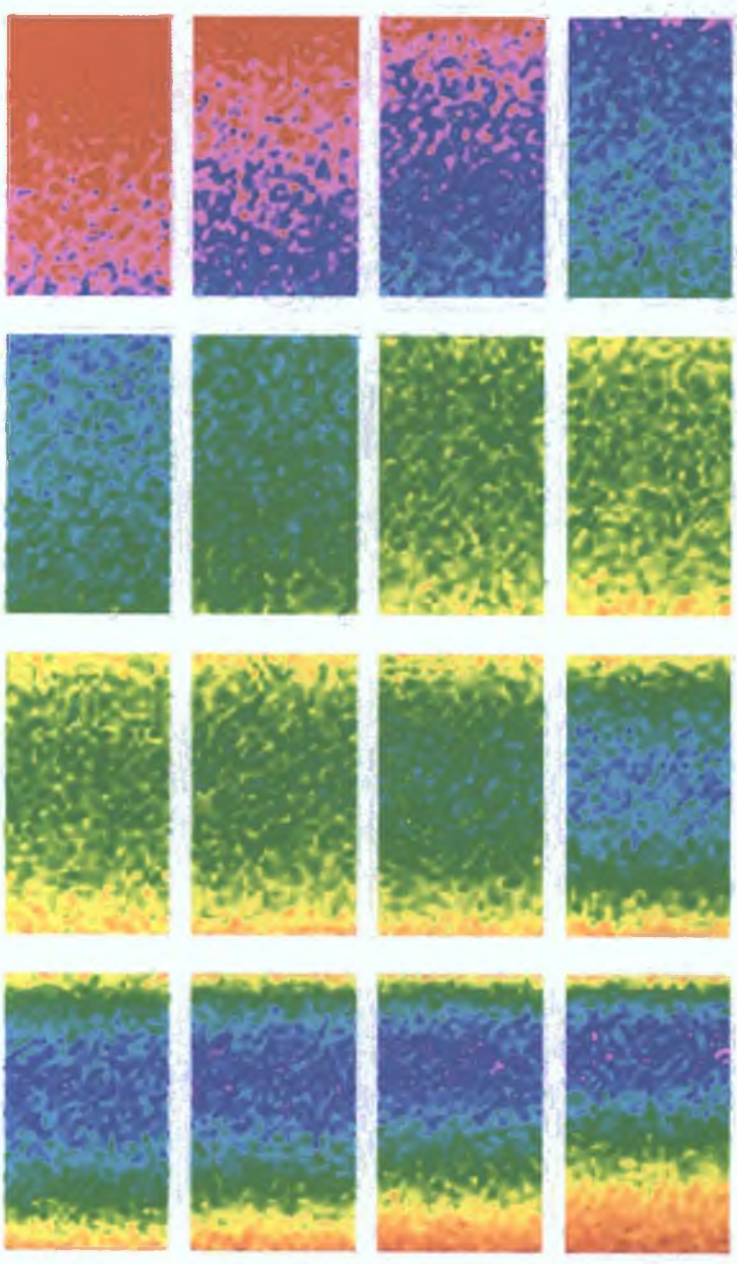

Figure 5.23: *Density plot of intermediate region between plasma and end boundary (non-magnetised). From left to right and top to bottom the H_2 neutral pressures are: 0.1, 0.2, 0.3, 0.5, 0.7, 1, 2, 3, 5, 7, 10, 20, 30, 50, 70 and 100 mTorr.*

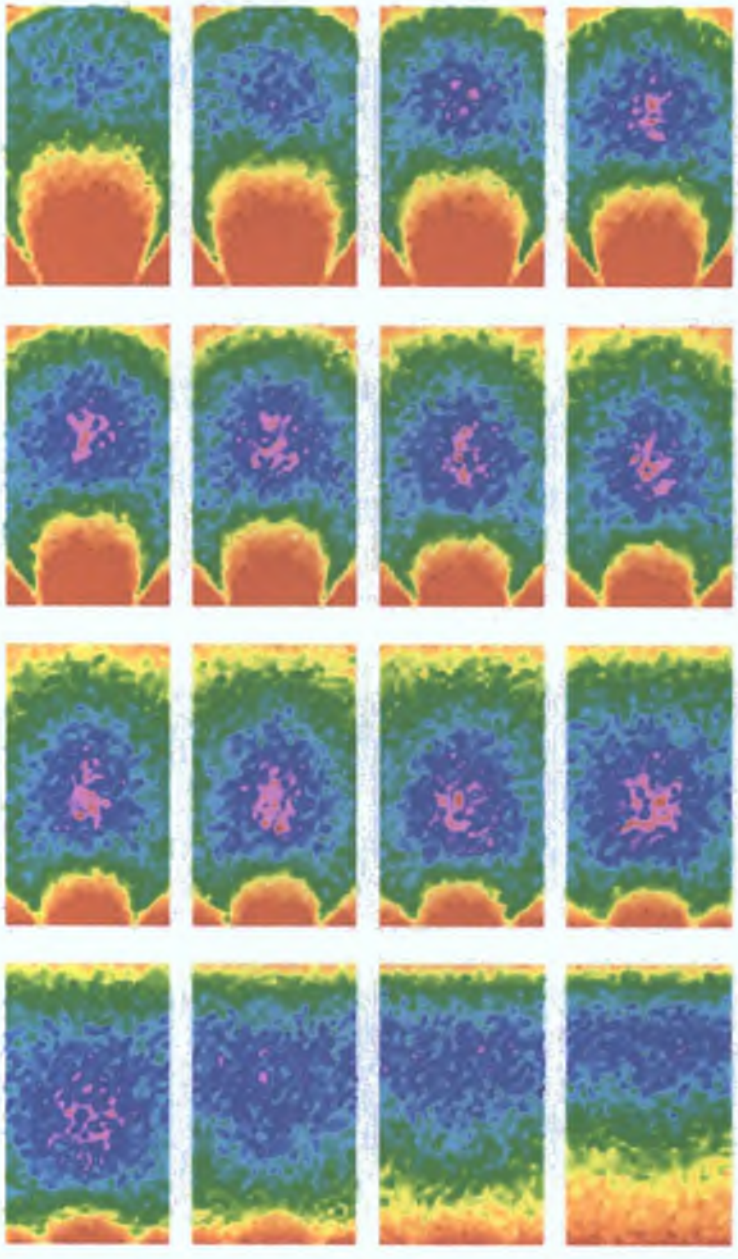

Figure 5.24: *Density plot of magnetised region between plasma and the magnetised boundary for the two magnetic bars configuration. From left to right and top to bottom the H_2 neutral pressures are: 0.1, 0.2, 0.3, 0.5, 0.7, 1, 2, 3, 5, 7, 10, 20, 30, 50, 70 and 100 mTorr.*

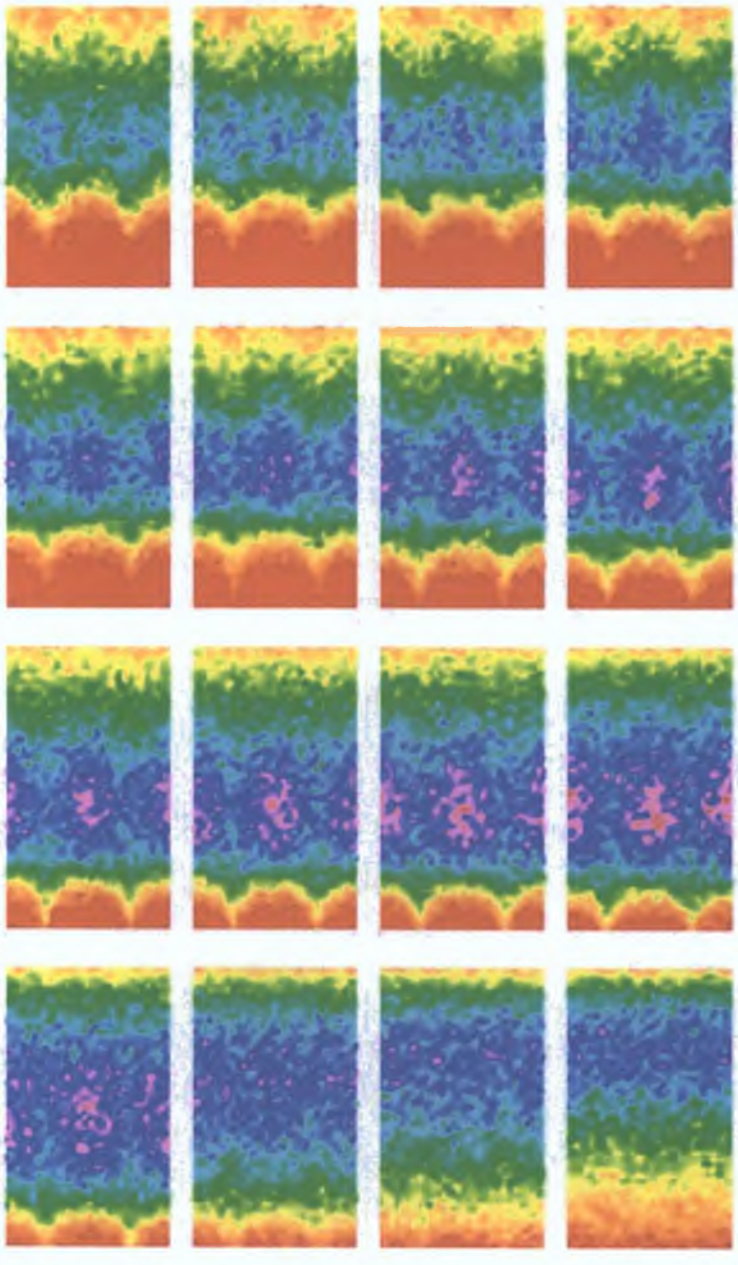

Figure 5.25: *Density plot of magnetised region between plasma and the magnetised boundary for the symmetric multi-cusp configuration. From left to right and top to bottom the H_2 neutral pressures are: 0.1, 0.2, 0.3, 0.5, 0.7, 1, 2, 3, 5, 7, 10, 20, 30, 50, 70 and 100 mTorr.*

The neutral background pressure is 1 mTorr. The magnetic field configuration corresponds to the two single magnetic bars (non symmetric cusps; figure 4.2a). The particles centre of giro-radius follows the magnetic field lines. This correlates with the particle density plots, in particular for the 1 mTorr case on figure 5.24. The field lines, the sample trajectories and the density plots fit with the expected magnetic confinement effect at low pressure.

After careful inspection of the trajectories on figures 5.26 we can find a discrete number of non-smooth changes in direction. At these nodes the particle experiences an elastic collision which randomises the particle velocity direction; but not the velocity modulus. These instantaneous changes in direction disrupt the particle trajectory on the magnetic field; otherwise pre-determined for its entire existence. Random collisions allow the particles to suddenly change velocity direction and transport across the magnetic field lines, accessing space regions otherwise forbidden for given the initial conditions. The higher the neutral pressure the less constrained are the trajectories by the magnetic field lines; as seen on the density plots (figures 5.24 and 5.25). Figures 5.26 show clearly the change of particles orbit. It is easily seen on figure 5.26b where after a series of elastic collisions the particle gain access to a region of higher magnetic field. As seen on figure 5.20 the particles are mainly lost at the cusps; this is when the particle velocity is almost parallel with the magnetic field line. The criteria for the loss is given by the loss cone; explained in Appendix C.

At low pressures the particles trajectories centre of giro-radius, following the field lines, present an oscillatory behaviour between the cusps. According to the density plots (figures 5.24 and 5.25) it is most probable to find the particles in between the cusps as opposed to at the edge of their trajecto-

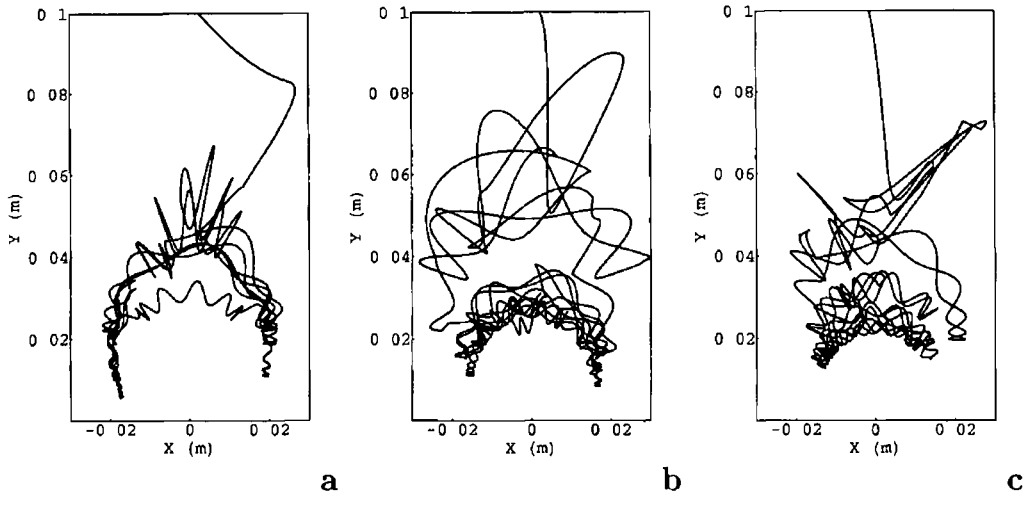

Figure 5 26 *Particle trajectories on the X-Y plane for three different electrons (a, b, c) Modelled region as sketched on figure 5 21*

ries, close to the cusps This is explained as follows The particles velocity does not change in modulus (kinetic energy is conserved) since the magnetic field can only change the velocity direction and the particle-neutral collision considered are elastic (particle energy is conserved, not momentum) If the modulus of the velocity does not change then the particle travels a certain distance per time unit uniformly (regardless of the trajectory shape it-self) The particle cyclotron frequency is independent of the particle energy but only depends on the particle charge to mass ratio and the magnetic field intensity, equation (4 24) The particle Larmor radius (giro-radius) is a function of the particle velocity and charge to mass ratio and magnetic field intensity

$$r_{\text{Larmor}} = \frac{v_{\perp}}{\Omega} = \frac{|\mathbf{v} \times \mathbf{b}|}{\Omega} = \frac{v \sin\theta}{\Omega} \tag{5 4}$$

where $\Omega = 2\pi f_{\text{cyclotron}}$, $\mathbf{b}$ is the magnetic field directional vector (unitary) and θ is the angle between vectors $\mathbf{v}$ and $\mathbf{b}$ It is clear then that the larger the magnetic field the smaller the Larmor radius and therefore, for a given

cyclotron frequency, the shorter the path around the giro-centre. Since the particle move with constant velocity modulus then it would spend more time in low magnetic field regions (large Larmor radius) than in high magnetic field regions (cusps) where the Larmor radius is small[1].

Electric, gravitational or any other force fields other than the force due to the magnetic field have been neglected on this model. Usually other forces would produce a drift velocity perpendicular to the magnetic field lines. Though if the magnetic field ($\mathbf{B}$) is not constant throughout the space then there is a drift velocity due to the magnetic field gradient.

$$\mathbf{v}_{\text{drift}} \propto \frac{\mathbf{B} \times \nabla B}{B^2} \tag{5.5}$$

This drift velocity is perpendicular to the magnetic field lines and the gradient of the magnetic field intensity, both on the X-Y plane, therefore on the Z axis. Since the particle position in the Z axis is not important due to the assumption that the magnetic bars are infinitely long it is consistently neglected. It is important to notice that in a real system this would cause charge separation because it will push opposite charges in opposite directions on the Z axis so that a self-consistent electric field would develop.

[1]This effect is the opposite to a pendulum where the velocity of the particle (velocity modulus not constant) is maximal at the centre of the trajectory and minimal at the edges. The mass in the pendulum spends more time at the edges of its trajectory.

5.2.2 *Probe*-PIC model results

Introduction

Here we present the results of a kinetic model of a plasma in the vicinity of a Langmuir probe. The model solves the plasma sheath around a cylindrical Langmuir probe and records the electron and ion currents collected by the probe surface as a function of the probe bias voltage. Therefore recorded current-voltage data reproduce the probe characteristic (I-V trace) which can be correlated with plasma parameters with collisional and/or other effects (RF plasma potential, photo-detachment signal for plasmas with negative ions). Further systematic studies with this model can provide parametrised relations of the plasma parameters and collected currents as a function of neutral species density (collisional effects).

As an example of multiple-ion plasma we set the model to reproduce a photo-detachment signal of a fictitious negative ion plasma (e^-,Ar^+,Ar^-).

Steady state solution for a dc biased probe

We dc bias the probe boundary and run the simulation for different background pressures in search for a steady state on the model. The steady state is evaluated from the particle collection at the probe surface and the total number of particles per specie.

The main input parameters for the model are set as follows: probe radius $r_o = 0.2$ mm, probe length 10 mm, plasma radius 10 mm, probe bias $V_B = -30$ V, plasma potential $V_P = 0$ V, plasma density $n_o = 10^{15}$ m^{-3}, electron temperature $T_e = 3$ eV and Ar^+ temperature $T_i \simeq 0.026$ eV (300 K). Therefore the following parameters defined by Laframboise [37]

$$-\frac{V_B}{T_e} = 10 \qquad \frac{T_i}{T_e} \simeq 0.0086 \qquad \frac{r_o}{\lambda_{De}} \simeq 0.466$$

Four different runs are made at background pressures 0, 1, 5 and 10 mTorr Null background pressure means the model runs collision-less Electron inelastic collisions are disabled for all this runs This is to prevent departures of density and electron temperature, which could occur given the set electron temperature (3 eV)

Orbital Motion Limited vs collision-less Probe-PIC model

The electron and ion densities and space potential as functions of radius can be compared with a numerical solution of the Vlasov and Poisson equations for a collision-less plasma around a cylindrical probe (Laframboise [37]) For the given plasma parameters, the space potential steepness is less than that of an inverse square or the radius This is the condition for Orbital Motion Limited (OML) [37] Figures 5 27 and 5 28 show normalised densities and space potential from *Probe*-PIC model (collision-less case) and the Vlasov-Poisson solution The potential profile for both results are in well agreement while the electron and ion density agree well over most of the range except in the sheath The electron density as calculated from *Probe*-PIC output data exhibit a similar profile as the Vlasov-Poisson solution, with very small differences The ion density solutions depart from each other in the sheath, while the numerical solution exhibits an almost constant density in the sheath and a sharp drop in density at the probe radius the PIC model output data presents a modulation of the density in the sheath and a sharp rise at the probe radius This is probably associated with a small population of trapped ions (closed orbits around the probe)

Figure 5 29 shows a snapshot of the ion phase space $(r - v_r)$, ions moving towards the probe have negative radial velocity ($v_r < 0$) and the ones moving away from the probe have positive radial velocity ($v_r > 0$) The

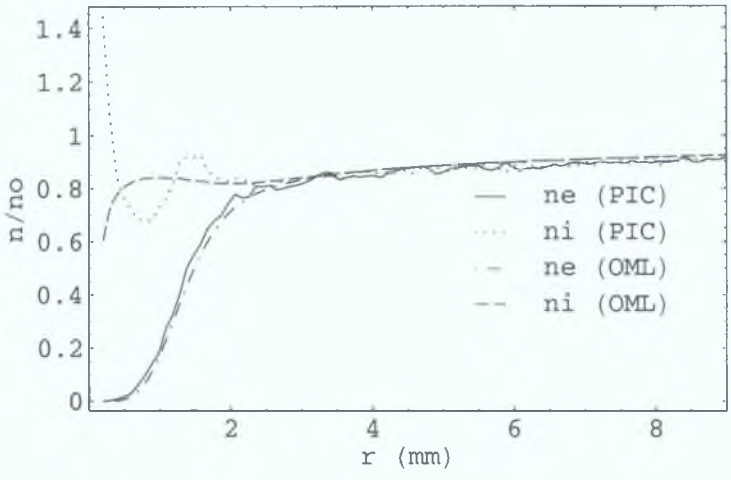

Figure 5.27: *Normalised electron and ion densities as function of radius from Probe-PIC model (collision-less) and numerical solution of the Vlasov-Poisson equations.*

phase space shows ions being accelerated into the probe in the probe sheath ($r_o < r < 2$ mm); getting larger negative radial velocity. It also shows that there are some fast ions coming from the probe in the sheath; decelerating towards the probe. Since the ion specieshas been set to have a thermal distribution some ions have enough angular momentum and are able to orbit the probe at radius larger than the probe radius. Those are the ions out-coming from the probe, seen in the sheath. Figure 5.30 presents the ion phase space ($v_r - v_\theta$) taken at radius intervals: $r_o < r < 2$ (sheath), $4 < r < 6$ and $8 < r < 10$ mm. First we observe that particles come injected with some small drift velocity (plasma radius region) set to prevent the development of electric fields at the plasma boundary. Second, as we look into regions closer to the probe we see an unpopulated region of the velocity phase space; that region corresponds to a group of particles that would be travelling back to the plasma if they had not been collected by the probe (a velocity loss cone) or would be trapped orbiting around the probe (total energy ≤ 0). Finally,

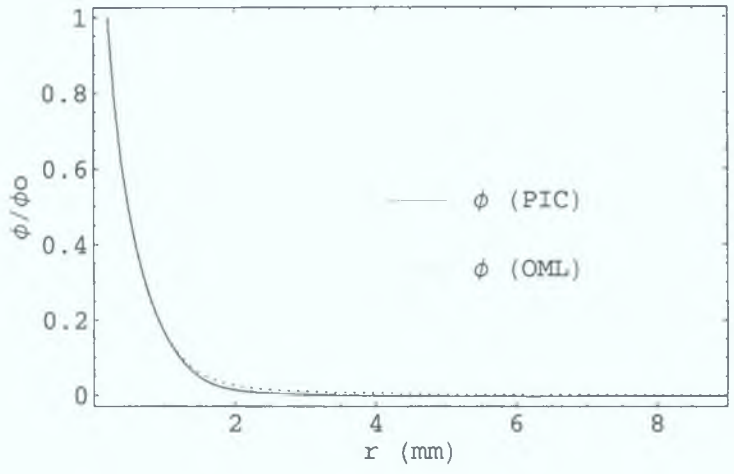

Figure 5.28: *Normalised space potential as function of radius from Probe-PIC model (collision-less) and numerical solution of the Vlasov-Poisson equations.*

we observe particles with large enough angular momentum to orbit the probe at a radius larger than the probe radius; this particles have positive radial velocity in the sheath region (out-coming ions).

Sheath solutions with collisional effects

Figure 5.31 shows the ion phase space $(r - v_r)$ for background pressure 5 mTorr. The observed effect of increasing pressure is the destruction of the orbits. As collisions are allowed, the ions start to fall in the forbidden region (for the collision-less case) of the phase space (in the sheath); where the total energy and angular momentum would not allow their trajectories to go through. Therefore the orbital motion limited approximation is not valid anymore. This forbidden region of the phase space corresponds to ions with total energy smaller than the potential energy; ion-particle collisions relax the ions energy.

Figures 5.32 and 5.33 show the normalised densities and space potential as functions of radius for runs with background pressure 0 (collision-less), 1,

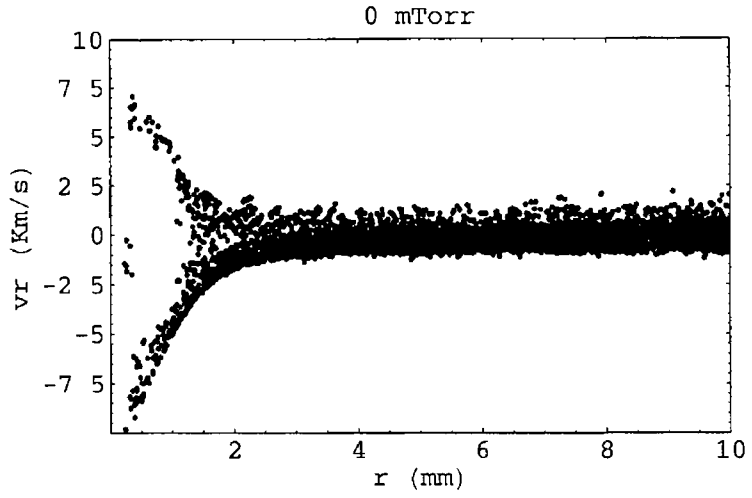

Figure 5 29 *Snapshot of ion phase space ($r - v_r$), collision-less case*

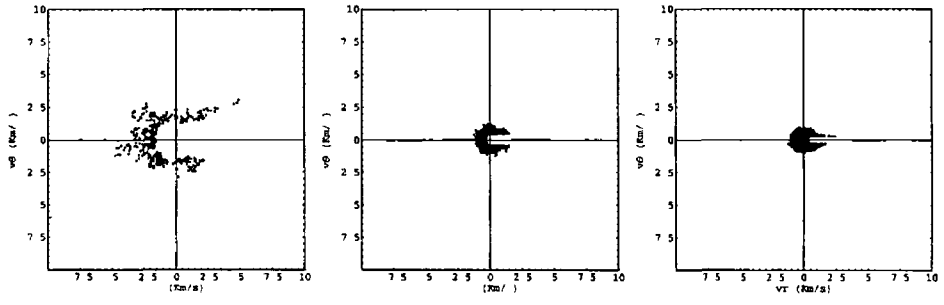

Figure 5 30 *Snapshots of the velocity ion phase space ($v_r - v_\theta$) for particles in $r_o < r < 2$ (sheath), $4 < r < 6$ and $8 < r < 10$ mm, collision-less case*

5 and 10 mTorr On the ion density we observe that the modulation in the sheath for the collision-less case is not seen on the collisional cases But the sharp rise of density at the probe surface prevails And for the collisional runs (1, 5 and 10 mTorr) the ions density in the sheath is very similar After the sheath the overall density (electrons/ions) drops as pressure is increased Collisions destroy orbits so that the ion current collected by the probe is expected to increase [39, 40, 69] In this model in particular charge exchange has the largest cross section Charge exchange collisions change the

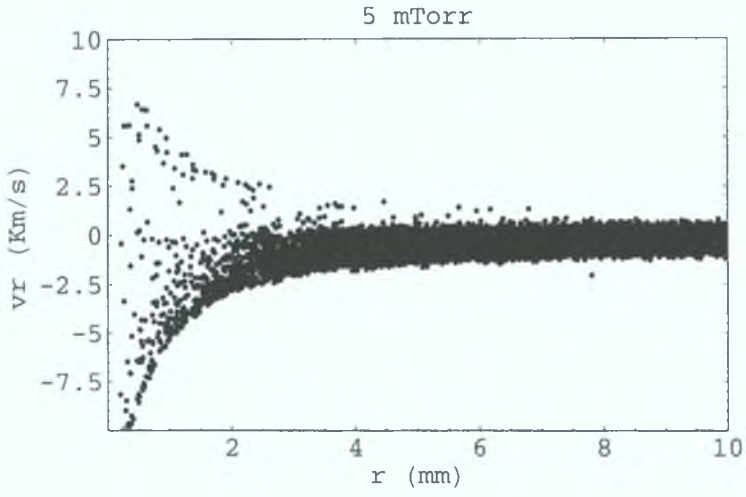

Figure 5.31: *Snapshot of the ion phase space ($r - v_r$); background gas pressure 5 mTorr.*

ions kinetic energy to thermal energies, therefore losing the energy gained by the electric field. Collected ion currents are 13.74 ± 1.47, 20.22 ± 1.63, 21.81 ± 2.21 and 21.00 ± 2.06 μA for background pressure 0 (collision-less), 1, 5 and 10 mTorr respectively. Collisions also affects the ion transport. The sheath/pre-sheath expands with pressure to accelerate the ions into the probe.

Current-voltage characteristics

In this section we present results of the recorded electron and ion current collected by the probe surface while the probe is biased. We have a singular opportunity here to examine the ion and electron currents separately and apply some of the standard analysis techniques on them; determining the electron and the ion currents is not a problem for the model as it is for experimentalists.

The main input parameters for the model are set as follows: probe radius $r_o = 0.2$ mm, probe length 10 mm, plasma radius 10 mm, probe bias sweep

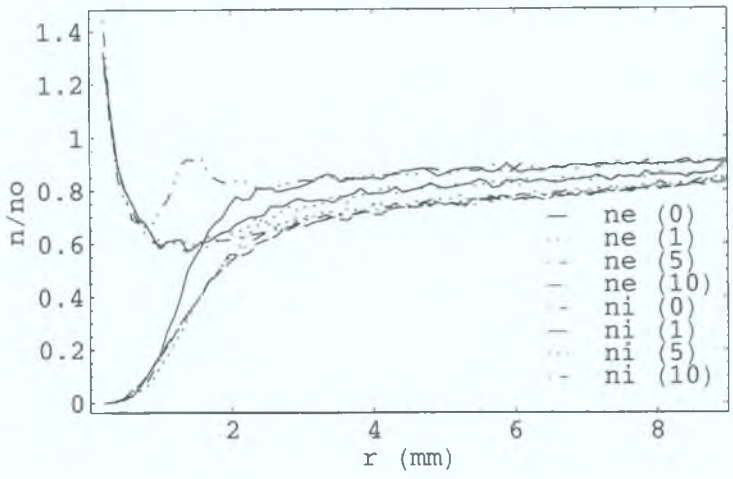

Figure 5.32: *Normalised electron and ion densities as function of radius (Probe-PIC) for background pressure 0 (collision-less), 1, 5 and 10 mTorr.*

from $V_B = -50$ V to $V_B = 20$ V in 0.1 ms (equivalent to a 10 kHz sawtooth or a 5 kHz triangular voltage signal), plasma potential $V_P = 0$ V, plasma density $n_o = 10^{15}$ m^{-3}, electron temperature $T_e = 3$ eV and Ar^+ temperature $T_i \simeq 0.026$ eV (300 K). The Laframboise parameters remain unchanged from last section. Four different runs are made at background pressures 0, 1, 10 and 100 mTorr. Again null background pressure means the model runs collision-less. Also electron inelastic collisions are disabled for all this runs to prevent departures of density and electron temperature; which could occur given the set electron temperature (3 eV).

The model is run for given parameters at each pressure with the probe biased $V_B = -50$ V until a steady state is achieved. Then the bias voltage is linearly increased up to $V_B = 20$ V in 0.1 ms while the ion and electron currents to the probe are recorded.

Typical current-voltage characteristic in a collision-less case

We set the pressure to 0 mTorr to make a collision-less run. Figure 5.34

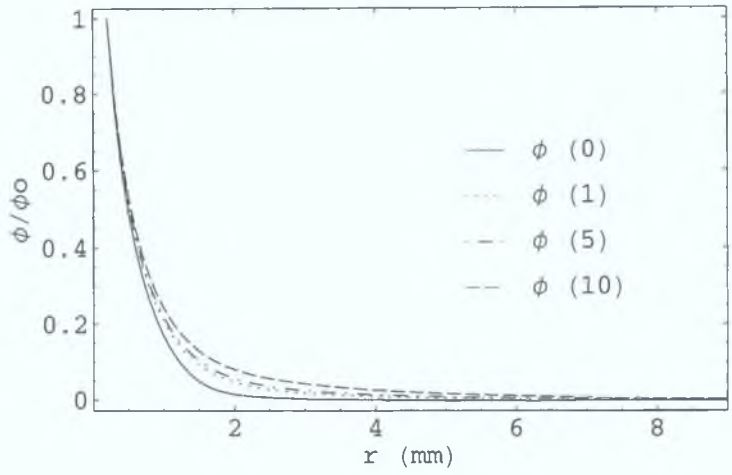

Figure 5.33: *Normalised space potential as function of radius (Probe-PIC) for background pressure 0 (collision-less), 1, 5 and 10 mTorr.*

shows the total current, electron plus ion current, collected by the probe as a function of probe bias. As expected for a cylindrical probe the trace does not show a flat electron saturation for bias voltage greater than the plasma potential ($V_B > V_P = 0$).

Following standard techniques to analyse the probe data, we take the natural logarithm of the electron current. A linear fit of the data between bias voltages -15 and 0 V is performed. The inverse of the slope of the fitted line is calculated, it is the electron temperature estimation. Figure 5.35 shows the log-scaled electron current and best linear fit. The electron temperature calculated is 3.0 eV which is in perfect agreement with the input value set for the model. This shows that the electron retardation region is an exponential function, also in good agreement with the Maxwellian distribution function set on the injected particles at the plasma boundary. The deviations of the fitted line at bias voltages ≤ -20 V are due to low particle collection. The resolution of the logarithm of the electron current at large negative bias voltages indicates the fact that the model runs with a finite number of

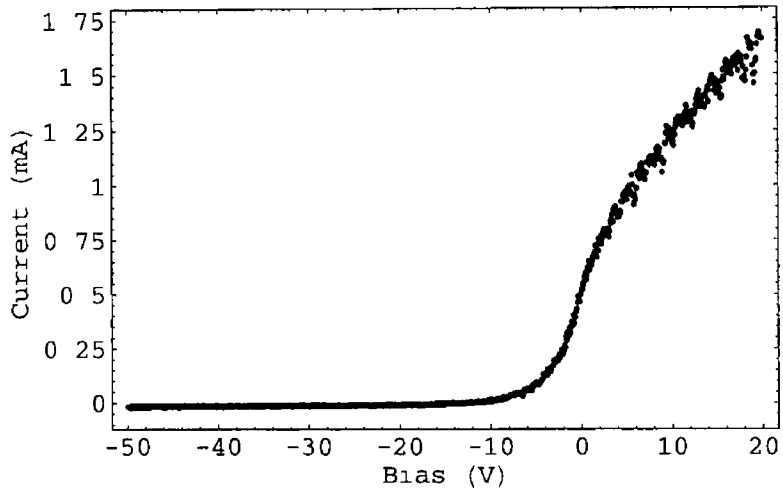

Figure 5 34 *Current-voltage characteristic (Probe-PIC), collision-less case*

particles, super-particles representing many real particles (Similar resolution effects can be seen on experimental results but in that case it is related to the bit resolution of the measuring device)

The plasma electron density can be calculated equating the random thermal flux of the electrons to the current density collected by the probe at $V_B = V_P = 0$, equation (3 3) The electron density calculated is $8\ 78 \times 10^{14}$ m^{-3} which underestimates the set density for the model 10^{15} m^{-3} But the average electron density at the plasma boundary $9\ 19 \times 10^{14}$ m^{-3} compares better with the I-V trace estimated density

We use the space potential profile to verify that the ion motion is Orbital Motion Limited (OML) Therefore we can use the collected ion current to estimate the ion density using equation (3 6) Figure 5 36 shows the ion current as a function of the probe bias and the best fit of the OML current formula The ion density from the OML formula is over estimated by a factor of $\sim 2\ 1$ respect to the estimated electron density from the electron current and a factor of $\sim 1\ 9$ respect to the input density set for the model Over-

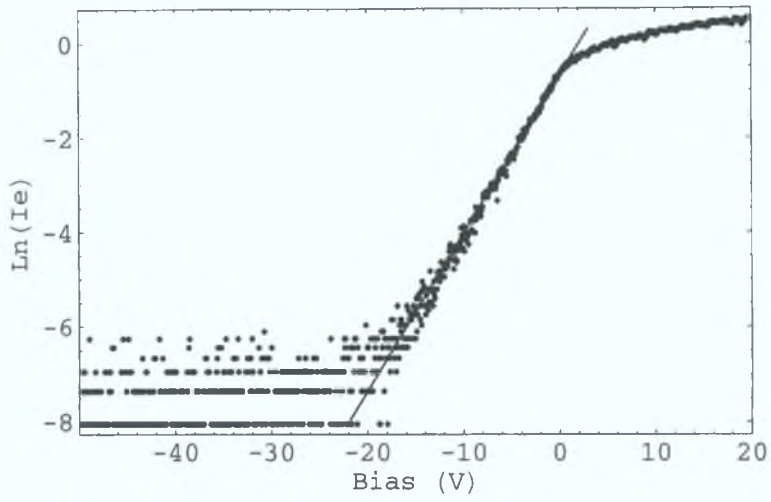

Figure 5.35: *Natural logarithm of the electron current (Probe-PIC) and linear fit. Collision-less case.*

estimation of the density by the ion saturation current is a known fact in Langmuir probes [35, 38]. Usually the discrepancy of electron and ion density is explained by ion collisions in the probe sheath/pre-sheath [39, 40, 69]. Though in this case the model has been run collision-less so the discrepancy has to be explained differently. Anisotropy could be a cause; notice the fact that the ions injected from the plasma boundary have a small drift velocity in v_r (see figure 5.30).

Typical current-voltage characteristic under collisional conditions

Now we turn our attention into the *Probe*-PIC results with collisional effects. Three orders of magnitude on background neutral pressure are explored; 0, 1, 10, 100 mTorr (higher pressures can be set although it would result computationally more expensive due to the high collision frequency restrictions on the model time step). The collision-less results (0 mTorr) are included to compare also the non-collisional case with collisional results.

Figure 5.37 shows the electron current collected by the probe at the differ-

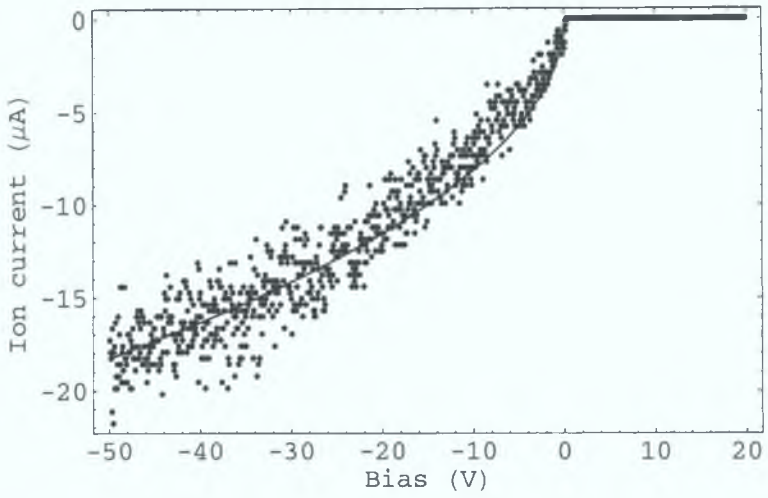

Figure 5.36: *Ion current (Probe-PIC) and OML current formula. Collision-less case.*

ent background pressures. The collision-less case and 1 mTorr case are hardly distinguishable. The effect of higher background pressure is to increase the electron collection; this will clearly overestimate the electron density.

The electron temperature and electron saturation current are calculated from the electron currents using the standard technique. The electron density is estimated using the set for the model ($T_e = 3$ eV) for all pressures and with the calculated T_e for each pressure. The results are presented in table 5.1. The measured electron temperature increases with pressure, it does not appear to be a distribution energy distortion after inspection of the natural logarithm of the electron currents (not shown). The electron saturation current increases with pressure and as expected the electron density is overestimated respect to the electron density at the plasma boundary, even using the measured –higher– electron temperatures, except for the collision-less case (0 mTorr).

Figure 5.38 show the ion saturation currents for 0 (collision-less), 1, 10, 100 mTorr background neutral pressure. We see that the ion curves increase

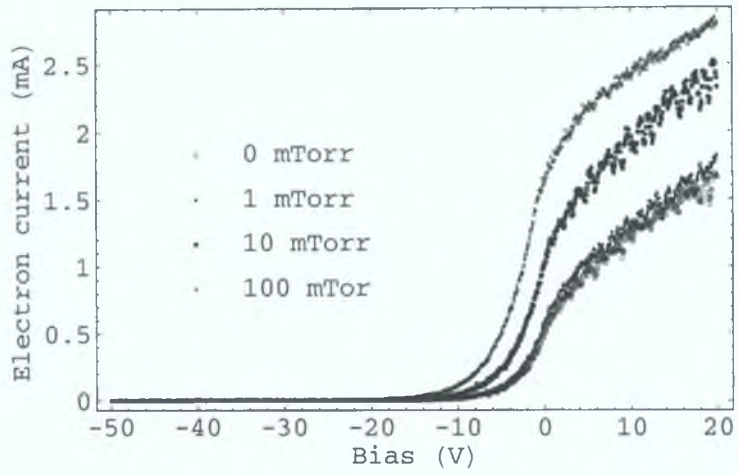

Figure 5.37: *Electron current (Probe-PIC) at 0 (collision-less), 1, 10 and 100 mTorr background pressure.*

with pressure from 1 to 10 mTorr but drops to approximately half the ion current for the collision-less case. The collision-less result has already been analysed using OML theory, we find that the average ion density at the plasma boundary is over estimated by a factor ~ 1.9. Therefore for pressures 1 and 10 mTorr the ion density is further overestimated while for 100 mTorr case OML results are in better agreement; the last agreement is just by chance. Since OML theory is a collision-less theory, we are not going to do any further analysis of the ion currents with it. The validity of OML is questionable even for the lowest pressures. Experimental evidence of this has been presented by Sudit and Woods [83] for low pressure and medium density plasmas.

The full current-voltage characteristics result from the addition of the electron current (figure 5.37) and the ion current (figure 5.38); not shown here. This curves show statistical noise due to the limited number of particles used on the model ($\sim$ 15000 per specie). The characteristics consist of a 1000 current-voltage pairs. To reduce this noise, we perform a Gaussian

Table 5.1: *Plasma parameters calculated form electron currents in figure 5.37. Electron densities estimated with $T_e = 3$ eV† and with calculated T_e‡. Also average electron densities at the plasma boundary¶.*

P (mTorr)	T_e (eV)	I_{eo} (mA)	n_{eo} (m^{-3})†	n_{eo} (m^{-3})‡	n_{eo} (m^{-3})¶
0	3.0	0.51	8.78×10^{14}	8.78×10^{14}	9.19×10^{14}
1	3.1	0.57	9.80×10^{14}	9.64×10^{14}	9.19×10^{14}
10	3.3	1.03	1.76×10^{15}	1.68×10^{15}	8.96×10^{14}
100	3.5	1.63	2.80×10^{15}	2.59×10^{15}	8.48×10^{14}

convolution; the kernel function

$$K = \sum_{i=-m}^{m} \exp\left(-\frac{i^2}{n^2}\right) \tag{5.6}$$

This function is normalised for $n = 20$ and $m = 30$. The resulting I-V traces are smooth enough to take numerical derivatives (the smoothing function may distort the characteristics, experimentally I-V traces are averaged from many samples to reduce the noise, computationally that is very expensive option; another possibility is to increase the number of super-particles). Figures 5.39 and 5.40 show the first and second derivatives of the current voltage characteristics (0, 1, 10 and 100 mTorr).

Plasma potential determination is usually done experimentally using the first or the second derivatives of the I-V traces. So far we have used the plasma potential ($V_P = 0$ V) set at the model for the density and electron temperature analysis. Now we use the recorded I-V traces to actually estimate the plasma potential. The plasma potential is taken as the bias voltage corresponding to the maximum of the characteristic first derivative ($dI/dV|_{V=V_P} = \max(I'(V))$) or the zero crossing of the second derivative

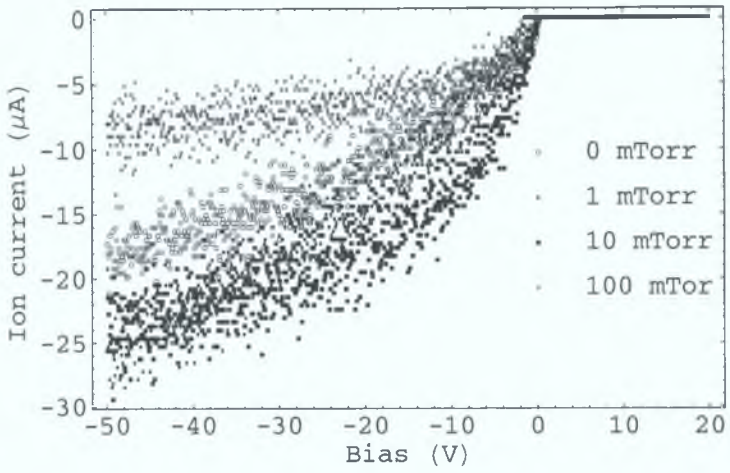

Figure 5.38: *Ion current (Probe-PIC) at 0 (collision-less), 1, 10 and 100 mTorr background pressure.*

($\mathrm{d}^2I/\mathrm{d}V^2|_{V=V_P} = 0$). Ideally the zero crossing of the second derivative and the maximum at $V_B < V_P$ (see figure 5.40) should occur at the same bias voltage. Experimentally this does not happen due to low collection of low energy electrons; the model reproduces this effect as well. Table 5.2 show the calculated plasma potential for the given pressures from the first and second derivatives, and the voltage difference of the plasma potential (from second derivative) and the bias voltage for which the second derivative is maximum. This analysis reveals that at higher pressures the plasma potential is underestimated. However, the gap between the zero and the maximum of the second derivative is consistently around $\sim 2.2-2.3$ V. The smoothing function actually made this difference larger than it probably is. The shift of the zero crossing of the second derivative or the peak of the first derivative could be evidence of the transition from the collision-less regime into the non-local or hydrodynamic (local) regime [28]. Using the plasma potential estimated from the second derivative we recalculate the electron saturation current using $T_e = 3$ eV and the electron temperature calculated from the

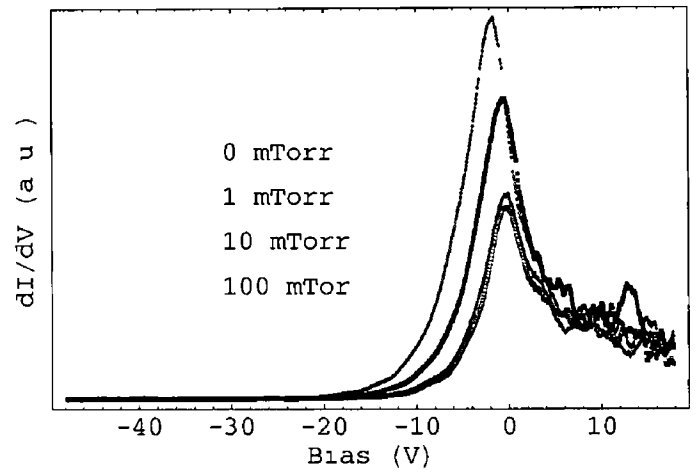

Figure 5 39 *First derivative of the current-voltage characteristic (Probe-PIC)*

electron current In table 5 3 we compare this results with the average electron density at the plasma boundary With the plasma potential from the second derivative, the electron saturation currents drop and the electron density overestimation gap reduces for 10 and 100 mTorr In the collision-less case it underestimates the density while for 1 mTorr it turns to be in good agreement, without an obvious reason to be so

The sheath radius is defined here as the radius where the absolute of the difference of the space potential ($\phi(r)$) and the plasma potential (V_P, at the plasma bulk boundary) equals half the electron temperature $|V_P - \phi(r_{\text{sheath}})| = T_e/2$ (this is an arbitrary definition, used here only for the purpose of analysis) Figure 5 41 shows the sheath radius estimated using this criteria as a function of the probe bias The collision-less (0 mTorr) and 1 mTorr cases are un-distinguishable except at large negative voltages (ion saturation) Also the effect of collisions is to expand the sheath in general in the ion saturation region while there is no apparent effect on the electron saturation region Finally notice the sheath collapses when the bias equals

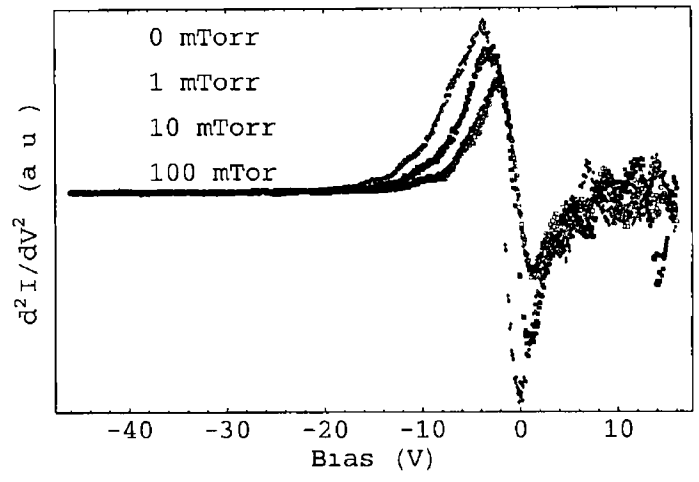

Figure 5 40 *Second derivative of the current-voltage characteristic (Probe-PIC)*

the plasma potential as expected

In summary we observe that the effect of increasing background pressure is to increase the collected electron and ion current, except for the highest pressure (100 mTorr) for the ion current This current increase result in density overestimation in the range 10-100 mTorr The electron temperature slightly increases with pressure although it shows a good Maxwellian behaviour The plasma potential appears to be underestimated as the pressure is increased

Plasma potential with RF oscillations and their effect on the current-voltage characteristic

Radio-frequency (RF) excited discharges are very common nowadays and widely used m the industry The ARIS experiment itself, presented is this thesis, is RF driven with an external antenna In this type of sources the plasma potential is expected to oscillate at the excited RF frequency This can make a Langmuir probe measurement very challenging, the probe char-

Table 5.2: *Plasma space potential calculated from first† and second‡ derivatives of the I-V traces, and the voltage difference of the plasma potential (from second derivative) and the bias voltage for which the second derivative is maximum¶.*

P (mTorr)	V_P (V)†	V_P (V)‡	ΔV (V)¶
0	-0.18	-0.25	2.16
1	-0.06	-0.30	2.15
10	-0.46	-0.70	2.27
100	-1.63	-1.77	2.24

acteristic is usually distorted. To prevent this, RF compensation is required. Some of the most common compensation techniques are describe in section 3.1.

Here we introduce RF oscillations to the plasma boundary voltage and run the model for a set of parameters and bias the probe boundary to record the I-V trace. It is analysed as usual and compared to another run results with same parameters except for the RF oscillations on the plasma potential.

The main input parameters for the model are set as follows: probe radius $r_o = 0.2$ mm, probe length 10 mm, plasma radius 10 mm, probe bias sweep from $V_B = -30$ V to $V_B = 10$ V in 0.01 ms (equivalent to a 100 kHz sawtooth or a 50 kHz triangular voltage signal), plasma potential $V_P = \sin(2\pi ft)$ V and $V_P = 0$ V for the plasma potential with and without RF oscillations respectively, plasma density $n_o = 10^{15}$ m^{-3}, electron temperature $T_e = 3$ eV and Ar^+ temperature $T_i \simeq 0.026$ eV (300 K). The Laframboise parameters remain unchanged from last two sections. The background pressure is set to 5 mTorr. Also electron inelastic collisions are disabled for all this runs.

The model is run for given parameters at each pressure with the probe

Table 5.3: *Plasma parameters calculated form electron currents in figure 5.37 using the plasma potential calculated form the second derivative of the I-V trace (table 5.2). Electron densities estimated with $T_e = 3$ eV† and with calculated T_e‡. Also average electron densities at the plasma boundary¶.*

P (mTorr)	T_e (eV)	I_{eo} (mA)	n_{eo} (m^{-3})†	n_{eo} (m^{-3})‡	n_{eo} (m^{-3})¶
0	3.0	0.49	8.43×10^{14}	8.43×10^{14}	9.19×10^{14}
1	3.1	0.53	9.19×10^{14}	9.03×10^{14}	9.19×10^{14}
10	3.3	0.88	1.51×10^{15}	1.44×10^{15}	8.96×10^{14}
100	3.5	1.19	2.05×10^{15}	1.90×10^{15}	8.48×10^{14}

biased $V_B = -30$ V until a steady state is achieved. Then the bias voltage is linearly increased up to $V_B = 10$ V in 0.01 ms while the ion and electron currents to the probe are recorded.

Probe sheath solution with radio-frequency oscillations on the plasma potential

The oscillating voltage on the plasma boundary represents the plasma potential of the plasma source oscillating at the same frequency as the RF excitation. Since the typical RF frequency (13.56 MHz) is less than the typical electron plasma frequency ($\sim 100 - 1000$ MHz) then it is the electrons which will follow the RF oscillations. Therefore the whole sheath voltage will follow the RF oscillations. Figure 5.42 shows the space potential as a function of radius and time at probe bias $V_B = -30$ V. As expected the PIC model follows the bulk plasma oscillations; modulated with a 5 V amplitude sinusoidal voltage. The voltage difference from the plasma boundary to the probe surface changes fast enough not to affect the ions but slow enough

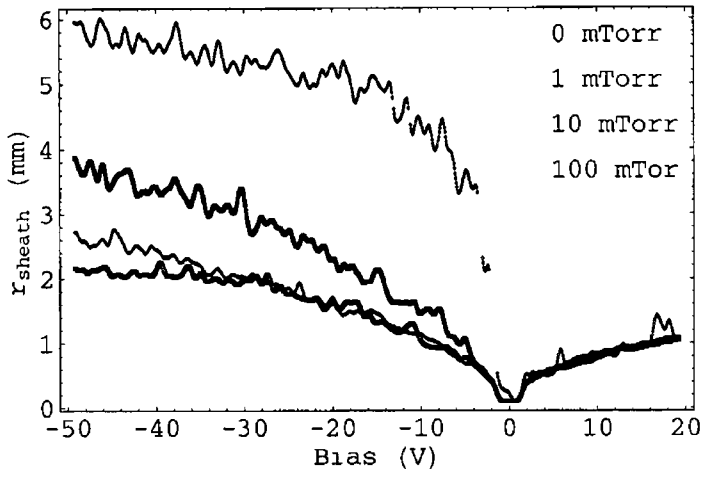

Figure 5 41 *Sheath radius (mm) (calculated using a Bhom criterion) as a function of probe bias (Probe-PIC)*

to allow electron current modulation on the probe This RF modulation explores the non-linear sheath impedance producing non-sinusoidal currents (rich in harmonics)

Current-voltage characteristic of a plasma with radio-frequency oscillations on the plasma potential

The probe is biased as described before A clear modulation of the electron current driven by the plasma potential oscillations can be seen in figure 5 43 The total time for the bias ramp is 0 01 ms while the Rf oscillation period is $\sim$ 74 ns, therefore there are about 135 RF periodic oscillations through the full ramp Experimentally current-voltage characteristics as that from figure 5 43 are not measured, but an averaged trace Experimental data averaging of many samples per bias voltage and stray capacitances produce the averaged trace

The model is run again with the same input parameters but without radio-frequency oscillations on the plasma potential in order to produce an

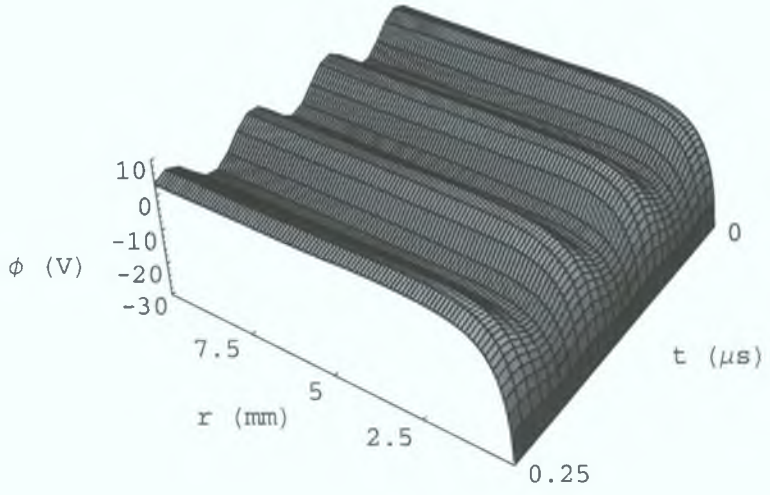

Figure 5.42: *Space potential as a function of radius and time.*

I-V trace to compare with the RF case. The ion current curves are very similar, with small differences due to noise (not shown). I-V traces are smoothed by performing a Gaussian convolution to reduce noise and to average the RF effects on the probe trace. Figure 5.44 presents the smoothed I-V traces. From the logarithm of the electron current of each trace we work out the electron temperature which is 3.2 eV for the DC plasma potential and 3.4 eV for the RF plasma potential case. This shows that for small or comparable (to the electron temperature) RF oscillations the electron temperature can be estimated, from the logarithm of the electron current. This is in agreement with analysis of Langmuir probe measurements in a Helicon plasma by Chen [59].

We have presented here the radio-frequency distortion of the probe characteristic for a RF oscillation amplitude (V_{RF} = 5 V) comparable to the electron temperature ($\sim$ 3 eV). Larger amplitude oscillations, such as found

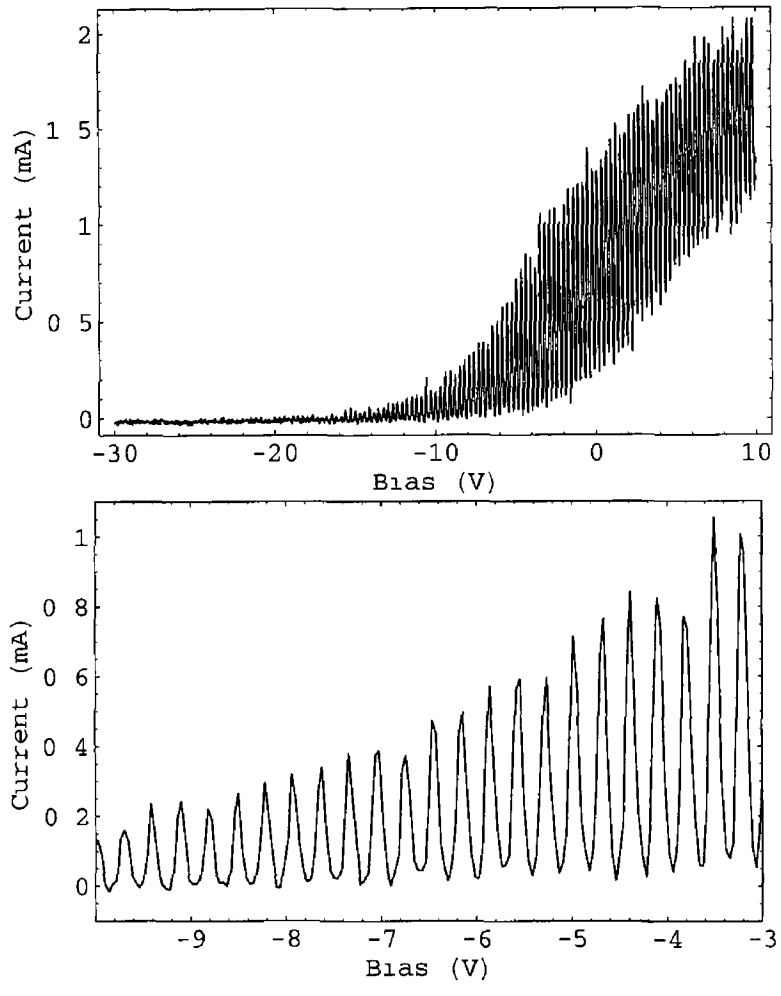

Figure 5 43 *Current-voltage characteristic with radio-frequency oscillations on the plasma potential Top full bias range Bottom -10 to -3 V*

on capacitive discharges, are expected to overestimate the electron temperature by larger differences However, still under those conditions the electron temperature can be properly estimated The basis for proper analysis in this case is found in references [53, 54], a revisited paper of these references has been submitted [85]

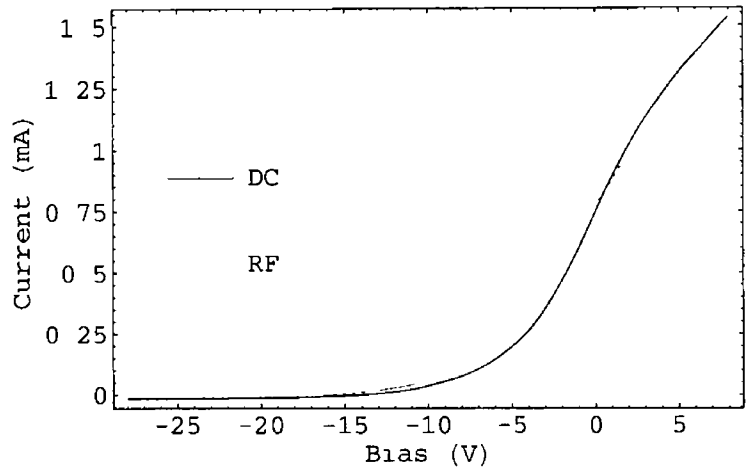

Figure 5 44 *Smoothed current-voltage characteristics for plasma potential with and without radio-frequency oscillations*

Three species plasma sheath solution and photo-detachment signals

As an example of a three speciesplasma we consider a third negative ion speciesin the plasma in considerable quantities We modify our particle in cell code to find sheath solutions with an extra (fictitious) negative ion speciesAr$^-$ (considered for modelling purposes only) Elastic and charge exchange collision cross sections for Ar$^+$ are used for Ar$^-$ No detachment or any other chemical reaction regarding the negative ions are considered

Probe must be positively biased with respect to the plasma potential in order to have a sheath with negative ions (electron saturation), the presence of negative ions is expected at the pre-sheath and sheath Electron inelastic collisions are disabled in the runs presented in this section The ratio of negative ion to electron density is fixed at the plasma boundary of the simulation, Ar$^-$ is set to be 10% of the total negative species

The main input parameters for the model are set as follows probe radius r_o = 0 2 mm, probe length 10 mm, plasma radius 5 mm, probe bias

$V_B = 20$ V, plasma potential $V_P = 0$ V, plasma density $n_o = 10^{15}$ m^{-3} and $n_o = 10^{16}$ m^{-3}, electron temperature $T_e = 1$ eV and Ar^+/Ar^- temperature $T_i \simeq 0\,026$ eV (300 K) Background pressure is set to 2 mTorr

Sheath solution

Figure 5 45 show the density profile as a function of radius for two different plasma densities We observe that the sheath is smaller at higher densities as expected Figure 5 46 show the negative ion density percentage of total negative species density as a function of radius for the two different plasma densities In either case the percentage of negative ions decrease with the radius At radius close to the probe surface the population of negative ions is smaller with respect to the electron than at larger radius

Photo-detachment signal

The photo-detachment diagnostic, reviewed by Bacal [63], consists on triggering a laser over the probe tip of a Langmuir probe while the probe is DC biased into electron saturation current The photons on the laser beam must have enough energy to detach electrons from negative ion species, this achieved with a Nd YAG laser Changes in the electron saturation current are measured and interpreted as $\Delta I_e/I_e = n_-/n_e$ The beam diameter is also important, the signal must be saturated (beam diameter 1 to 10 mm maximum) to make sure the negative ion density is not miss-interpreted

We simulate a photo-detachment signal with *Probe*-PIC model by turning suddenly all negative ions up to certain radius into electrons (laser beam radius), starting from one of our steady state solutions We use the sheath solution for density $n_o = 10^{15}$ m^{-3} to reproduce a photo-detachment signal We use the beam radius as 5 mm (10 mm diameter) Figure 5 47 show the cur-

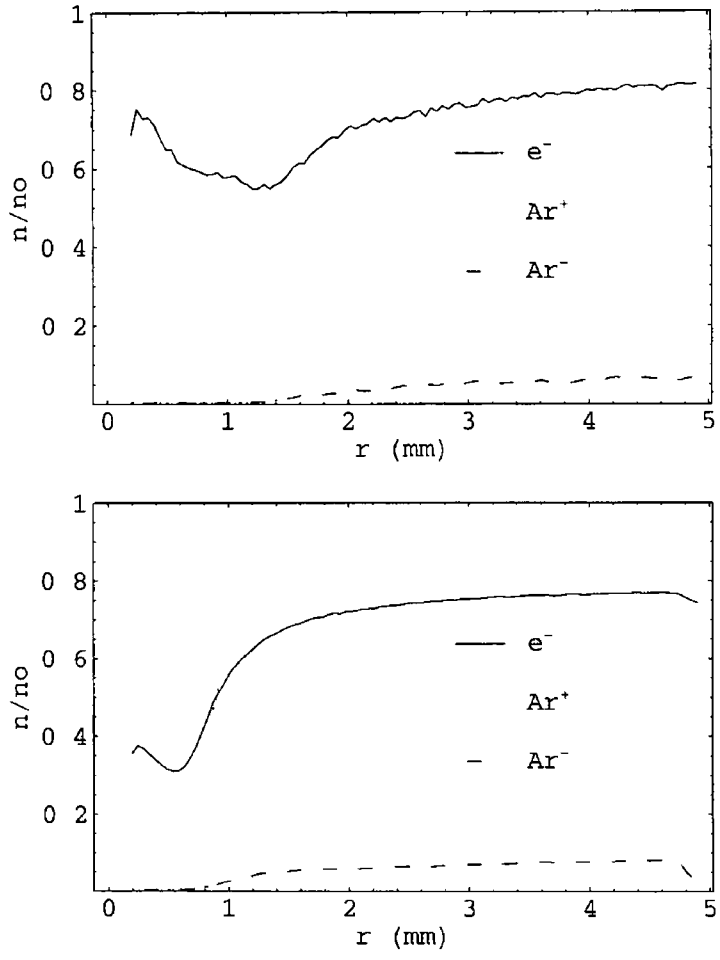

Figure 5 45 *Density profiles as a function of radius Top* $n_o = 10^{15}\ m^{-3}$ *Bottom* $n_o = 10^{16}\ m^{-3}$

rent saturation signal with and without photo-detachment signal, currents are vertically displaced to allow comparison From the photo-detachment signal the ratio of negative ions is calculated $\Delta I_e/I_e = 0\ 079$ Ar^- percentage of total negative species is 7 35 % for a laser beam of 10 mm diameter This actually underestimates the negative ion fraction as it was set up on the boundary condition (10 %) but is in good agreement with the average density ratios between 4 and 5 mm, 7 33 % (see top figure of 5 46)

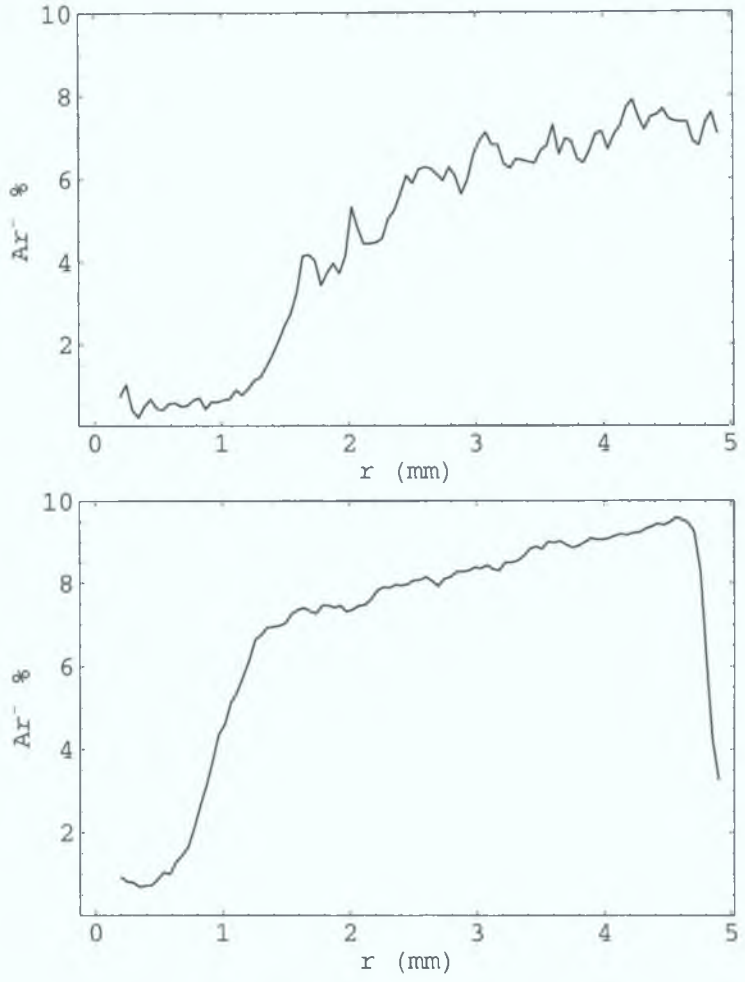

Figure 5.46: *Negative ion density percentage of the total negative species density as a function of radius. Top:* $n_o = 10^{15}\ m^{-3}$. *Bottom:* $n_o = 10^{16}\ m^{-3}$.

Discussion

Considering *Probe*-PIC sheath solution we can predict that a priori the negative ion density fraction to the electron density is not be the same in the sheath as in the pre-sheath and the plasma bulk. And thus we are in danger of under-estimating the negative ion density. The sheath solutions presented here are for densities within the range of those reported experimentally by Bacal [6]. At higher densities the sheath gets smaller and the risk of negative ion underestimation is reduced, but at low pressures the sheath becomes

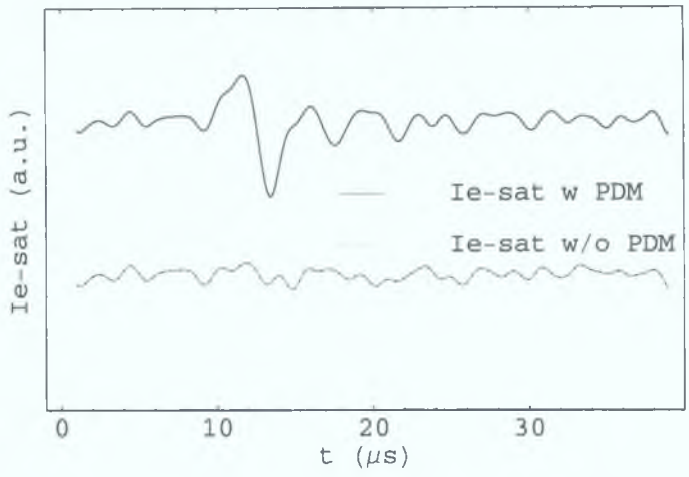

Figure 5.47: *Electron saturation current (arbitrary units) with and without photo-detachment signal for plasma density $n_o = 10^{15}\ m^{-3}$ (top figures in 5.45 and 5.46). Currents are vertically displaced for comparison reasons.*

considerably larger (of the order of a centimetre); where there are practical limitations to the laser beam diameter. Still in the case of negative ion sources of H^- the negative ion is lighter and this may contribute to reduce the sheath size and therefore the risk of underestimation of the negative ion density.

Long time runs in collision-less situation and stable solutions

An important difference between the model presented here an most other theories lies in the steadiness of the solution. We model the plasma dynamically, this is, the particles respond to changes in the space potential and collisions (in a collisional case). This leads to discrepancies in the results respect to collision-less theories, such as Laframboise [37]. In particular in collision-less case the dynamical character of the model allows for a large number of trapped orbits to exist after long time runs, most probably due to collective effects and the fact that the initial state of the system was not

the steady state. Basically the space potential changes fast enough for the ions, effectively trapping many of them in the sheath. The trapped orbits are reduced or removed in collisional plasmas due to particle-neutral collisions which enhance particle collection by the probe surface.

The generation of trapped orbits has been observed under different circumstances.

1. The probe is initially biased negatively respect to the plasma potential and a plasma is allowed to fill in the vicinity of the probe.

2. The probe is initially biased to the plasma potential until a steady state solution is achieved. Later the probe bias is instantaneously dropped several T_e to a given probe bias.

3. The probe is initially biased to the plasma potential until a steady state solution is achieved. Later the probe bias is dropped again several T_e in a fraction of a millisecond to a given bias.

In any case the space potential changes as the plasma develops. Temporal changes on the potential create effective potential traps for the ions. The space potential relaxes eventually with a very fast overall change in the first and second case leaving some ions trapped in the sheath. In the third case the trapping is an energy loss effect due to charges in the probe bias which are too fast for the ions to follow; ions orbiting the probe enter the sheath with certain amount of total energy but by the time the come back from their orbit to the sheath it has dropped in space potential. To prevent this the probe bias would have to be slowly change (tenths of a second maximum), which is not possible in this PIC code (extremely long computational time). The dynamical evolution of the system and these observations are made using

a XGrafix[2] version of the PIC model

Discussion

The one dimensional particle-in-cell code developed has been successful on qualitatively reproducing current-voltage characteristics for cylindrical Langmuir probes and known effects of un-compensation in case of RF oscillations in plasma potential Also in producing a photo-detachment signal and calling our attention on the fact that the ratio of negative ion density might not be the same in the pre-sheath and sheath as in the plasma bulk

Of particular interest is the failure of the Orbital Motion Limited theory (OML) to predict the ion saturation current and the density discrepancies within the model that result from the analysed I-V characteristics

The validity of the electron density measure at low pressures is supported by the model On the contrary, density measurements with the ion saturation current are shown to be erroneous However, it has been shown that the electron density can overestimate the plasma density around the upper limit of the pressure range of the collision-less probe theory Here we presented some probable evidence of the effects on the probe traces of a transition from the collision-less regime into the non-local or hydrodynamic (local) regimes Therefore, there could be an issue on the validity of the collision-less probe theory up to pressure $\sim$ 300 mTorr, even with careful selection of probe sheath radius

Further work is required with the PIC model at various densities and pressures There is also the possibility of creating a library of probe trace shapes or current density to plasma density ratios to be used to analyse

[2]XGrafix library by Vahid Vahedi, Payam Mirrashidi, Donald K Wong, John Verboncoeur, David Cooperberg, http //langmuir eecs Berkeley edu

experimental data Other possible works to study other effects, such as electron emission or secondary emission, multiple ion plasma probe traces, and to extend negative ion diagnostic signal study (photo-detachment) for a Hydrogen or other plasma with negative ion species The model could be also used for interpretation of new prototype probe data

CHAPTER 6

Summary

In this thesis the Applied Radio-frequency Ion Source (ARIS) experiment has been presented, two diagnostics have been implemented and used and finally three computer models, two of which have been developed for this thesis, have been used to complement the experimental work The ARIS device has been designed as a negative ion source prototype for basic plasma studies or a plasma source for plasma science studies We have set the foundation for future complementary measurements of the chemistry of volume production of negative ions, those should include metastable density measurements This device can also be used to benchmark plasma diagnostics under well defined plasma conditions We have successfully implemented and used Langmuir probes, single and double, and used the AC superimposing technique to accurately measure the electron energy distribution function (EEDF) Single particle and particle-in-cell models have been developed and a global model,

developed by R. Zorat, have been used to complement experimental observations in ARIS and plasmas in general.

On the experimental work Langmuir probes were used to scan axially the ARIS device through the source and the diffusion chamber for low pressure and moderate RF power. Results were taken with and without magnetic multi-cusp on the end plate of the diffusion chamber. Single probe measurements analysed with standard theory were taken with emphasis in the source and the source-diffusion transition region. The EEDFs were estimated by numerical differentiation of the traces. It was shown that the source and the diffusion chamber are decoupled and that changes on the end plate conditions (magnetic multi-cusp) do not affect the plasma parameters in the source. Only a small decrease in the plasma and floating potential where observed; this could be attributed to changes on the chambers internal walls although measurements under different conditions were taken within a few days difference. A single probe and a double probe were used to focus on the study the effects of the magnetised boundary (multi-cusp) on the end plate of the diffusion chamber. The EEDFs were obtained with the single probe using the AC superimposing technique. These were compared with electron temperature estimation from double probe traces. The discrepancies between the single and double probe estimations of the electron temperature are explained after understanding of the double probe limitations. The double probe effectively estimates T_e form the tail of the EEDF assuming a Maxwellian distribution; if the actual EEDF exhibits a depletion of high energy electrons (as compared to a Maxwellian distribution) then it is expected that a double probe would predict a lower electron temperature than the one estimated after a full integration of the EEDF. It is important to note that a proper criterion, up to our knowledge unreported before, for the

amplitude of the AC superimposed voltage has been presented in the case of a Maxwellian EEDF, it can be used as a rough guide. Regarding this technique it has also been noted that the second harmonic phase information is also useful, in contrast to the general usage of using only the amplitude of the second harmonic.

Also, on the experimental work the Cavity Ring Down Spectroscopy (CRDS) diagnostic was implemented in the diffusion chamber in ARIS; close to the diffusion chamber end plate. CRDS measurements of negative Hydrogen ion density (H^-) were taken in a Hydrogen plasma without any magnetic confinement, with the end plate magnetic multi-cusp and with the end plate multi-cusp plus extra magnetic confinement on the cylindrical walls of the diffusion chamber. Besides different magnetic confinements the measurements were also taken at different pressures in the range 5-10 mTorr. Results show an improvement in negative ion density at the lowest pressure and largest confinement conditions tested. This increase is associated with an increase in plasma density and a drop in electron temperature due to improved magnetic confinement. This qualitative behaviour is confirmed with a global model although there is no quantitative agreement between the model and the experimental results. Other important elements in the chemistry of the negative ion production are the vibrationally excited Hydrogen molecules. The model predicts a small increase with magnetic confinement in the density of vibrationally excited molecules for the low vibrational levels and a decrease in density for the high vibrational energy levels. Also a drop in pressure favours again the low energy level populations. In spite of the model results it is not clear yet what is the actual trend of the density of the vibrationally excited Hydrogen molecules since it is clear the model does not represents a good quantitative simulation of ARIS. Further exper-

imental measurements are required to elucidate the negative ion chemistry including possible wall production of H^- We note here that the negative ion measurements in ARIS represented a challenge due to the low density of the negative ion, the small cross section for the photo-detachment process and plasma affects on the reflectivity of the cavity mirrors The last problem was partially tackled by allowing a flow of neutral Hydrogen in front of the mirrors The low density and small cross section made the differences in the ring down time considerably smaller respect to the intrinsic noise to the diagnostic This noise was reduced using an integration technique on the CRDS data This allowed to reduce the noise by one order of magnitude The experimental error was reduced by another order of magnitude after averaging over thousands of ring down time samples This improvement in the analysis technique could prove useful to improve the accuracy on the measurements in devices where the negative ion densities are expected to be considerably larger It can also be an improvement to measurements on any other speciesin general, pushing the diagnostic sensitivity by an order of magnitude

On the computational work a model of single particle interaction with a magnetic multi-cusp has been presented Two different magnetic cusp configurations have been used showing similar results The particles modelled are electrons with a Maxwellian distribution It has been shown that most of the particle losses occur at the cusps even when pressure effects start to destroy the orbital motion of the electrons, dominant at low pressures This model lacks self-consistency and therefore the results are to be taken with care It shows a particle trapping effect a higher electron density in between cusps, specially at low pressure A local increase in electron density such as this would generate an electric field which would relax this effect A proper

multi-cusp model would required self consistency, where a PIC model is a possible option [86]

Also, on the computational work a particle-in-cell model with Monte Carlo collisions (PIC-MCC) has been developed to study the plasma transition from the plasma bulk into a cylindrical Langmuir probe This model is able to reproduce typical current-voltage characteristics A set of diagnostics allow us to watch carefully the plasma parameters in the model which can be lately compared with parameters resulting form the analysis of the current-voltage characteristics that result from the model This way basic probe theory has been compared to model results and pressure and RF effects on the probe characteristics have been studied Also basic studies of probe sheath solutions for plasmas with negative ion species have been done and presented, including the simulation of a photo-detachment signal on the electron current In general a few issues about basic assumptions of probe theory have been brought up, such as ion and electron current and plasma parameters estimated from them and their derivatives as a function of background pressure and RF distortion of the current-voltage characteristic

APPENDIX A

Match box

A.1 RF matching basics

In order to maximise the power delivery from a radio-frequency power supply it is required that the load impedance equals the supply output impedance Most commercial RF power supplies have an output impedance of 50 Ω But antennas used to excite inductive discharges do not have a real constant impedance equal to 50 Ω *(In general it is required that the load complex impedance equals the conjugate of the complex source impedance)* Even further the antenna impedance is a function of plasma parameters (plasma density and electron temperature) Therefore it is required a match box (also known as matching network) to turn the antennas complex impedance into a real 50 Ω

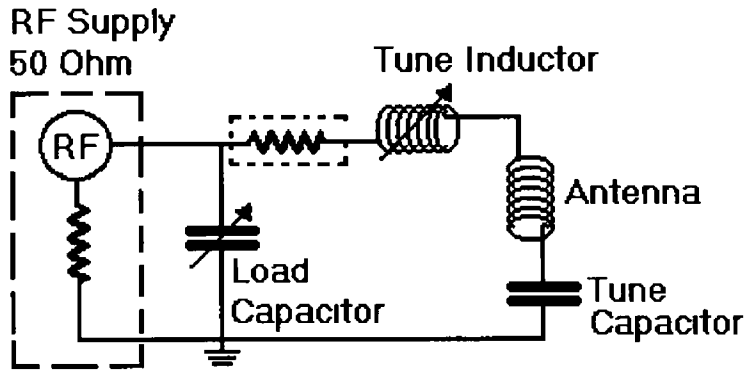

Figure A 1 *Diagram of the RF power circuit including the matchbox elements and the antenna The boxed resistance represents the matchbox and antenna resistance*

A.2 AMAT match box

The match box used in ARIS is a modified AMAT (Applied Materials) network match box It has a variable load (air) capacitor (200-2000 pF) and a variable tune inductor (0 1-0 4 μH) Figure A 1 shows a diagram of the matching network circuit including the antenna and the power supply

The match box requires two power supplies A 24 V supply, able to draw 100 mA, for the air cooling in the box and a $\pm$15 V supply, able to draw 0 5 A, for the electronics The match box has been set to auto-match

The load capacitor and tune inductor settings can be monitored with voltage signals ranging from -5 to +5 V where +5 V corresponds to the maximum limit on either the capacitor or the inductor, this is maximum load capacitance value and maximum tune inductance value

The pin configuration for auto match setting, match box settings read-out and voltage supply is given in table A 1

25 Pin socket at MB	Connect to
2	pin 3 (auto match)
3	pm 2 (auto match)
4	tune inductor (L) volatge (+/-5V)
7	load capacitor (C) volatge (+/-5V)
9	+24V
11	common (+/-15V)
13	-15V
14	common (+24V)
24	signal ground
25	+15V

Table A 1 *AMAT match box pin settings*

APPENDIX B

Non-unifrom to uniform distribution conversion

B.1 Introduction

Very often in particle simulations it is required to load or generate a population of particles with a particular –non-uniform– distribution such as a Maxwellian or Druyvesteyn distribution There are good algorithms to generate random numbers uniformly distributed [73] which can be used to generate any required distribution In this appendix we introduce the basic procedure to generate any particular non-uniformly distributed set of velocities/positions from a uniform random number generator

B.2 General transformation

Take a general non-uniform distribution function $h(x)$ where $x \in [a, b]$ Define a function

$$H(x) = \frac{\int_a^x h(x')\mathrm{d}x'}{\int_a^b h(x')\mathrm{d}x'} \tag{B 1}$$

Call the last function

$$H(x) = \chi \tag{B 2}$$

where $\chi \in [0, 1]$ If the inverse of the H function exists then

$$x = H^{-1}(\chi) \tag{B 3}$$

where $H^{-1}(\chi) \in [a, b]$ Then a sample of $\{\chi_i\}$ numbers generated with a uniform random number generator will generate a sample of $\{x_i\}$ numbers distributed as function h

It is most probably that for any give h function there is not an analytical inverse function H^{-1}, not even an analytical H function A numerical inverse function can be calculated by generating a table of pairs $\{\chi_i, x_i\}$ using equation (B 2) for $a < x < b$ The number of pairs must be large enough to outline smoothly the correlation Finally any $H^{-1}(\chi)$ can be calculated by interpolation

APPENDIX C

Magnetic mirrors

Magnetic fields are very effective on confining a single charged particle, though it does not mean that particles are irremediable confined There is a range of initial parameters which can lead particle loss in spite of the magnetic field for unperturbed particle orbits This depends on the degree of magnetisation of the particle For example if the particle moves along the field lines, the particle velocity is parallel to the magnetic field, then the particle is not affected by the magnetic field, no Lorentz force acting on the particle The chances that a particle may escape the field confinement are related to the ratio

$$\frac{v_{\perp}}{v_{\parallel}} = \tan\theta \tag{C 1}$$

Where $v_{\perp}$ and $v_{\parallel}$ are the velocity components perpendicular and parallel to the magnetic field at a given position respectively, and θ is the angle between the velocity and the magnetic field vector

Assume a particle has a velocity **v** at position **r** in a weak magnetic field region and moves towards a magnetic cusp, where the magnetic field lines converge and the filed intensity rises Figure C 1 shows a schematic diagram of this situation Lets assume that the particle is reflected at $\mathbf{r}_{\text{ref}}$ due to the

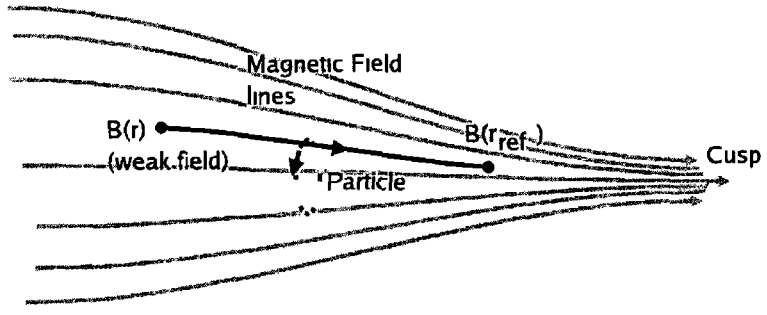

Figure C 1 *Diagram of a charged particle moving towards a magnetic cusp*

magnetic field And find the condition for the reflection If the particle only experiences a magnetic field force then the energy is conserved

$$E = \frac{1}{2}m(\underbrace{v_{\perp}^2 + v_{\parallel}^2}_{\text{at } \mathbf{r}}) = \frac{1}{2}m(\underbrace{v_{\perp \text{ref}}^2 + v_{\parallel \text{ref}}^2}_{\text{at } \mathbf{r}_{\text{ref}}}) \tag{C 2}$$

And if $\mathbf{r}_{\text{ref}}$ is the reflection point then the parallel velocity reverses at that positions so that $v_{\parallel \text{ref}} = 0$ The particle *magnetic moment* is also conserved, it is defined

$$\mu \equiv \frac{1}{2}\frac{mv_{\perp}^2}{|\mathbf{B}|} \tag{C 3}$$

The magnetic moment conservation

$$\frac{1}{2}\frac{mv_{\perp}^2}{|\mathbf{B}(\mathbf{r})|} = \frac{1}{2}\frac{mv_{\perp \text{ref}}^2}{|\mathbf{B}(\mathbf{r}_{\text{ref}})|} \tag{C 4}$$

Combining the energy conservation and magnetic moment conservation equations (C 2) and (C 4) and using $v_{\parallel \text{ref}} = 0$ we obtain

$$\frac{|\mathbf{B}(\mathbf{r})|}{|\mathbf{B}(\mathbf{r}_{\text{ref}})|} = \frac{v_{\perp}^2}{v_{\perp}^2 + v_{\parallel}^2} = \sin^2\theta \tag{C 5}$$

which is the condition for the particle reflection by the magnetic field at $\mathbf{r}_{ref}$ Using this we can define a critical angle

$$\theta_c = \sin^{-1}\left(\sqrt{\frac{|\mathbf{B}(\mathbf{r})|}{|\mathbf{B}(\mathbf{r}_{boundary})|}}\right) \tag{C 6}$$

for a particle in a magnetised region, between its velocity vector and the field vector, where $\mathbf{r}_{boundary}$ is the magnetised boundary position The particle will be reflected before the boundary if $\theta > \theta_c$ or would reach the boundary if $\theta \leq \theta_c$ The critical angle defines the loss cone, see figure C 2

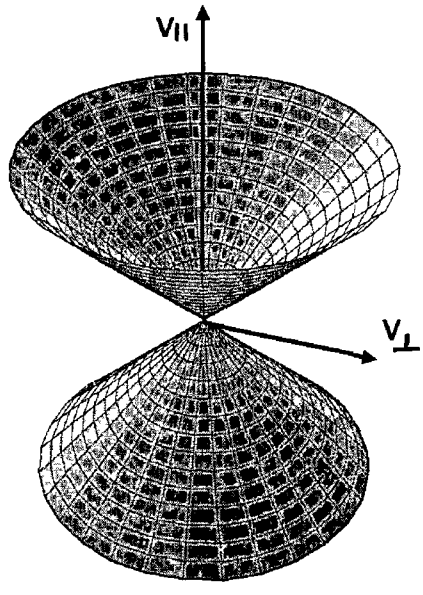

Figure C 2 *The loss cone Particles inside the cone are not reflected by the magnetic field*

APPENDIX D

Plasma basic formulas

The following are the basic formulas for an ICP plasma source valid for electropositive discharges (such as Argon)

1 ***Plasma frequency***

$$\omega_{Pe} = \sqrt{\frac{n_e e^2}{\epsilon_o m_e}} \tag{D 1}$$

2 ***Debye length***

$$\lambda_e = \sqrt{\frac{T_e \epsilon_o}{n_e e}} \tag{D 2}$$

3 ***Plasma potential*** (respect to the wall)

$$\phi = -T_e \ln\left(\sqrt{\frac{2\pi m_e}{M_i}}\right) \tag{D 3}$$

4 ***Sheath thickness*** (Child Law)

$$s = \frac{\sqrt{2}}{3}\lambda_e \left(\frac{2\phi}{T_e}\right)^{\frac{3}{4}} \tag{D 4}$$

5 ***Mean electron velocity and Bhom velocity***

$$\langle v_e \rangle = \sqrt{\frac{8eT_e}{\pi m_e}} \tag{D 5}$$

$$u_B = \sqrt{\frac{eT_e}{M_i}} \tag{D 6}$$

6 ***Ion mean free path and electron-neutral collision frequency***

$$\lambda_i = \frac{1}{n_g \sigma_i} \tag{D 7}$$

$$\nu_e = n_g \sigma_e \langle v_e \rangle \tag{D 8}$$

Where n_g is the neutral gas density, σ_i is the ion-neutral collision cross section and σ_e is the electron-neutral collision cross section

7 ***Particle flux to the walls***

$$\Gamma_e = \frac{1}{4} n_s \langle v_e \rangle e^{-\phi/Te} = \Gamma_i = n_s u_B \tag{D 9}$$

Where n_s is the plasma density at the sheath edge The longitudinal (h_l) and radial (h_R) edge to centre density ratio (Godyak)

$$h_l \equiv \frac{n_s}{n_o} \simeq \frac{0\,86}{\sqrt{3 + L_{\rm ch}/2\lambda_i}} \tag{D 10}$$

$$h_R \equiv \frac{n_s}{n_o} \simeq \frac{0\,8}{\sqrt{4 + R_{\rm ch}/\lambda_i}} \tag{D 11}$$

Where $R_{\rm ch}$ and $L_{\rm ch}$ are the chamber radius and length respectively

8 ***Plasma Dielectric Constant***

$$\epsilon_P \equiv \epsilon_o \kappa = \epsilon_o \left[1 - \frac{\omega_{Pe}^2}{\omega(\omega - i\nu_m)} \right] \tag{D 12}$$

9 ***Plasma κ***

$$\kappa = 1 - \frac{\omega_{Pe}^2}{\omega(\omega - i\nu)} \tag{D 13}$$

10 ***Plasma Conductivity***

$$\sigma_P = \frac{e^2 n_e}{m(\nu_m + i\omega)} \tag{D 14}$$

Notice the plasma dielectric constant and conductivity are related

$$i\omega\epsilon_P = \sigma_P + i\omega\epsilon_o \tag{D 15}$$

11 ***Skin depth***

$$\delta_P = \frac{c}{\omega} \frac{1}{Im(\kappa^{1/2})} \tag{D 16}$$

Bibliography

[1] R. Limpaecher and K. R. MacKenzie. Magnetic multipole containment of large uniform collisionless quiescent plasmas. *Rev. Sci. Instum.*, 44(6):726–731, June 1973.

[2] K. N. Leung, N. Hershkowitz, and K. R. MacKenzie. Plasma confinement by localized cusps. *Phys. Fluids*, 19(7):1045–1053, July 1976.

[3] W. L. Stirling, P. M. Ryan, C. C. Tsai, and K. N. Leung. Magnetic multipole line-cusp plasma generator for neutral beam injectors. *Rev. Sci. Instrum.*, 50(1):102, 1979.

[4] K. W. Ehlers. High current negative ion sources (invited). *Rev. Sci. Instrum.*, 61(1), January 1990.

[5] K.H. Berkner, R.V. Pyle, and J.W. Stearns. *Nuclear Fusion*, 15:249, 1975.

[6] M. Bacal and G. W. Hamilton. H^- and D^- Production in Plasmas. *Phys. Rev. Lett.*, 42(23):15381540, June 1979.

[7] W G Graham The kinetics of negative ions in discharges *Plasma Sources Sci Technol*, 4(2) 281–292, May 1995

[8] J M Wadehra and J N Bardsley Vibrational- and Rotational-State Dependence of Dissociative Attachment in e-H_2 Collisions *Phys Rev Lett*, 41(26) 17951798, December 1978

[9] J N Bardsley and J M Wadehra Dissociative attachment and vibrational excitation in low-energy collisions of electrons with H_2 and D_2 *Phys Rev A*, 20(4) 13981405, October 1979

[10] Th Mosbach, V Schulz von der Gathen, and H F Dobele Laser diagnostic of high vibrational and rotational H2-states *Contrib Plasma Phys*, 42(6-7) 650–656, November 2002

[11] R Zorat, J Goss, D Boilson, and D Vender Global model of a radiofrecuency H_2 plasma in DENISE *Plasma Sources Sci Technol*, 9(2), May 2000

[12] R Zorat and D Vender Global model of a rf hydrogen inductive plasma discharge in the deuterium negative ion source experiment including negative ions *J Phys D Appl Phys*, 33(14), July 2000

[13] R Zorat PhD Thesis, Numerical Modelling of Low Temperature Radio-Frequency Hydrogen Plasmas Dublin City University, Dublin, Ireland, 2003

[14] R L York, Jr Ralph R Stevens, K N Leung, and K W Ehlers Extraction of H^- beams from a magnetically filtered multicusp source *Rev Sci Instrum*, 55(5), May 1984

[15] A J T Holmes, G Dammertz, and T S Green H^- and electron production in a magnetic multipole source *Rev Sci Instrum* , 56(9), September 1985

[16] M P S Nightingale, A J T Holmes, and J D Jhonson Negative hydrogen ion extraction and electron control in a multipole ion source *Rev Sci Instrum* , 57(10), October 1986

[17] A J T Holmes, L M Lea, A F Newman, and M P S Hightindale Extraction of H^- and D^- ions from a large magnetic multipole source *Rev Sci Instrum* , 58(2), February 1987

[18] R McAdams, A J T Holmes, and M P S Nightingale H^- beam extraction experiments on the Culham small multipole source *Rev Sci Instrum* , 59(6), June 1988

[19] A J T Holmes Electron flow through tranverse magnetic fields in magnetic multipole arc discharges *Rev Sci Instrum* , 53(10) 1517, October 1982

[20] A J T Holmes Electron cooling in magnetic multipole arc discharges *Rev Sci Instrum* , 53(10) 1523, October 1982

[21] Azusa Fukano and Masatada Ogasawara Electron transport across magnetic filter in negative hydrogen ion source *Jpn J Appl Phys* , 40(12) 7072, 2001

[22] N P Curran, M B Hopkins, D Vender, and B W James The effect of addition of noble gases on H^- production in a dc filament discharge in hydrogen *Plasma Sources Sci Technol* , 9(2), May 2000

[23] M Bacal, M Nishimura, M Sasao, M Hamabe, M Wanda, and H Yamaoka Effect of argon additive m negative hydrogen ion sources *Rev Sci Instrum* , 73(2) 903–905, February 2002

[24] O Vollmer, H Falter, P Frank, B Heinemann, W Kraus, P Massmann, P McNeely, R Riedl, E Speth, R Trainham, and R Wilhelm Development of large radio frequency driven negative ion sources for fusion *Rev Sci Instrum* , 71(2) 939–942, February 2000

[25] H M Mott-Smith and Irvmg Langmuir The Theory of Collectors m Gaseous Discharges *Phys Rev* , 28(4) 727–763, October 1926

[26] Francis F Chen Electric probes In Richard H Huddlestone & Stanley L Leonard, editor, *Plasma Diagnostic Techniques*, chapter 4, pages 113–200 Academic, New York, 1965

[27] Noah Herhkowitz How langmuir probes work In W Lochte-Holtgreven, editor, *Plasma Diagnostics* New York, AIP Press, 1995

[28] V I Demidov, S V Ratynskaia, and K Rypdal Electric probes for plasmas The link between theory and instrument *Rev Sci Instum* , 73(10) 3409–3439, October 2002

[29] M J Druyvesteyn Der niedervoltbogen *Zeitschrift fur Physik*, 64 781–798, 1930

[30] Isaac D Sudit and R Claude Woods A workstation based langmuir probe system for low pressure dc plasmas *Rev Sci Instum* , 64(9), September 1993

[31] U Flender, B H Nguyen Thi, K Wiesemann, N A Khromov, and N B

Kolokolov RF harmonic suppression in Langmuir probe measurements in RF discharges *Plasma Sources Sci Technol*, 5 61–69, 1996

[32] V A Godyak, R B Piejak, and B M Alexandrovich Measurements of electron energy distribution function in low-pressure rf discharges *Plasma Sources Sci Technol*, 1 36–58, 1992

[33] G R Branner, E M Friar, and G Medicus Automatic plotting device for the second derivative of langmuir probe curves *Rev Sci Instrum*, 34(3) 231–237, March 1963

[34] J E Heidenreich III, J R Paraszczak, M Moisan, and G Sauve Electron energy distribution functions in oxigen microwave plasmas *J Vac Sci Technol B*, 6(1) 288–292, Jan/Feb 1988

[35] M A Lieberman and A J Lichtenberg *Principles of plasma discharges and materials processing* New York, Wiley, 1994

[36] I H Hutchinson *Principles of plasma diagnostics* Cambridge University Press, 2nd edition, 2002

[37] James G Laframboise Theory of spherical and cylindrical langmuir probes in a collisionless, maxwellian plasma at rest Technical Report 100, UTIAS (University of Toronto, Institute for Aerospace Studies), June 1966

[38] M B Hopkins and W G Graham Langmuir probe technique for plasma parameter measurement in a medium density discharge *Rev Sci Instum*, 57(9), September 1986

[39] Z Sternovsky and S Robertson Effect of charge exchange ions upon

Langmuir probe current *Appl Phys Lett*, 81(11) 1961–1963, September 2002

[40] Z Sternovsky, S Robertson, and M Lampe Ion collection by cylindrical probes in weakly collisional plasmas Theory and experiment *J Appl Phys*, 94

[41] B A Smith and L J Overzet Improvements to the floating double probe for time-resolved measurements *Rev Sci Instrum*, 69(3) 1372–1377, March 1998

[42] R R Arslanbekov, N A Khromov, and A A Kudryavtsev Probe measurements of electron energy distribution function at intermediate and high pressures and in a magnetic field *Plasma Sources Sci Technol*, 3 528–538, 1994

[43] V I Demidov, S V Ratynskaia, R J Armstrong, and K Rypdal Probe measurements of electron energy distribution funtions in a strongly magnetized low-pressure helium plasma *Physics of Plasmas*, 6(1) 350–358, January 1999

[44] V I Demidov, S V Ratynskaia, and K Rypdal Reducing influence of ion current on measurements of electron energy distributions in collisional plasmas *Rev Sci Instum*, 72(11) 4106–4109, November 2001

[45] S V Ratynskaia, V I Demidov, and K Rypdal Probe measurements of ion energy distribution in magnetized plasmas *Rev Sci Instum*, 73(12) 4232–4236, December 2002

[46] J V Scanlan and M B Hopkins Langmuir probe measurements of the electron energy distribution function in radio-frequency plasmas *J Vac Sci Technol A*, 10(4) 1207–1211, July 1992

[47] J I Hong, S H Seo, S S Kim, N S Yoon, C S Chang, and H Y Chang Electron temperature control with grid bias in inductively coupled argon plasma *Physics of Plasmas*, 6(3) 1017–1028, March 1999

[48] S J Jeon, G S Eom nad J H Kim, and W Choe Multichannel rf-compensated langmuir probe array driven by a single bias supply *Rev Sci Instum* , 73(2) 277–282, February 2002

[49] R H Bond PhD Thesis, Directed Electron Velocity Distributions in Rare Gas Discharges Using Guard Ring Probes California Institute of Technology, Pasadena, California, 1965

[50] J G Laframboise and L W Parker Probe design for orbit-limit current collection *The Physics of Fluids*, 16(5) 629–636, May 1973

[51] H W Rundle, D R Clark, and J M Deckers Electron energy distribution functions in a o_2 glow discharge *Can J Phys* , 51 144–148, 1973

[52] *Power Integrated Circuits Data Book*, volume 11 APEX Microtechnology

[53] A Boschi and F Magistrelli Effect of a RF Signal on the Characteristic of a Langmuir Probe *Il Nuovo Cimiento*, 29(2) 487–499, July 1963

[54] A Garscadden and K G Emeleus Notes on the Effect of Noise on Langmuir Probe Characteristics *Proc Phys Soc* , 79 535–541, 1962

[55] B M Annaratone, G F Counsell, H Kawano, and J E Allen On the use of double probes in RF discharges *Plasma Sources Sci Technol* , 1 232–241, 1992

[56] N St J Braithwaite, N M P Benjamin, and J E Allen An electrostatic probe technique for RF plasma *J Phys E Sci Instrum*, 20(8) 1046–1049, August 1987

[57] A P Paranjpe, J P McVittie, and S A Self A tuned Langmuir probe for measurements in rf glow discharges *J Appl Phys*, 67(11) 6718–6727, June 1990

[58] A E Wendt Passive external radio frequency filter for Langmuir probes *Rev Sci Instrum*, 72(7) 2926–2930, July 2001

[59] I D Sudit and F F Chen RF compensated probes for high-density discharges *Plasma Sources Sci Technol*, 3 162, 1994

[60] B M Annaratone and N St J Braithwaite A comparison of a passive (filtered) and an active (driven) probe for RF plasma diagnostics *Meas Sci Technol*, 2(8) 795–800, August 1991

[61] J V Scanlan PhD Thesis, Langmuir Probe Measurements in 13 56 MHz Discharges Dublin City University, Dublin, Ireland, 1991

[62] A O'Keefe and D A G Deacon Electron cooling in magnetic multipole arc discharges *Rev Sci Instrum*, 59(12) 2544, December 1988

[63] M Bacal Photodetachment diagostic techniques for measuring negative ion densities and temperatures in plasmas *Rev Sci Instrum*, 71(11), November 2000

[64] E Quandt, E Kraemer, and H F Dobele Measurements of negative-ion densites by cavity ring down spectroscopy *Europhys Lett*, 45(1) 32–37, January 1999

[65] F Grangeon, C Monard, J-L Dorier, A A Howling, Ch Hollenstein, D Romanini, and N Sadeghi Applications of the cavity ring-down technique to a large-area RF-reactor *Plasma Sources Sci Technol*, 8(3) 448–456, August 1999

[66] William H Press, Brian P Flannery, Saul A Teukolsky, and William T Vetterling *Numerical Recipies in Fortran The Art of Scientific Computing* Cambridge University Press

[67] H Tawara, Y Itikawa, H Nishimura, and M Yoshino Cross sections and related data for electron collisions with hydrogen molecules and molecular ions *J Phys Chem Ref Data*, 19(3) 617–636, 1990

[68] F Soberón and A R Ellingboe EEDF Measurements in the Diffusion-extraction Region of a Plasma in ARIS (Applied Radio-frequency Ion Source) *Contrib Plasma Phys*, 44(7-8) 629–634, October 2004

[69] Z Sternovsky, S Robertson, and M Lampe The contribution of charge exchange ion to cylindrical Langmuir probe current *Phys Plasmas*, 10

[70] C K Birdsall and A B Langdon *Plasma physics via computer simulation* Adam Hilger, 1991

[71] L D Landau and E M Lifshitz *Mechanics* Oxford, New York Pergamon Press, 3rd edition, 1976

[72] C Lanczos *The variational principles of mechanics* New York Dover Publications, 4th edition, 1986

[73] William H Press, Saul A Teukolsky, William T Vetterling, and Brian P Flannery *Numerical Recipies in C The Art of Scientific Computing* Cambridge University Press, 2nd edition

[74] Eric W Weisstein Box-Muller Transformation *MathWorld–A Wolfram Web Resource*

[75] M M Woolfson and G J Pert *Introduction to Computer Simulation* Oxford University Press, 1999

[76] J L Pack, R E Voshall, A V Phelps, and L E Kline Longitudinal electron diffusion coefficients in gases Noble gases *J Appl Phys*, 71(11) 5363–5371, June 1992

[77] A V Phelps Cross Sections and Swarm Coefficients for Nitrogen Ions and Neutrals in N_2 and Argon Ions and Neutrals in Ar for Energies from 0 1 eV to 10 keV *J Phys Chem Ref Data*, 20(3) 557–573, May 1991

[78] A V Phelps The application of scattering cross sections to ion flux models in discharge sheaths *J Appl Phys*, 76(2) 747–753, July 1994

[79] F Soberón, R Faulkner, and A R Ellingboe Plasma diffusion into a picket-fence magnetic field in ARIS (Applied Radio-frequency Ion Source) *Frontiers in Low Temperature Plasma Diagnostics*, V 172, April 2003

[80] V A Godyak, R B Piejak, and B M Alexandrovich Electron energy distribution function measurements and plasma parameters in inductively coupled argon plasma *Plasma Sources Sci Technol*, 11(4) 525–543, November 2002

[81] V A Godyak Plasma phenomena in inductive discharges *Plasma Phys Control Fusion*, 45(12A) A399–A424, November 2003

[82] C M Deegan, J P Goss, D Vender, and M B Hopkins Measurement of the electron energy distribution function in an argon radio-frequency

discharge in the γ mode *Appl Phys Lett*, 74(14) 1969–1971, April 1999

[83] I D Sudit and R C Woods A study of the accuracy of various Langmuir probe theories *J Appl Phys*, 76(8) 4488–4498, October 1994

[84] B A Smith and L J Overzet Observations of the ion-ion transition in an SF6 discharge using a fast floating double probe *Plasma Sources Sci Technol*, 8 82–90, 1999

[85] L Oksuz, F Soberón, and A R Ellingboe Analysis of uncompensated Langmuir probe characteristics in radio-frequency discharges revisited *Submitted to J Appl Phys*, 2005

[86] H Takekida and K Nanbu Particle modelling of plasma confinement by a multipolar magnetic field *J Phys D Appl Phys*, 37(13) 1800–1808, July 2004